Study of Z Boson Decays into Pairs of Muon and Tau Leptons with the CMS Detector at the LHC

Zur Erlangung des akademischen Grades eines
DOKTORS DER NATURWISSENSCHAFTEN
von der Fakultät für Physik des
Karlsruher Instituts für Technologie (KIT)
genehmigte

DISSERTATION

von

Dipl.-Phys. Manuel Zeise

Mündliche Prüfung: 15. Juli 2011

Referent: Prof. Dr. G. Quast
Institut für Experimentelle Kernphysik

Korreferent: Prof. Dr. W. de Boer
Institut für Experimentelle Kernphysik

Contents

1. Introduction

For centuries scientists have been studying the principles of nature in a systematic way. The common knowledge evolves through an interplay of improved theoretical models and advancing experiments. The rapid technical development beginning in the 19^{th} century pushed science forward and changed our view of the world.

Nowadays, physics knows four fundamental forces: the gravitational force between massive particles, the electromagnetic force between charged particle as well as the strong and the weak force on sub-atomic scales. The last three forces could be successfully combined to the widely accepted Standard Model of particle physics. Since then, many experiments could measure the parameters of the model and prove its validity. However, some observations raised new questions, e. g. the oscillations of neutrinos which is not described by the Standard Model.

Over the last two decades, a new particle accelerator, the Large Hadron Collider (LHC), has been constructed at the research centre CERN (European Organization for Nuclear Research) near Geneva, Switzerland. Two proton beams with a centre-of-mass energy of up to 14 TeV open a new area for high energy physics studies. The Compact Muon Solenoid (CMS) experiment is one of the two multi-purpose detectors at the LHC. The experiment will be able to improve the knowledge about the Standard Model and its parameters and it might also unveil evidence for physics beyond the Standard Model. However, the search for the elusive Higgs boson, the last undiscovered particle within the Standard Model, is its main task. This massive particle is a consequence of the Standard Model and explains the mass of particles. Its observation would be a further verification of the current Standard Model.

The mass of the Higgs boson cannot be predicted by theory. Former experiments at CERN and at Fermilab could only establish exclusion limits on the Higgs boson mass. Even at the high centre-of-mass energy of the LHC, the production cross section of the Higgs boson is small which complicates its observation. Higgs searches require a significant reduction of background contributions to exclude that a statistical fluctuation of the background mimics a potential signal. A precise knowledge of the background processes and an accurate estimation of the number of expected events are necessary for a reliable estimation of the significance of a measured signal.

In Chapter 2, the Standard Model of particle physics is introduced. The emphasis lies on the electroweak sector and the Higgs mechanism. The phenomenology of Z bosons and Higgs bosons at hadron colliders is explained and the results of recent experiments are presented.

The Large Hadron Collider and the CMS detector are described in Chapter 3 with a focus on technical details which are relevant for this thesis. A description of

the experimental infrastructure is given and the reconstruction of muons and taus is described in detail.

Chapter 4 concludes the introductory part with a description of the software used throughout this thesis, the software framework of the CMS experiment and the world-wide LHC computing grid.

The analysis part of the thesis starts in Chapter 5 with a study of Z bosons decaying into pairs of muons. The topology of the process, the possible background contributions and the selection of $Z \to \mu^+\mu^-$ events are introduced. The results from the data collected in 2010 are then compared to a simulation based study. The chapter concludes with a measurement of the Z boson production cross section including an estimation of the systematic uncertainties.

Chapter 6 is dedicated to the single muon High Level Trigger (HLT), i. e. an algorithm which selects events with at least one muon fulfilling specific requirements during the data-taking process. As part of the trigger commissioning and the monitoring of the trigger performance, the efficiency of the trigger selection is measured using two complementary and data-driven methods. The study of single muon triggers concludes with a detailed study of the isolation criteria that can be applied during the trigger decision.

The study of Z bosons decaying into tau leptons is the topic of Chapter 7. The selection and reconstruction of $Z \to \tau^+\tau^-$ candidates is introduced and followed by a motivation of its importance as background contribution for a study of a light Standard Model Higgs boson. Since the significance of a observation depends on the precise knowledge of the $Z \to \tau^+\tau^-$ background, a data-driven method which describes the shape of all relevant kinematic distributions as well as their absolute normalisation is introduced in this thesis. The prospect of this approach is presented and tested using samples of simulated events. The absolute normalisation is described and the arising systematic uncertainties are estimated. Using CMS data from 2010, the method is applied on reconstructed $Z \to \mu^+\mu^-$ events and a comparison with the direct $Z \to \tau^+\tau^-$ measurement is carried out.

The thesis concludes with a summary and an outlook in Chapter 8.

2. Standard Model of Particle Physics

Since the ancient world, philosophers and scientists searched for a description of matter and models for its structure. Ancient Greek philosophers established a model of indivisible constituents called *ta atomoa* [1], nevertheless this was more a philosophic than a scientific approach. Centuries later, scientists like Newton established physical models for kinematics and other phenomena in nature. In the 19^{th} century, first models for matter evolved and the constituents were categorized in elements. In 1904, Joseph Thomson published a first model for what we call today *atom* [2]. But this so-called plum pudding model could not explain the observed atomic light spectra. Ernest Rutherford introduced an improved model including the first substructure of atoms with a charged core and orbiting electrons after his famous gold-foil experiment with alpha particles [3]. With increasing energies of the probing particles new effects appeared, new ideas were developed and emerged as sophisticated models.

Today, all observed processes in nature can be traced back to four different fundamental forces, different in their strengths, ranges and types: gravitation as an interaction between massive objects, electromagnetic interaction between electrically charged objects, strong interaction as an adhesive force mediating between *coloured* quarks and gluons and weak interaction as another subatomic force and occurring in the description of the beta decay.

Table 2.1.: The gauge bosons in the Standard Model and various parameters: quantum numbers J^P, electric charge q and the third component of the weak isospin T_3 [4].

Particle	Interaction	Mass	J^P	q	T_3
Photon (γ)	electr.magn.	–	1^-	0	0
Z^0	weak	91.18 GeV/c^2	1	0	0
$W^{\pm}$	weak	80.40 GeV/c^2	1	$\pm e$	± 1
8 Gluons (g)	strong	–	1^-	0	0

The latter three forces could be combined during the last decades to a widely accepted model known as the *Standard Model of Particle Physics*. In this model forces are mediated by vector-bosons with spin $\hbar$. Table 2.1 summarizes some properties of these so-called gauge bosons. Beside these there are twelve fundamental particles ordered in two groups: quarks and leptons (see Table 2.2). These particles are called fermions. They carry spin $\hbar/2$, and each can be arranged into three families which also called *generations*. Each fermion has an associated anti-particle

with the same mass but opposite quantum numbers.

Table 2.2.: The fundamental fermions are grouped pairwise in three generations forming isospin doublets. The dashes for the quarks indicate that the mass eigenstates of quarks, which are listed here, are not identical with the eigenstates of the weak interaction.

Fermions	Generation 1	2	3	electr. charge	weak isospin	colour
Leptons	ν_e	ν_μ	ν_τ	0	$+1/2$	–
	e	μ	τ	$-e$	$-1/2$	
Quarks	u	c	t	$+2/3e$	$+1/2$	r, g, b
	d'	s'	b'	$-1/3e$	$-1/2$	

The grouping into three families is based on experimental observations; a muon coincides for example always with a certain neutrino in a particle interaction. Nicola Cabibbo proposed in 1963 [5] that weak currents can only transform particles within a doublet. However, the mass eigenstates of the quarks, which diagonalise the Yukawa-Coupling, are not identical to the eigenstates of the weak interaction, hence there are rare transitions of quarks from one doublet to another. The connection between both representations is the CKM-matrix[1] [6]:

$$\begin{pmatrix} |d'\rangle \\ |s'\rangle \\ |b'\rangle \end{pmatrix} = \begin{pmatrix} V_{\mathrm{ud}} & V_{\mathrm{us}} & V_{\mathrm{ub}} \\ V_{\mathrm{cd}} & V_{\mathrm{cs}} & V_{\mathrm{cb}} \\ V_{\mathrm{td}} & V_{\mathrm{ts}} & V_{\mathrm{tb}} \end{pmatrix} \begin{pmatrix} |d\rangle \\ |s\rangle \\ |b\rangle \end{pmatrix}$$

Composite particles made up of two and three quarks, called mesons and baryons, have been observed in experiments. The detection of the Δ^{++}, a bound state with spin $3\hbar/2$ made up of three up-quarks, demanded a new degree of freedom to preserve Pauli's exclusion principle for fermions. This degree of freedom is called *colour* and commonly the three possible values are *red*, *green* and *blue*. In line with mixing light, the sum of all three colours yields *white*. Quantum chromodynamics presumes that all observable particles are colourless. Moreover the colour of a quark does not affect its mass and rotations of the colour definitions do not change its interactions with other particles.

As mentioned above, colour is the charge of the strong interaction which is mediated by gluons. Demanding invariance in terms of rotations of the colour assignment in the three-dimensional colour space, there are finally eight gluons carrying a colour charge themselves as a result of the non-abelian nature just like spatial rotations. There is also one colour singlet, which is non-specific and therefore non-relevant for interactions.

Since gluons themselves are subject to the strong interaction and only colourless states can be observed, coloured objects behave differently than electric charges

[1] Cabibbo-Kobayashi-Maskawa matrix

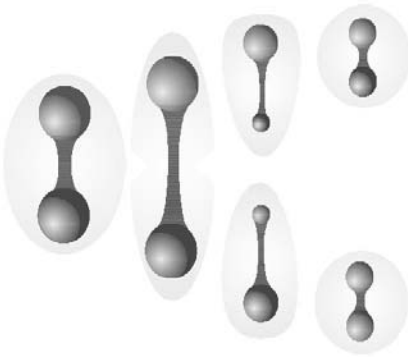

Figure 2.1.: Coloured objects cannot exist isolated. When separated from each other, the field forms gluon strings. At a distance of about 1 fm the string fragments and produces pairs of quarks and anti-quarks.

when being separated. Two quarks (or gluons) moving apart from each other form a field in-between whose energy increases linearly with the distance. Like a stretched rubber band breaking apart, the field fragments into smaller colourless parts and thus creates particles out of the vacuum as shown in Figure 2.1. This effect is called fragmentation.

2.1. Lagrange Formulation

The Lagrange formalism is a special formulation of classical mechanics [7]. The Lagrange function L

$$L = E_{\text{kin}}\left(\dot{q}_i, t\right) - E_{\text{pot}}\left(q_i, \dot{q}_i, t\right)$$

describes the dynamics of a physical system. The kinetic energy E_{kin} and the potential energy E_{pot} are functions of the generalised coordinates q_i and their derivatives $\dot{q}_i$.

For relativistic field theories it is useful to introduce the Lagrange density function $\mathcal{L}$ as

$$L = \int \mathcal{L}\left(\phi_i, \partial_\mu \phi_i\right) \, \mathrm{d}x \quad \text{with} \quad \partial_\mu \phi_i = \frac{\partial \phi_i}{\partial x^\mu}$$

and to consider $\mathcal{L}$ as a function of complex fields $\phi_i\left(x_\mu\right)$ and their covariant derivatives.

The equations of motion can be derived with the Euler-Lagrange equation, which follows from the calculus of variation:

$$\frac{\partial}{\partial x_\mu}\left(\frac{\partial \mathcal{L}}{\partial\left(\partial_\mu \phi_i\right)}\right) - \frac{\partial \mathcal{L}}{\partial \phi} = 0 \, .$$

Common Langrange Densities

The Lagrange density function for a free particle with spin $\frac{1}{2}$, e. g. electrons, reads

$$\mathcal{L} = i\bar{\psi}\gamma^{\mu}\partial_{\mu}\psi - m\bar{\psi}\psi$$

with the four-component Dirac spinor ψ, Dirac's γ-matrices and $\bar{\psi} = \psi^{+}\gamma^{0}$. The first term can be denoted as kinetic term, the second one as mass term.

A free scalar particle, i. e. with spin 0, is described by the Klein-Gordon equation or equivalent by

$$\mathcal{L} = \frac{1}{2}\left(\partial_{\mu}\phi\right)^{2} - \frac{1}{2}m^{2}\bar{\phi}\phi\,.$$

A vector field A for a massive spin 1 particle is defined by the Proca lagrangian density

$$\mathcal{L} = -\frac{1}{4}F^{\mu\nu}F_{\mu\nu} + \frac{1}{2}m^{2}A^{\mu}A_{\mu} \quad \text{with} \quad F^{\mu\nu} = \partial^{\mu}A^{\nu} - \partial^{\nu}A^{\mu}\,. \tag{2.1}$$

2.2. Local Gauge Invariance

In classical physics the inhomogeneous laws of electromagnetism exhibit an invariance under a special class of transformations. The experimentally accessible quantities, the electrical field $\vec{E}$ and the magnetic field $\vec{B}$, are connected with the electrostatic potential ϕ and the magnetic vector potential $\vec{A}$ through

$$\vec{B} = \vec{\nabla} \times \vec{A} \quad \text{and} \quad \vec{E} = -\vec{\nabla}\phi - \frac{\partial \vec{A}}{\partial t}\,.$$

A transformation

$$A_{\mu} \rightarrow A'_{\mu} = A_{\mu} - \partial_{\mu}\Lambda\left(\mathbf{x}\right) \quad \text{with} \quad A_{\mu} = \left(\phi, \vec{A}\right) \tag{2.2}$$

and an arbitrary, differentiable scalar field $\Lambda\left(\mathbf{x}\right)$, leaves the physically relevant fields $\vec{E}$ and $\vec{B}$ unchanged.

This gauge transformation can also be applied in the quantum field formulation. A local gauge transformation of the complex phase then reads

$$\psi\left(\mathbf{x}\right) \rightarrow \psi'\left(\mathbf{x}\right) = e^{i\alpha(\mathbf{x})}\psi\left(\mathbf{x}\right).$$

However, the derivative term in the Lagrangian for the considered fermion is not invariant under this transformation:

$$\begin{aligned}\partial_{\mu}\psi'\left(\mathbf{x}\right) &= \partial_{\mu}\left(e^{i\alpha(\mathbf{x})} \cdot \psi\left(\mathbf{x}\right)\right) \\ &= \underbrace{e^{i\alpha(\mathbf{x})} i\psi\left(\mathbf{x}\right)\partial_{\mu}\alpha\left(\mathbf{x}\right)}_{\neq 0} + e^{i\alpha(\mathbf{x})}\partial_{\mu}\psi\left(\mathbf{x}\right)\,.\end{aligned}$$

Invariance can be achieved by simultaneously introducing a vector field $A_\mu(\mathbf{x})$. The derivative ∂_μ is replaced with the so called covariant derivative D_μ

$$\partial_\mu \rightarrow D_\mu = \partial_\mu + ieA_\mu \tag{2.3}$$

and $A_\mu(\mathbf{x})$ has to transform as

$$A_\mu(\mathbf{x}) \rightarrow A'_\mu(\mathbf{x}) = A_\mu(\mathbf{x}) - \frac{1}{e}\partial_\mu \alpha(\mathbf{x}). \tag{2.4}$$

Finally, a local phase transformation does not affect the covariant derivative D_μ anymore. It is noteworthy that the required transformation (2.3) of the derivative operator is the quantum mechanic analogon of (2.2).

The Lagrange density then becomes

$$\mathcal{L} = i\bar{\psi}\gamma^\mu\partial_\mu\psi - m\bar{\psi}\psi - e\bar{\psi}\gamma^\mu\psi A_\mu$$

which is invariant under local phase transformations. The first two terms of the Lagrangian describe the free fermion and the third term expresses the coupling of the fermion to the electromagnetic vector field.

In summary, it is notable that the postulation of local invariance leads to a new vector function A_μ which is identical to to the classical magnetic vector potential. Furthermore, the introduced vector field A_μ has to be massless as a mass term

$$\frac{1}{2}m^2 A^\mu A_\mu$$

would spoil the invariance.

The Lagrangian density for quantum electrodynamics (QED) is complemented by an additional term for massless free spin-1 particle which represents free photons

$$\mathcal{L}_{\mathrm{QED}} = i\bar{\psi}\gamma^\mu\partial_\mu\psi - m\bar{\psi}\psi - j^\mu A_\mu - \frac{1}{4}F_{\mu\nu}F^{\mu\nu}$$

with $F^{\mu\nu}$ as defined in (2.1).

2.3. Weak Interaction

The weak interaction mediates transitions of quarks and leptons. Experiments suggest an arrangement in doublets of left-handed and singlets of right-handed leptons as shown in Table 2.3 [8]. The corresponding spin quantity T is referred to as weak isospin. A transition requires particles which carry a weak isospin of 1. For the following it is useful to further introduce the hypercharge Y defined as

$$Y = 2(Q - T_3)\,.$$

Table 2.3.: Experimental observation suggest an arrangement of the leptons in multiplets. As the current Standard Model assumes neutrinos to be massless in, they can only appear as left-handed particles. The left-handed quarks can be arranged in a similar way in three doublets according to their generation and six singlets for the right-handed quarks which are not shown in this table. The charged gauge bosons $\mathrm{W}^{\pm}$ carry a weak isospin of $T = \pm 1$, so the third component (T_3) of the weak isospin is conserved in transitions of quarks and leptons.

Generation			T	T_3
1	2	3		
$\begin{pmatrix}\nu_e\\ e^-\end{pmatrix}_{\mathrm{L}}$	$\begin{pmatrix}\nu_\mu\\ \mu^-\end{pmatrix}_{\mathrm{L}}$	$\begin{pmatrix}\nu_\tau\\ \tau^-\end{pmatrix}_{\mathrm{L}}$	$\frac{1}{2}$	$+\frac{1}{2}$
				$-\frac{1}{2}$
$(e^-)_{\mathrm{R}}$	$(\mu^-)_{\mathrm{R}}$	$(\tau^-)_{\mathrm{R}}$	0	0

For left- and right-handed particles, the invariance under local phase transformations can be written as

$$\psi_L \to \psi'_L = e^{i\alpha(x_\mu)\cdot\vec{T}+i\beta(x_\mu)Y}\psi_L$$
$$\psi_R \to \psi'_R = e^{i\beta(x_\mu)Y}\psi_R$$

with the three generators $\vec{T} = (T_1, T_2, T_3)$ of the SU(2) transformation and Y for the U(1) transformation.

The left-handed particles require the introduction of three vector fields $\vec{W}_\mu$ and one scalar field B which is necessary for the right-handed particles. The derivative then transforms as

$$\partial_\mu \to D_\mu = \partial_\mu - i\frac{g}{2}\vec{\sigma}\cdot\vec{W}_\mu - i\frac{g'}{2}YB^0_\mu$$

to achieve local gauge invariance. The resulting Lagrangian then reads

$$\mathcal{L} = i\bar{\psi}\gamma^\mu\partial_\mu\psi - \frac{1}{4}\vec{W}_{\mu\nu}\vec{W}^{\mu\nu} - \frac{1}{4}\vec{B}_{\mu\nu}\vec{B}^{\mu\nu}$$
$$- g\bar{\psi}\gamma^\mu\vec{T}\cdot\vec{W}_\mu\psi - \frac{g'}{2}\bar{\psi}\gamma^\mu B_\mu\psi_L\ .$$

The fields of the actual gauge bosons $\mathrm{W}^{\pm}$, Z^0 and A_μ are linear combinations of the four fields $\vec{W}_\mu$ and B^0:

$$W^{\pm} = \frac{1}{\sqrt{2}}\left(W^1 \mp iW^2\right)$$
$$Z^0 = -\sin(\theta_{\mathrm{W}})\,B^0 + \cos(\theta_{\mathrm{W}})\,W^3$$
$$A_\mu = \cos(\theta_{\mathrm{W}})\,B^0 + \sin(\theta_{\mathrm{W}})\,W^3\ .$$

The Weinberg angle θ_W includes the fact that photons couple to the electric charge of right- and left-handed fermions but not to the neutral neutrinos. The current world average [4] of the Weinberg angle is

$$\sin^2\theta_\mathrm{W} \approx 0.232$$

By introducing ladder operators $T^\pm = \frac{1}{2}(T_1 \pm T_2)$ it is possible to rewrite the Lagrangian in terms of A, Z^0 and $W^\pm$. Leaving the kinematic terms aside, each gauge particle gives rise to a characteristic interaction term:

$$\begin{aligned} A: &\quad \sim e\bar{\psi}\gamma^\mu\psi A_\mu \\ W^\pm: &\quad \sim g\bar{\psi}\gamma^\mu\left(1-\gamma^5\right)\left(T^+W_\mu^+ + T^-W_\mu^-\right)\psi \\ Z^0: &\quad \sim \frac{g}{\cos\theta_\mathrm{W}}\bar{\psi}\gamma^\mu\left(c_\mathrm{v} - c_\mathrm{a}\gamma^5\right)\psi Z_\mu \,. \end{aligned}$$

The photon couples to leptons in form of a pure vector current where the strength is proportional to the current. The coupling of the W and Z bosons exhibit both a vector and an axial-vector current. Since the term

$$\frac{1}{2}\left(1-\gamma^5\right)$$

can be identified as an operator which projects onto the left-handed part of a Dirac particle, hence the Lagrangian provides only couplings of W bosons to left-handed leptons. For interactions with Z bosons the contributions of both currents have different strengths. For a fermion with the charge q_f the couplings are given as

$$c_\mathrm{v} = T_3 + 2q_\mathrm{f}\sin^2\theta_\mathrm{W} \quad \text{and} \quad c_\mathrm{a} = T_3 \,.$$

In summary, the requirement of an invariance under local gauge transformations leads to a unification of the electromagnetic interaction and the weak interaction into a combined $\mathrm{SU(2)_L} \otimes \mathrm{U(1)_Y}$ group. However, the predicted massless bosons are in contradiction to the observed massive bosons since any additional mass term would spoil the gauge invariance.

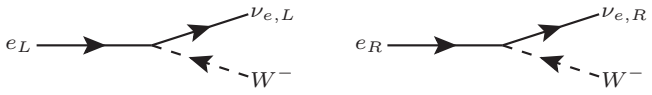

(a) observed (b) not observed

Figure 2.2.: Weak interaction mediates transitions of leptons. As weak currents only couple to left-handed fermions (and to right-handed anti-fermions) the transition depicted in the right-hand plot cannot be observed.

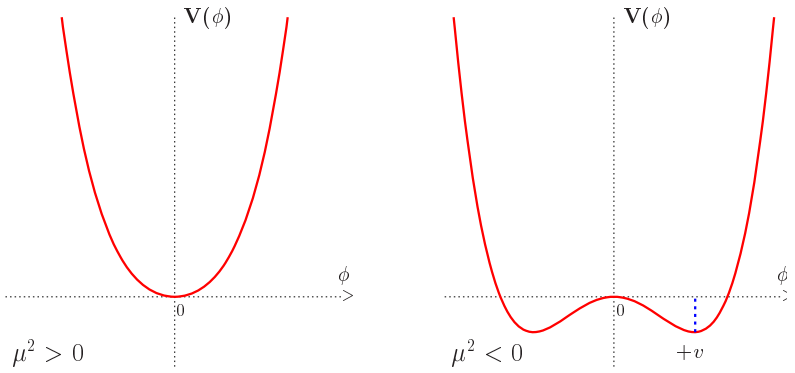

Figure 2.3.: Illustration of the spontaneous symmetry breaking: For $\mu^2 < 0$, the point $\phi = 0$ is an instable equilibrium, a real system will randomly choose $\phi = \pm v$ as ground state [12].

2.4. Spontaneous Symmetry Breaking

In order to explain existence of the gauge boson masses, the concept of spontaneous symmetry breaking has been proposed by Englert, Brout, Higgs, Guralnik, Hagen and Kibble [9, 10, 11]. The effect of spontaneously broken symmetry is known from ferromagnetism in solid state physics. The energy of a system of atoms with magnetic spins in absence of external magnetic fields depends only on the relative orientation of the spins to each other. A global rotation of all spins does not change the energy of the system. However, at a critical temperature T_c the ferromagnet undergoes a phase transition and below T_c all spins point in the same direction reducing the symmetry to rotations around this distinguished axis. The underlying symmetry is broken spontaneously.

2.4.1. Global Symmetry Breaking

Gauge bosons acquire mass by adding a complex scalar, the "Higgs field". For a complex scalar field with ϕ^4 self-interaction and real-value fields $\phi_{1,2}$ the Lagrangian reads

$$\mathcal{L} = \underbrace{\partial_\mu \phi^* \partial^\mu \phi}_{\text{“}E_{\text{kin}}\text{”}} - \underbrace{(\mu^2 \phi^* \phi + \lambda (\phi^* \phi)^2)}_{\text{“}E_{\text{pot}}\text{”}} \tag{2.5}$$

$$\text{with} \quad \phi = \frac{1}{\sqrt{2}} (\phi_1 + i\phi_2) \quad \text{and} \quad \lambda > 0.$$

This Lagrangian is invariant under global phase transformations. For $\mu^2 \geq 0$ the minimum of the potential V is at $\phi = 0$. For $\mu^2 < 0$ all points located on a circle given by

$$\phi_0 = e^{i\delta} \sqrt{\frac{-\mu^2}{\lambda}} \equiv v e^{i\delta} \tag{2.6}$$

represent the minimum of the potential as illustrated in the sectional drawing in Figure 2.3. It is convenient to rewrite the potential ϕ in terms of two real scalar fields, χ_1 and χ_2, to

$$\phi = \frac{1}{\sqrt{2}} \left(v + \chi_1 + i\chi_2 \right),$$

and expand the Lagrangian around the ground state:

$$\mathcal{L}' = \frac{1}{2} \left(\partial_\mu \chi_1 \right)^2 + \frac{1}{2} \left(\partial_\mu \chi_2 \right)^2 + \frac{1}{2} \left(2\mu^2 \right) \chi_1^2 + \text{const.} + \mathrm{O}\left(\chi^3 \right)$$

The result can be interpreted in the following way: The field χ_1 describes a massive particle with $m_{\chi_1} = \sqrt{-2\mu^2}$. The field χ_2 represents a massless particle and reflects the possibility of transitions from one ground state to another one through δ in Eq. (2.6). The chosen ground state in fact breaks the original radial symmetry.

Massless Goldstone bosons are a results of a spontaneously broken symmetry [13]. However there is no experimental evidence for the existence of such a particle. The emergence of such a boson can be avoided by couplings to the gauge fields in a spontaneously broken *local* symmetry as shown in the following subsection.

2.4.2. Local Gauge Symmetry Breaking

To achieve local gauge symmetry the Lagrangian in Eq. (2.5) has to be invariant under *local* transformations of the phase. A substitution for the derivative and a new gauge field A have to be introduced:

$$\begin{aligned} \partial_\mu &\rightarrow \partial_\mu + iqA_\mu \\ A_\mu &\rightarrow A_\mu - \frac{1}{e} \partial_\mu \theta \,. \end{aligned}$$

Again it is convenient to translate the Lagrangian into the ground state:

$$\begin{aligned} \mathcal{L} = & \frac{1}{2} \left(\partial_\mu \chi_1 \right)^2 + \frac{1}{2} \left(\partial_\mu \chi_2 \right)^2 + \mu^2 \chi_1^2 + \frac{1}{2} e^2 v^2 A_\mu A^\mu \\ & - evA_\mu \partial^\mu \chi_2 - \frac{1}{4} F_{\mu\nu} F^{\mu\nu} - \mu^2 \phi^* \phi - \lambda \left(\phi^* \phi \right)^2 \,. \end{aligned}$$

In this representation the Lagrangian exhibits a massive scalar particle χ_1, a massless scalar particle χ_2 and a massive vector boson A_μ. Furthermore, the Lagrangian includes an interaction term that couples the vector field to the Goldstone boson which is unphysical. Although the vector boson has acquired mass, the non-observability of the massless boson is a supposed flaw. This problem can be resolved by rewriting the complex field in the potential term as

$$\phi \rightarrow \frac{1}{\sqrt{2}} \left(v + h(x_\mu) \right) e^{i\zeta(x_\mu)/v} \,.$$

For the sake of convenience, χ_1 and χ_2 have been redefined to h and ζ. Accordingly, the Lagrangian then transforms to:

$$\begin{aligned}\mathcal{L}'' =& \frac{1}{2}\left(\partial_\mu h\right)^2 - \lambda v^2 h^2 + \frac{1}{2}e^2 v^2 A_\mu A^\mu - \lambda v h^3 - \frac{1}{4}\lambda h^4 \\ &+ \frac{1}{2}e^2 A_\mu A^\mu h^2 + v e^2 A_\mu A^\mu h - \frac{1}{4}F_{\mu\nu}F^{\mu\nu} \ .\end{aligned}$$

This representation includes a massive scalar Higgs boson h, a massive vector boson A and various couplings among particles from both classes. The degree of freedom in the original massless Goldstone boson has been absorbed in the massive vector field with its longitudinal polarisation as additional degree of freedom.

2.4.3. Symmetry Breaking for SU(2)⊗U(1)

In order to give the three gauge bosons a mass, the QED Lagrangian has to be extended by the introduction of a new covariant derivative

$$\partial_\mu \to D_\mu = \partial_\mu \underbrace{-g\frac{\vec{\sigma}}{2}\cdot\vec{W}_\mu - g'\frac{Y}{2}B_\mu}_{=(*)} \tag{2.7}$$

and a complex scalar doublet

$$\Phi = \begin{pmatrix}\phi^+ \\ \phi^0\end{pmatrix} = \frac{1}{\sqrt{2}}\begin{pmatrix}\phi_1 + i\phi_2 \\ \phi_3 + i\phi_4\end{pmatrix} \ .$$

The fourth scalar field is necessary due to theoretical constraints. The expectation value of $\Phi(x)$ in the ground state can be taken as

$$\Phi = \frac{1}{\sqrt{2}}\begin{pmatrix}0 \\ v\end{pmatrix} \quad \text{with} \quad v^2 = -\frac{\mu^2}{\lambda}, \quad \lambda > 0, \quad \mu^2 < 0$$

The term $|(*)\Phi|^2$ in the QED Lagrangian then becomes

$$|(*)\Phi|^2 = \left(\frac{1}{2}vg\right)^2 W_\mu^+ W^{-\mu} + \frac{1}{8}v^2 \begin{pmatrix}W_\mu^3 \\ B_\mu^0\end{pmatrix}^{\mathrm{T}} \begin{pmatrix}g^2 & -gg' \\ -gg' & g'^2\end{pmatrix} \begin{pmatrix}W^{3\mu} \\ B^{0\mu}\end{pmatrix}$$

with $W^\pm = \frac{1}{\sqrt{2}}\left(W^1 \mp iW^2\right)$ as introduced before. The second term can be diagonalised so that the gauge bosons A (for the photon) and Z appear:

$$|(*)\Phi|^2 = \frac{1}{2}M_{\mathrm{W}}^2 W_\mu^+ W^{-\mu} + \frac{1}{2}M_{\mathrm{Z}}^2 Z_\mu Z^\mu + \frac{1}{2}M_{\mathrm{A}}^2 A_\mu A^\mu$$

with

$$\begin{aligned}M_{\mathrm{A}} &= 0 \\ M_{\mathrm{W}} &= \frac{1}{2}vg \\ M_{\mathrm{Z}} &= \frac{1}{2}v\sqrt{g^2 + g'^2} \ .\end{aligned}$$

The aforementioned Weinberg angle is connected to g and g' through the relation

$$\tan\theta_{\mathrm{W}} = \frac{g'}{g}$$

and the relation between the Z and the W masses simplifies to

$$\frac{m_{\mathrm{W}}}{m_{\mathrm{Z}}} = \cos\theta_{\mathrm{W}}.$$

In conclusion, the demand for invariance under local SU(2)⊗U(1) transformations and the introduction of four scalar fields results in a unified theory for electroweak interactions. The weak gauge bosons gain their masses in this model while the photon remains massless.

However, one new massive scalar particle, the Higgs boson, appears as shown above. If collider experiments succeed in finding the Higgs boson and determining its mass, the current Standard Model would be completed. However, new phenomena such as neutrino oscillations indicate that further extensions to the Standard Model are unavoidable.

2.5. Parton Distribution Functions

The actual centre-of-mass energy in a collider experiment depends on the kind of particles which are used. For particles with a substructure only some of the constituents take part in the hard interaction contributing with their fraction of the total longitudinal momentum of the whole particle. The probability for an interaction of a constituent (called parton) is described by a parton density function which depends on the energy transfer Q of the collision. For low energies below about 1 GeV a proton for example acts as a point-like particle. With increasing energy the proton reveals that it consists of three so-called valence quarks which can be measured in deep inelastic scattering processes. For even larger energies the fraction of the momentum carried by the valence quarks decreases and gluons mediating the strong force and virtual quark-anti-quark pairs become visible in scattering processes (see also Figure 2.4)

2.6. Z Bosons at Hadron Colliders

The Z boson has been discovered at the Super Proton Synchrotron in 1983 [17] in collisions of protons and anti-protons. The study of the properties of Z bosons were one of the major goals of the Large Electron Positron experiment (LEP) from 1989 until 2000 [18]. The usage of point-like particles allowed a precision measurement and the LEP results for the mass and the width of theZ resonance are still the dominating contributions to the world average [4]:

$$m_{\mathrm{Z}} = 91.1876 \pm 0.0021 \text{ GeV}/c^2$$
$$\Gamma_{\mathrm{Z}} = 2.4952 \pm 0.0023 \text{ GeV}/c^2$$

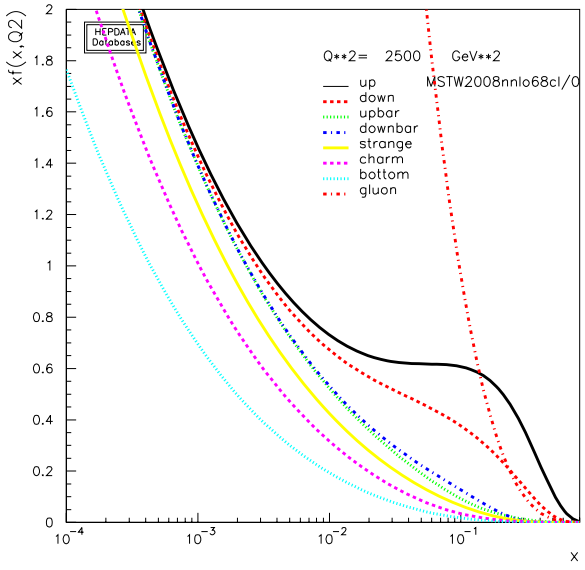

Figure 2.4.: Parton density function for quarks and gluons for $Q^2 = (50\,\mathrm{GeV}/c)^2 = 2500\,\mathrm{GeV}^2/c^2$ using MSTW2008nnlo [14, 15] as parton distribution function [16].

The individual results of the four main experiments at LEP are shown in Figure 2.5. More information about the measurements can be found in [19].

While the LEP experiments could measure the Z resonance in lineshape scans by varying the centre-of-mass energy, this approach is not possible for hadron colliders since the interacting partons carry only a fraction of the longitudinal proton momentum. In contrast to the Tevatron experiment, the higher beam energies lead to larger production cross sections as shown in Figure 2.6 and numerous Z bosons are available for various studies.

The main production process at the LHC is the annihilation of quarks and anti-quarks. With protons as colliding particles, the anti-quarks originate from sea quarks. With a subsequent decay into electrons or muons, the existing knowledge on the Z properties can be exploited to commission the CMS detector at the beginning of the data taking campaign. The re-discovery of known Standard Model particles forms the basis for later studies in yet unexplored fields of particle physics.

The production of Z bosons in association with a balancing hadronic jet is also very important for the deeper understanding of the detector. This event topology gives a good handle on the determination of the jet energy calibration. Details on this specific task can be found in [21] and [22].

2.7. Higgs Bosons at Hadron Colliders

The Higgs boson is the last particle in the Standard Model to be discovered. As the mass cannot be predicted by the theory, all calculations have to be done for different

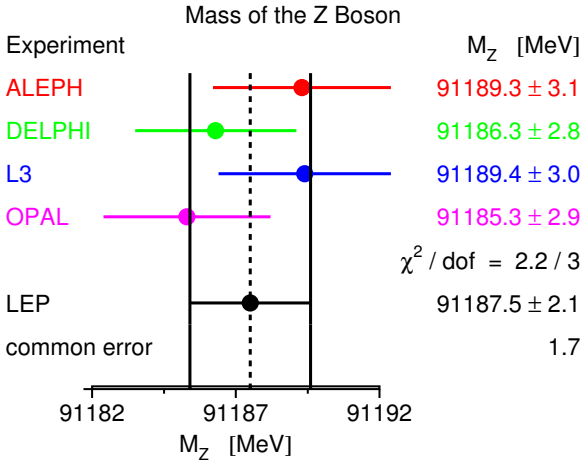

Figure 2.5.: Results for the measurement of the Z mass at LEP. The overall value is the result of a common fit to the individual results of the four experiments [20].

mass hypotheses, including the production and decay processes as explained in the following subsections. Previous experiments could only define exclusion limits for the mass of a potential Higgs boson.

Higgs Production Processes

Collisions of protons and anti-protons, as in the Tevatron experiments, allow a Higgs boson production by annihilation of valence quark-anti-quark pairs. However at the LHC with its proton-proton collisions, anti-quarks are only accessible as sea-quarks resulting in low cross sections for this production mode. The dominating production process over the relevant mass range is therefore the gluon-fusion. Since the Higgs bosons only couples to massive particles, the production is mediated by a quark loop, preferably a top quark loop as shown in Figure 2.7 and the left plot of Figure 2.8.

The fusion of two vector bosons of the electroweak interaction radiated by quarks is smaller by a factor of 10 compared to the gluon-fusion cross section. Nevertheless, the vector boson fusion is an important production mode since its event characteristic with two forward directed jets showing a high invariant mass and low hadronic activity in the central region of the detector allows a powerful reduction of background processes. The characteristic event topology and its benefits have been studied in [24].

Higgs bosons can also be radiated by an off-shell Drell-Yan resonance or by a top quark. Although both processes have a much lower cross section than the previously mentioned modes, they are also advantageous to use for a Higgs boson search since hadronic background events can be suppressed significantly through the requirement of a high momentum lepton coming from a decay of the associated particles when the Higgs decays into two photons.

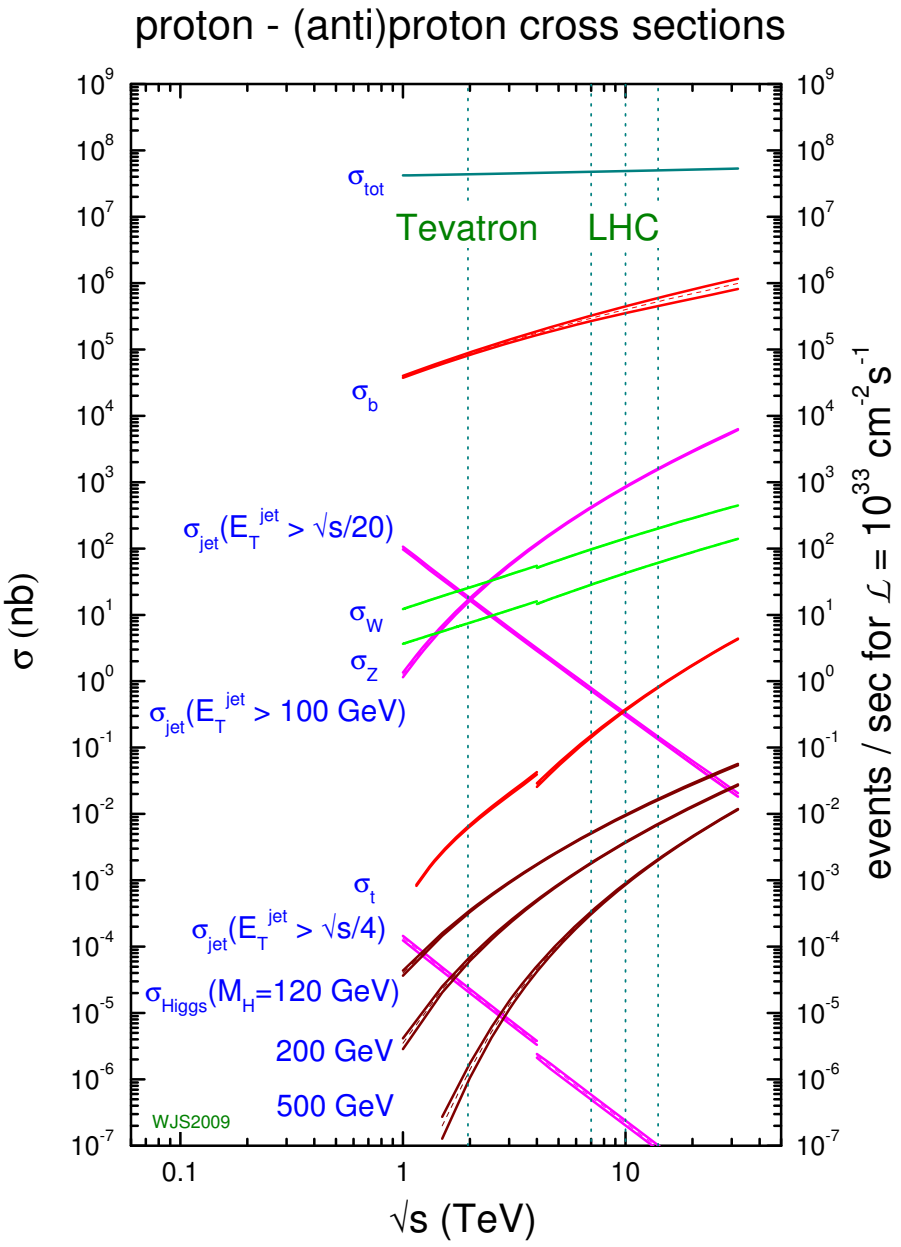

Figure 2.6.: Cross section for different production processes as a function of the centre-of-mass energy. The kink at $\sqrt{s} = 4$ TeV indicates the changeover from $p\bar{p}$ to pp collisions (taken from [14]).

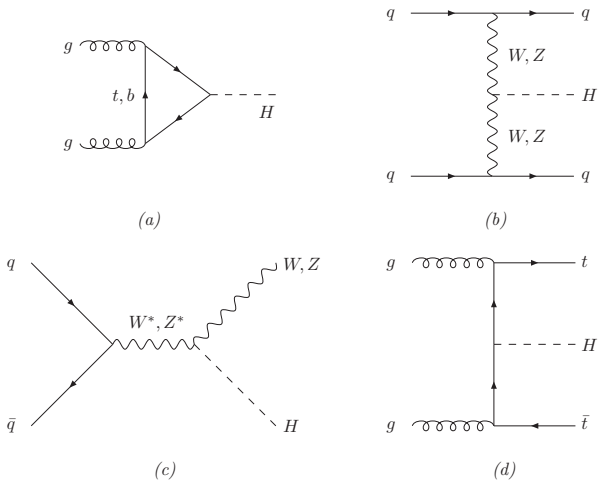

Figure 2.7.: Main production processes for a Standard Model Higgs boson in proton-proton collisions at the LHC [23].

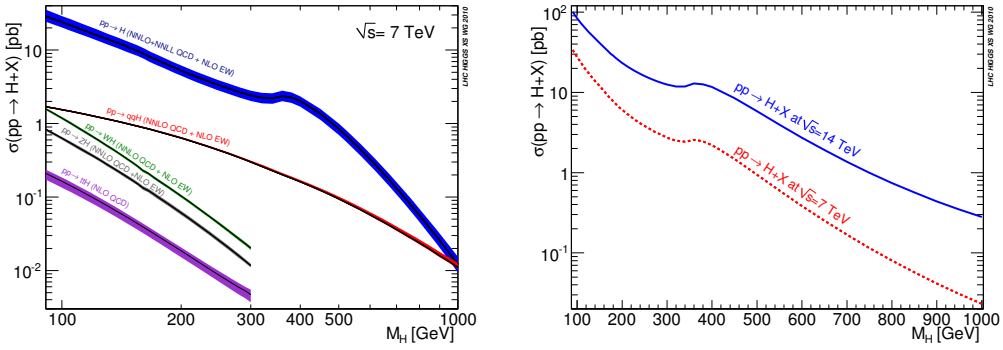

Figure 2.8.: Cross sections for different Higgs boson production modes in proton-proton collisions as a function of the Higgs boson mass (left) and comparison of the inclusive production cross sections at 7 TeV and 14 TeV [25].

Higgs Boson Decays

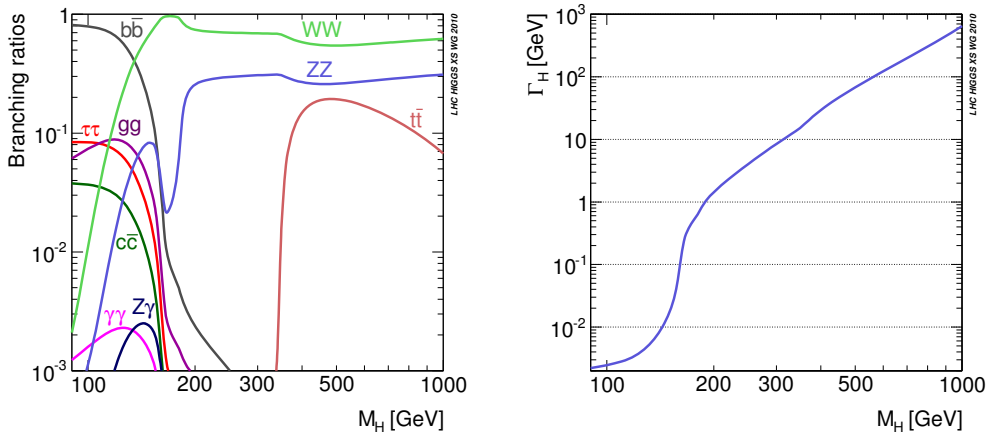

Figure 2.9.: Branching ratios for different decay modes (left) and the decay width Γ as a function of the Higgs boson mass. Both plots are taken from [25].

The Higgs boson couples to all massive particles and hence the decay modes depend on the Higgs boson mass. Figure 2.9 shows the branching ratios of the dominant decay modes together with the decay width of the Higgs boson over the relevant mass range covered by the LHC.

A light Higgs boson with a mass below the threshold of two vector bosons preferably decays into two bottom quarks. However, this decay channel is challenging as it suffers from large contributions from QCD processes and a discovery in this channel has been seen as unfeasible for a long time. Recent studies [26] exploiting sub-jet reconstruction techniques and multi-variate approaches suggest that studies can profit from boosted event topologies where a light Standard Model Higgs boson is produced in association with a back-to-back vector boson. This constraint topology allows a significant reduction of the QCD background and a Higgs search becomes feasible in $H \to b\bar{b}$.

The branching ratio of the decay into a pair of tau leptons is smaller by about an order of magnitude compared to the branching ratio for a decay into bottom quark pairs. A restriction to Higgs bosons produced in vector boson fusion leads to an event topology that allows a powerful reduction of events coming from background processes. It is used as one of the benchmark channels to gauge the success of the CMS experiment and is also part of the analysis in this thesis.

The decay into two gluons is possible via a quark loop in analogy to the gluon fusion production mechanism. The decay channel is competitive to the tau decay in this mass region but suffers from overwhelming contributions from QCD background processes to the final state.

The branching ratio of the Higgs decay into two photons is only some per mill and can only be exploited for a narrow mass range. However, this channel gives

only a clear signal peak if the energy of the two photons can be measured very accurately. This prospect drove the planning of the CMS experiment resulting in a detector design with a precise electro-magnetic calorimeter and a fine-granular silicon tracking detector.

Above a threshold of about 135 GeV/c^2 the decays in weak vector boson pairs become dominant. The branching ratio of the W W decay is twice the Z Z decay above 200 GeV/c^2 since the W bosons are distinguishable in their charges corresponding to two possible final states while having a similar mass. A leptonic decay of both Z bosons gives a very clean signature with a relatively small background contribution [27]. The mode where one Z boson decays leptonically and the other one hadronically is also a promising channel if the Higgs boson is produced in weak vector boson fusion [28]. The decay of the Higgs boson in W W suffers from the fact that no narrow mass peak can be reconstructed. For this reason, a precise understanding of the background contributions to this signal channel is thus very important [29, 30].

The decay into a top pair for a Higgs boson mass above 400 GeV/c^2 can hardly be used for a discovery due to the difficult measurement of the signal events and the increasing decay width (see right plot in Figure 2.9) leading to a broad signal peak on a huge background.

Finally, all promising channels will be used in combinations to prove the discovery of a certain Higgs boson mass or to define exclusion limits on the mass.

Results from Recent Analyses

The Large Electron Positron collider performed first searches for a Higgs boson mass near the Z mass. In later runs, the beam energy was successively increased up to $\sqrt{s} = 209$ GeV/c^2. As no analysis could establish a Higgs signal, the LEP community could only give an exclusion limit on the Higgs mass. The four collaborations excluded a Higgs boson below 114 GeV/c^2 with a confidence level of 95%.

The experiments CDF and DØ at the Tevatron [31] continued with analyses in $p\bar{p}$ collisions at $\sqrt{s} = 1.96$ TeV. With an integrated luminosity of up to 8.2 fb^{-1} the two experiments can exclude a Higgs boson mass between 158 GeV/c^2 and 173 GeV/c^2 at a 95% confidence level. The results for combined limits are shown in Figure 2.10 as a function of the potential Higgs boson mass.

High precision measurements of electroweak parameters allow an indirect determination of the Higgs boson mass. The electroweak working group at LEP combined the results of LEP, Tevatron and SLC [32] to give an upper limit of about 190 GeV/c^2 at 95 % confidence level. The preferred value for the Higgs boson mass based on the combination of various precision measurements is 89^{+35}_{-26} GeV/c^2 [20]. If the results from the direct searches are taken into account, the best value for the Higgs boson mass moves to 121^{+17}_{-6} GeV/c^2 [33]. The results of the combined efforts of LEP and Tevatron are shown in Figure 2.11 and Figure 2.12.

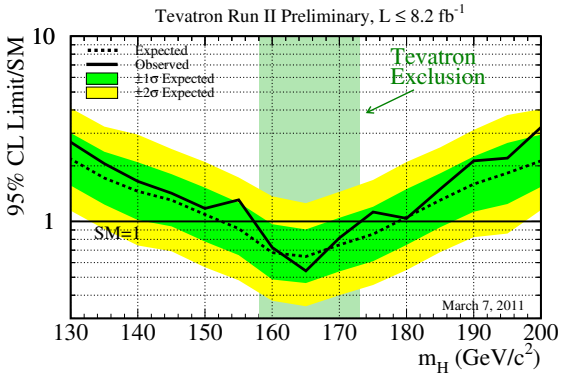

Figure 2.10.: Combined upper limits for a 95% confidence level on the standard model Higgs boson production from CDF and DØ analyses with an integrated luminosity of up to 8.2 fb^{-1} [34]: A Higgs boson mass between 158 GeV/c^2 and 173 GeV/c^2 can be excluded at a 95% confidence level. The results for the mass region below are not yet published.

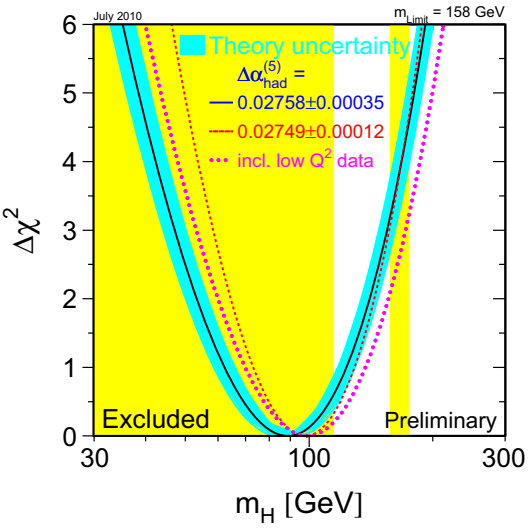

Figure 2.11.: Result for a combined fit of the Higgs boson mass in electroweak precision measurements at different experiments [20]. The preferred value for the Higgs boson mass is 89^{+35}_{-26} GeV/c^2 with a 68% confidence level. The dotted lines indicate the results for different assumptions for α_s. The region below 114 GeV/c^2 is excluded by direct searches at LEP, the mass region around 165 GeV/c^2 corresponds to the interval excluded by Tevatron which is also shown in Figure 2.10. In contrast to Figure 2.12 both direct exclusion ranges are not taken into account during the fit.

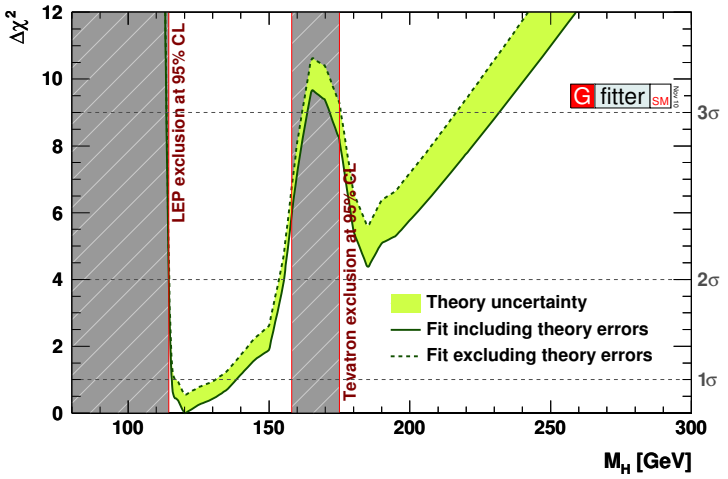

Figure 2.12.: Result for a combination of both electroweak precision measurements and direct searches at different experiments to constrain the Higgs boson mass [33]. The preferred value for the Higgs boson mass is 121^{+17}_{-6} GeV/c^2 with a 95% confidence level. It is important to note that the interval does not intersect the range below 114 GeV/c^2 by construction.

3. The Compact Muon Solenoid at the Large Hadron Collider

The Large Hadron Collider at CERN[1] near Geneva, Switzerland, at the Franco-Swiss border is the world's largest and most powerful hadron collider. With a centre-of-mass energy of 14 TeV and a design luminosity of $10^{34}\,\mathrm{cm}^{-2}\mathrm{s}^{-1}$, this proton-proton collider targets a new range for particle physics. A comprehensive description of the LHC and the participating experiments can be found in [35]. The original design of the LHC can be found in [36].

Four experiments are installed at the intersection points of the two proton beams: the ATLAS[2] [37, 38] experiment and the Compact Muon Solenoid (CMS) experiment are general-purpose detectors designed for a broad range of possible studies. The LHCb[3] [39] detector is specialised on physics with bottom quarks, especially the measurement of CP violation. TOTEM[4] [40] is placed near the CMS experiment and is intended to study diffractive physics and to measure the total cross section of the proton-proton interactions with high precision. The ALICE experiment [41] will study lead-lead collisions to explore quark-gluon plasmas.

3.1. Goals of the LHC

One of the main goals of the LHC is the discovery or the exclusion of the Standard Model Higgs Boson. The preceding large collider experiment at CERN, the Large Electron Positron collider (LEP), established a lower limit on the Higgs boson mass at $m_\mathrm{H} > 114\ \mathrm{GeV}/c^2$ with a 95% confidence level [42]. The projected beam parameters of the LHC, e. g. the luminosity, assure a high statistical precision to either prove the existence or set new exclusion limits on the Higgs boson over a wide mass range.

The extended energy range with respect to previous experiments allows a precise test of the Standard Model at energy scales of up to 1 TeV. Studies of QCD are possible over a wide range of transversal jet energies and allow new tests and tuning of models and parameters for the simulation of particle collisions. The production rate of top quarks allows a determination of the couplings within the Standard Model and a measurement of the top quark spin.

[1] Organisation Européenne pour la Recherche Nucléaire, formerly Conseil Européen pour la Recherche Nucléaire
[2] A Toroidal LHC ApparatuS
[3] Large Hadron Collider beauty
[4] Total Elastic and Diffractive Cross Section Measurement

The exploration of the nature of electro-weak symmetry breaking up to 1 TeV provides consistency checks of the current model and might unveil evidence for new physical theories, new massive vector bosons or the existence of extra dimensions. All these various studies could lead to a profound understanding of the Standard Model or even a grand unified theory of particle physics.

In Heavy Ion mode [35], the LHC uses lead ions (instead of proton beams) with a centre-of-mass energy of 2.76 TeV and a design luminosity of $10^{27}\,\mathrm{cm}^{-2}\mathrm{s}^{-1}$. These parameters extend the reachable range of current high energy physics experiments by more than one order of magnitude. A deeper understanding of the first few microseconds after the birth of the universe might be achieved by investigating quark-gluon plasma. In this state of aggregation, quarks and gluons behave like free particles comparable to ions and electrons in a plasma state.

The aforementioned studies impose a broad range of requirements on the CMS experiment as a multi-purpose detector. The search for Higgs bosons in various channels and other phenomena often require a good muon identification, a precise measurement of the momentum and the charge of the muon. A good measurement of the energy of photons and charged particles including a precise reconstruction of the production vertex are also necessary for these studies. A large spatial coverage of the hadron calorimeter again with high energy resolution allows a good determination of the missing transverse energy, which plays a dominant role in searches for super-symmetric particles. These particles are supposed to interact only weakly and often result in signatures with a large missing transverse energy.

3.2. The LHC Beam and the Luminosity Measurement

The Large Hadron Collider (LHC) is installed in the same tunnel that formerly hosted the Large Electron Positron collider (LEP). The tunnel is 27 km long and it is located 100 m beneath the surface at the border of Switzerland and France near Geneva. The LHC is mainly designed to accelerate protons which suffer less from synchrotron radiation than electrons due to their higher mass. As a consequence, much higher centre-of-mass energies can be reached. The acceleration of the particles is performed with 16 high frequency cavity resonators. The usage of electromagnetic waves for the acceleration implies that the protons cannot be a continuous stream of particles, instead they are packed into bunches.

1232 dipole magnets keep the particles on the circular path along the ring. Quadrupole and sextupole magnets focus and steer the beam along the way. A fine tuning of the beam optics is required to achieve optimal conditions for collisions at the intersection points where the experiments are located.

Although the nominal magnetic field strength of the dipoles is 8.33 T, which allows beam energies of up to 7 TeV per beam, the electrical current in the dipoles – and hereby the magnetic field strength – had to be decreased with respect to the design value for safety reasons. Smaller currents reduce the chances of a superconducting magnet quench, i. e. a sudden collapse of the superconducting state.

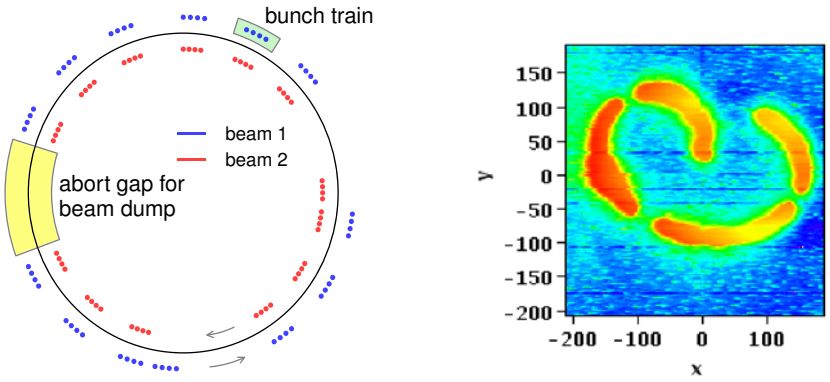

(a) Schematic view of a filling scheme in 2010 with 52 bunches per beam grouped as so-called bunch trains (raw data taken from [43]). The abort gap is necessary to ramp up the extraction magnets for a beam dump. The commissioning of the bunch trains is done in the pre-accelerator systems of the LHC.

(b) Monitoring of a beam dump in the x-y plane [44]: the linear chain of bunches is transformed into a helix by the fast-pulsed dilution magnets of the beam extraction system to distribute the heat load over the absorber graphite core. The colours indicate the intensity of the beam at a given position in arbitrary units (x and y are given in mm).

Figure 3.1.: Illustration of the filling scheme (left) and monitoring of the beam spot position before entering the absorber block during a beam extraction (right).

Several magnets were heavily damaged during an incident in 2008 after the loss of superconductivity and the subsequent evaporation of liquid helium which led to high pressure that could not be released sufficiently by the installed release valves. Only during the scheduled downtime in 2013 it will be possible to mount larger valves in all segments of the ring which allow to operate the LHC with a justifiable operational risk at the design energy. Until then, the LHC is operating at 3.5 TeV per beam.

A pre-acceleration of the protons is done in the existing Proton Synchrotron and Super Proton Synchrotron facilities (see also Table 3.1). The injection and extraction of the proton bunches from one accelerator to another is accomplished by so-called kicker magnets. These magnets are equipped with ferrite cores which feature small eddy currents. Combined with the small number of windings it is possible to ramp-up the magnetic field within 0.1µs. However, this injection mechanism causes the necessity of so-called *bunch trains* where several bunches are grouped in a pre-accelerator and are then transferred into the next accelerator as a group. One possible filling scheme for 52 bunches with bunch trains is depicted in Figure 3.1(a).

Table 3.1.: Overview of the LHC beam acceleration facilities for proton runs. The beam energy in the Large Hadron Collider can be set to any value between 450 GeV and 7 TeV.

Accelerator	Type	Beam Energy
Radio Frequency Quadrupole	linear	750 keV
Linear Accelerator 2	linear	50 MeV
Proton Synchroton Booster	ring	1.4 GeV
Proton Synchroton	ring	25 GeV
Super Proton Synchroton	ring	450 GeV
Large Hadron Collider	ring	7 TeV

3.2.1. Luminosity

The instantaneous luminosity is a characteristic quantity of a collider experiment and it solely depends on beam parameters. For a given physical process with the production cross section σ_{prod}, the number of generated events per second yields [35]

$$\dot{N}_{\text{evt}} = \frac{\partial N_{\text{evt}}}{\partial t} = L \cdot \sigma_{\text{prod}} \ . \tag{3.1}$$

Assuming a Gaussian distribution[35, 45] of the beam particles inside a bunch, the luminosity reads

$$L = \frac{N_a N_b f_{\text{rev}} \gamma_{\text{rel}}}{4\pi \epsilon_{\text{norm}} \beta^*} F$$

with the number of protons per beams N_a and N_b, the revolution frequency f_{rev} and the relativistic gamma factor γ_{rel}. The normalized beam emittance ϵ_{norm} and the beta function β^* at the collision point are a measure for the transverse movement of the beam particles. Both parameters are subject to fine tuning by the machine operators to maximise the luminosity. Since the collision of both beams incorporates a finite crossing angle θ_{c} it is necessary to also introduce the geometric luminosity reduction factor

$$F = \left(1 + \left(\frac{\theta_{\text{c}} \sigma_z}{2\sigma^*}\right)\right)^{-\frac{1}{2}} \tag{3.2}$$

with the transverse quadratic mean beam size σ^* and the longitudinal quadratic mean beam size σ_z, each measured at the interaction point. Equation (3.2) assumes symmetric beams and $\sigma_z \ll \beta^*$ for the sake of simplicity. A finite crossing angle is also required to avoid unwanted, parasitic interaction points near to the nominal one which would complicate the measurement for experiments.

The instantaneous luminosity is not constant over time as the intensity of the beam and its emittance deteriorate during a fill, i. e. the time between injection

Table 3.2.: Overview of the LHC machine parameters for proton-proton collisions at a centre-of-mass energy of 7 TeV in spring 2011. The values in the right column have not been achieved necessarily at the same time and not all of the values are yet publicly available (taken from [46, 47, 48, 49]).

Quantity	Unit	Value	
		Design	Achieved
Proton energy	TeV	7	3.5
Instantaneous luminosity	$\mathrm{cm}^{-2}\mathrm{s}^{-1}$	10^{34}	10^{33}
Protons per bunch	-	$1.15 \cdot 10^{11}$	$1.1 \cdot 10^{11}$
Number of bunches	-	2808	1092
Revolution frequency	kHz	11.2	11.2
Relativistic gamma factor	1	7460	3730
normalised transverse emittance	$\mathrm{mm} \cdot \mathrm{mrad}$	3.75	≈ 2
crossing angle at IP	µrad	285	100
bunch transverse width	µm	16.7	≈ 60
β^* at IP	m	0.55	1.5

and extraction of the proton beams. The information on the luminosity is thus being stored in the CMS experiment at the moment every 23 seconds, equivalent to roughly 2^{18} orbits of the protons in the accelerator. This time period is referred to as a luminosity section. The loss of intensity over time is depicted in Figure 3.2. The time period of data taking with a specific detector configuration is called a run which itself consists of many luminosity sections. In general, a few runs span a complete fill.

The integration of the instantaneous luminosity over time yields the *integrated* luminosity $\mathcal{L}$ which is generally quoted to express the amount of collision data that has been accumulated:

$$N_{\mathrm{evt}} = \int L \cdot \sigma_{\mathrm{prod}} \, \mathrm{d}t = \mathcal{L} \cdot \sigma_{\mathrm{prod}}$$

The desire to observe rare physical processes implies the necessity of a vast amount of collisions, i. e. a high integrated luminosity. High beam intensities are therefore essential.

3.2.2. Measurement of the Luminosity

The CMS experiment continuously measures the instantaneous luminosity with four rings of the forward hadronic calorimeter [45, 50]. The occupancy of the detector cells in these rings is linearly correlated with the luminosity and it thus allows a relative measurement. This online measurement is complemented by offline measurements, e. g. by counting reconstructed vertices in events with low activity or by coincidence measurements in both hemispheres of the forward hadronic calorimeter.

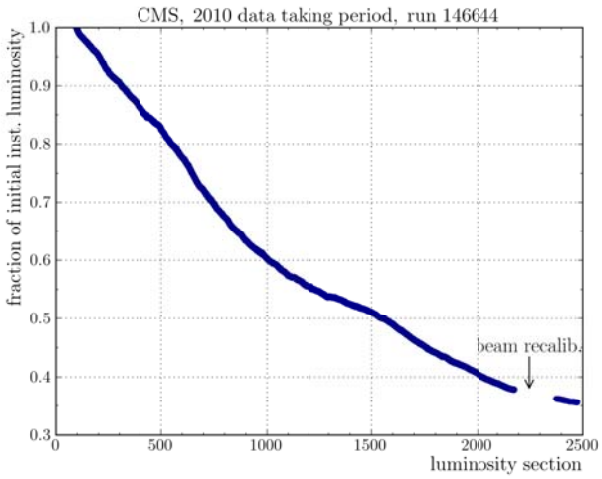

Figure 3.2.: Fraction of the initial instantaneous luminosity of the proton beams as a function of the luminosity section, i. e. as a function of time, in run 146644 on 26 September 2010. The gap on the right corresponds to a period with a re-adjustment of the proton beams that is excluded from analyses. The decrease over time suggests the usage of a dynamically prescaled trigger configuration to keep the rate of stored events constant over time.

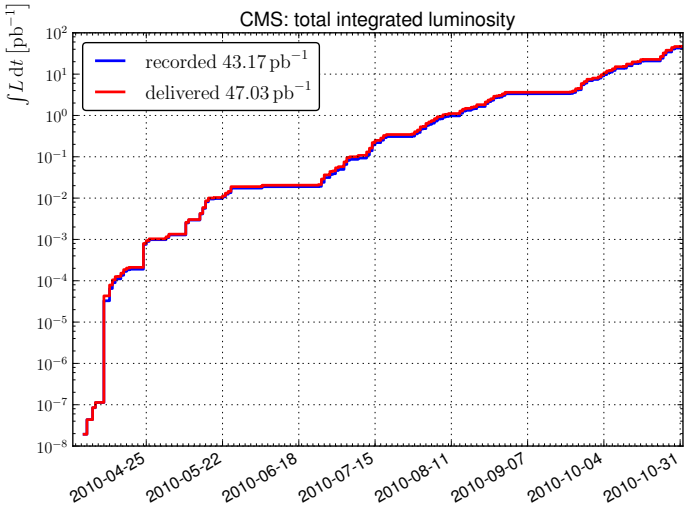

Figure 3.3.: Delivered and recorded integrated luminosity for proton-proton collisions at the CMS experiment in 2010. The two flat regions are attributed to technical stops of the LHC.

However, all previous mentioned approaches allow only a *relative* measurement of the luminosity. An absolute normalisation can be achieved either by a comparison to simulated events – leading to large systematic uncertainties – or by performing a so-called van der Meer scan [51]. The latter takes advantage of the connection between the interaction rate and the transverse beam separation to measure the actual size and shape of the beam. This is done in separate fills and yields a systematic uncertainty on the integrated luminosity of 4% [52]. The 2010 data sample that is used throughout this thesis corresponds to an integrated luminosity of $\mathcal{L} = 35.6 \pm 1.4\,\mathrm{pb}^{-1}$.

3.2.3. Pile-Up Events

A measurement with the CMS experiment suffers from the finite time resolution of the sub-detectors. If two collisions occur nearly at the same time, they cannot be separated in the detector. Energy deposits and observed interactions with the detector material sum up into one recorded event. Such overlapping events are called pile-up events. In general, one differentiates between in-time pile-up and out-ouf-time pile-up.

In-time pile-up events originate from interactions in the same bunch crossing as the main interaction process. Therefore, it increases with the number of protons per bunch and it is also correlated to the bunch volumina, e. g. a smaller β^* increases the interaction rate and thus the probability for additional interactions.

Out-of-time pile-up events arise from parasitic interaction points, from collisions of bunches with remnant molecules in the beam pipe and above all from interactions of adjacent bunch crossings. Hence, small time intervals between two bunches within a bunch train (i. e. a small bunch spacing) favour out-of-time pile-up.

For a few in-time pile-up events, the number of reconstructed vertices in an event is a good measure for the actual amount of pile-up as illustrated in Figure 3.4. Figure 3.5 depicts the average number of reconstructed vertices over time, divided into luminosity sections. While there was less than one pile-up event at the beginning (except for special beam configuration tests), the number of pile-up events has increased to roughly two additional interactions per event at the end of 2010. However, at the same time the instantaneous luminosity could be increased by three orders of magnitude. This was mainly achieved by injecting more proton bunches arranged in bunch trains with a comfortable bunch spacing of more than 50ns.

3.3. The Compact Muon Solenoid Experiment

The CMS detector is characterised by its compact design with the installation of the calorimeters inside a solenoid. The detector has a total weight of 12 500 t, an overall length of 21.5 m and an overall diameter of 16 m. The apparatus is small but heavy in comparison to the ATLAS detector with a weight of 7 000 t, a length of 46 m and 25 m in diameter. The layout is approximately symmetric to the interaction point of the two beams. The central barrel is flanked by endcaps on both sides. The

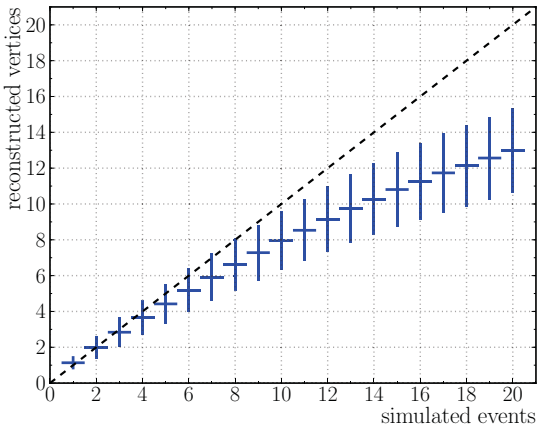

Figure 3.4.: Average number of reconstructed vertices as a function of the number of superimposed events. The n^{th} bin corresponds to $(n-1)$ added pile-up events. The error bars indicate the root mean square for each bin. The number of reconstructed vertices is a good measure for low pile-up scenarios. However, non-linear effects appear for larger pile-up effects.

tracking detector and the calorimeter are inside the magnet coil whereas the muon chambers are interleaved with the iron return yoke. A schematic view can be seen in Figure 3.6, a more profound introduction of the apparatus and its sub-detectors can be found in [54] and [23].

3.3.1. Coordinate Conventions

The nominal centre of the CMS detector corresponds to the origin of the CMS coordinate system. The z-axis is defined along the beam line anti-clockwise while x and y span the perpendicular plane in a right-handed coordinate system with the y axis pointing upwards to the surface. The azimuthal angle ϕ is measured within the transverse plane with respect to the positive x axis. The polar angle θ is defined with respect to the positive z direction.

Rapidity

In high energy physics it is useful to define a quantity called rapidity

$$y = \frac{1}{2} \ln \left(\frac{E + p_z}{E - p_z} \right).$$

It is an additive quantity for Lorentz transformations along the beam axis. In addition, the choice for this measure is favoured by the fact that the generated particle flux per rapidity interval is constant for hadron-hadron colliders.

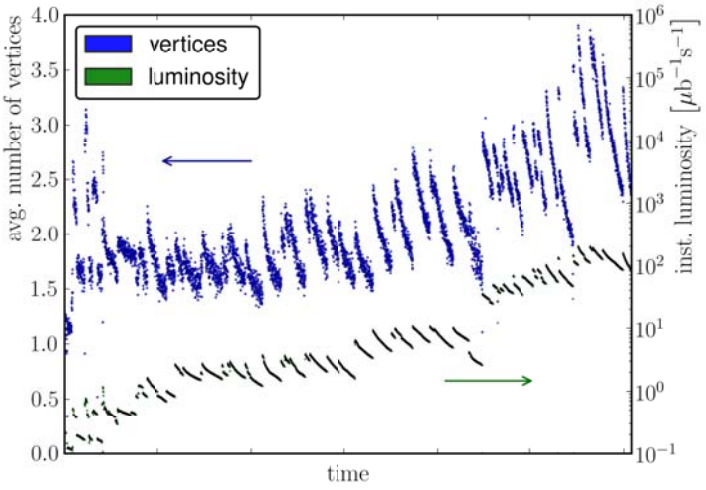

Figure 3.5.: Average number of reconstructed vertices, which is a measure for the influence of pile-up events, and the total instantaneous luminosity as a function of time in the 2010 data taking period. Each data point corresponds to one luminosity section. It is notable that the instantaneous luminosity has advanced by three orders of magnitude in 2010. This increase has been achieved mainly by using more proton bunches and not by an increase of the number of protons per bunch. As a consequence the effect of pile-up has only increased gently. The periodic decline of both plotted quantities is attributed to the intensity loss of the beams during a fill as depicted in Figure 3.2.

Pseudorapidity

It is also useful to define a second, similar quantity, the pseudorapidity

$$\eta = -\ln\left(\tan\left(\frac{\theta}{2}\right)\right).$$

Unlike the rapidity, it is defined just by the polar angle θ and does not require any knowledge about the mass of a particle. The pseudorapidity is zero for a vector perpendicular to the beam pipe and reaches infinity as the polar angle θ goes to zero. The sign of the pseudorapidity indicates the hemisphere. It is noteworthy that both rapidity and pseudorapidity coincide for massless particles or in the high energy limit, i. e. $E \approx |p|$.

3.3.2. Inner Tracking System

The innermost sub-detector is the tracking system (see Figure 3.8). The particle flux next to the interaction point is the highest in the experiment. Therefore, special attention is paid to the durability of the components under hard radiation and to the spatial resolution.

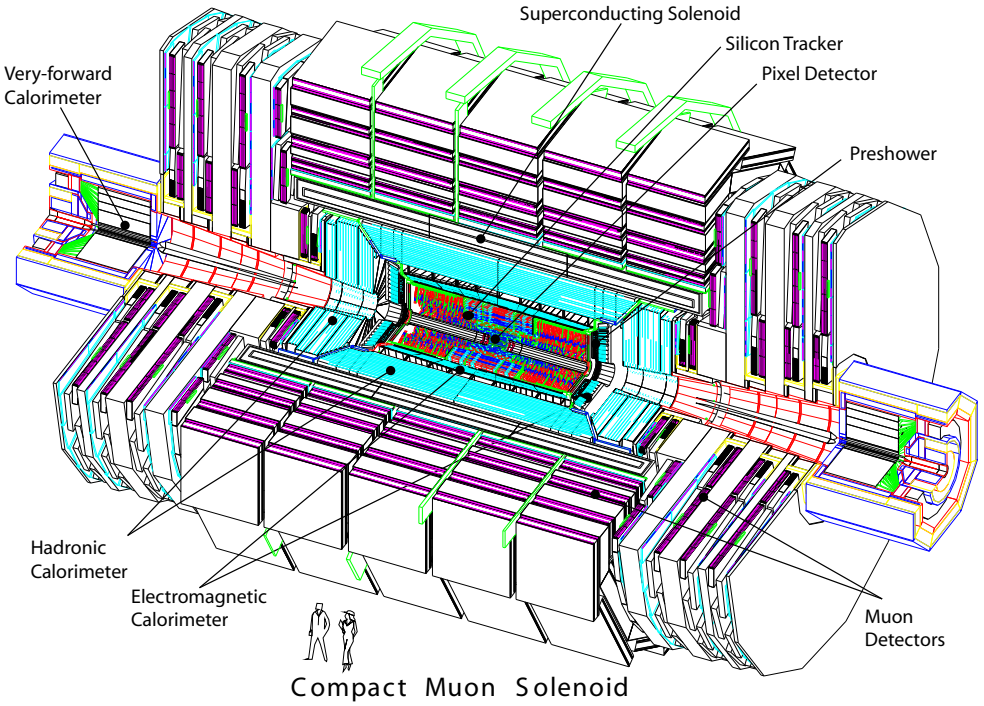

Figure 3.6.: Schematic view of the CMS detector and its components (taken from [53]).

To achieve a spatial resolution that allows to distinguish between different charged particles, the silicon pixel detectors have a size of $100 \times 150\,\mu\text{m}^2$ each and are used in three concentric layers. Together with special filter techniques, a spatial resolution of about $10\,\mu\text{m}$ in the r-ϕ-plane and $20\,\mu\text{m}$ in z-direction can be achieved [23].

In the region between 20 cm and 110 cm from the intersection point, silicon strip detectors are used in 10 layers. Due to their oblongness, these strips provide only two-dimensional information about a hit. The third dimension is covered by twisting different layers towards each other by $110\,\mu\text{rad}$. Their single-point resolution lies between $23 - 52\,\mu\text{m}$ in r-ϕ-direction and $230 - 530\,\mu\text{m}$ in z-direction depending on the distance to the beam pipe. These detectors are cheaper in comparison to the ones in the innermost region, but would give ambigous results in a high particle flux environment because of the lack of the third dimension.

The central tracking system can detect all kinds of charged particles. If a charged particle traverses the silicon, atoms are ionised and the read-out chip measures a current as the ionisation process is amplified by the applied high voltage. The magnetic field bends charged particle tracks and thus their interaction points in the detector are located on the arc of a spiral. The curvature of the arc is a direct measure for the momentum of the particle.

The tracking detectors allow an accurate measurement of the charged particles'

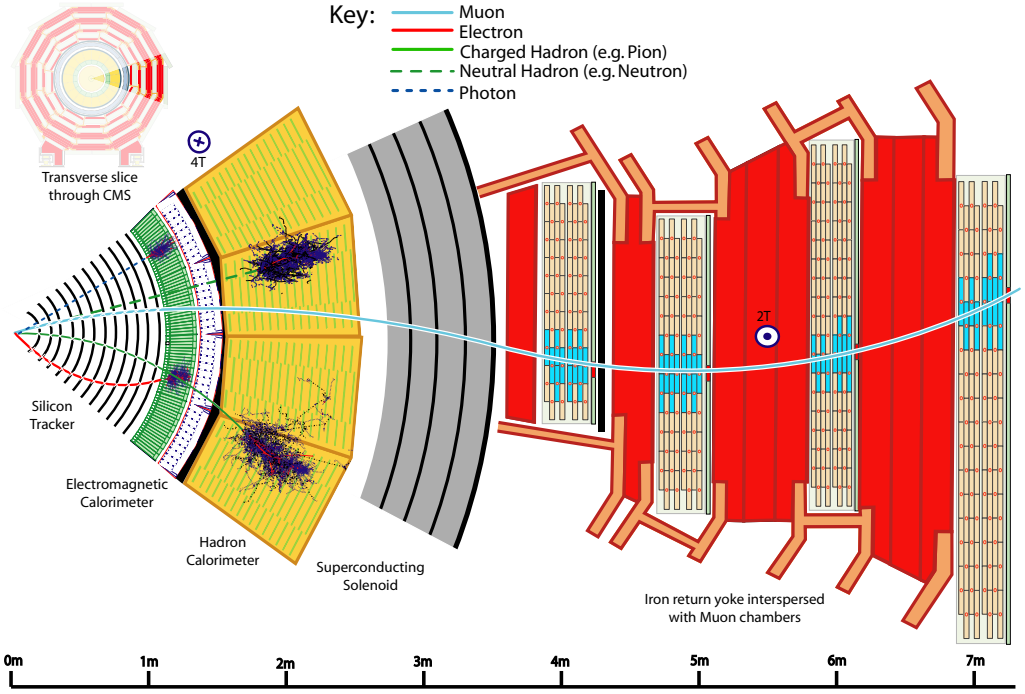

Figure 3.7.: Schematic view of a slice of the CMS detector with the interaction points and energy deposits of different particles (taken from [55]).

impact parameters and the position of secondary vertices. The latter ones are especially important for the identification of jets created by bottom quarks.

3.3.3. Electromagnetic Calorimeter

The electromagnetic calorimeter (see Figure 3.9) is a scintillation calorimeter made of lead tungstate. Incoming electromagnetic particles, e. g. electrons and photons, create a cascade of secondary particles inside the crystals by bremsstrahlung and electron-positron pair production. The number of created photons is a direct measure for the energy of the incident particle. Silicon avalanche photo diodes are used to detect the scintillation light in the barrel region because they are insensitive to high axial magnetic fields. In the endcap region, vacuum phototriodes are used since they withstand the high radiation exposure in this region. Additionally, the pre-shower detectors made of lead absorbers and silicon detectors are installed in front of the endcaps to separate high energetic single photons from photon pairs originating from π^0 decays.

The crystals cover 1° in ϕ and η direction and have a length of 23 cm which corresponds to 25.8 radiation lengths of lead tungstate. With a Molière radius of 2.2 cm and a light emittance of 80% within 25 ns, the electromagnetic calorimeter

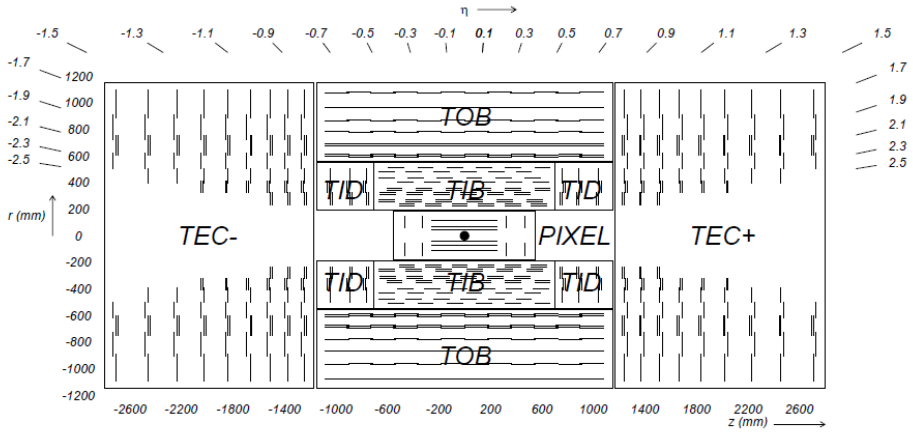

Figure 3.8.: Schematic view of the inner tracking system in the r-z plane (taken from [54]).

allows fast, complete and fine granular measurements. The calorimeter has a relative energy resolution of about 50% for electrons with $E_{\mathrm{T}} = 75$ GeV. This quantity roughly scales with $1/\sqrt{E}$ as the measuring is a counting process.

3.3.4. Hadronic Calorimeter

The hadron calorimeter (HCAL) is a sampling calorimeter made of brass absorber material and plastic scintillators (see Figure 3.10). Hadrons induce a cascade of secondary particles by subsequent inelastic scattering processes. Most of the energy is deposited in the absorber material, only a fraction is used for the detection in the scintillator material. This is the reason for the coarse energy resolution in comparison to the ECAL. The scintillation light is transported by wavelength-shifting fibres and clear fibres to hybrid photodiodes that can operate in high axial magnetic fields. The calorimeter is supplemented by additional detectors outside the magnet coil to increase the accuracy for high energetic jets. All in all hadronic jets can be measured over a distance of 11 hadronic interaction lengths.

A forward calorimeter extends the coverage of the HCAL from $|\eta| < 3$ to a pseudorapidity of 5.0 and allows a monitoring of the instantaneous luminosity (see Section 3.2.2). This region is characterised by high particle flux, the calorimeter thus consists of steel absorbers with embedded quartz fibres. Photomultiplier tubes detect the Cherenkov light emitted by cascade particles traversing the fibres.

The nearly hermetic coverage of the calorimeter allows for a good measurement of the missing transverse energy. However, the calorimetric response is different for electromagnetic and hadronic incoming particles of the same energy. Furthermore, the calorimeter is not uniform over the whole range of the pseudorapidity. Therefore it is necessary to apply a calibration for both the scale and the absolute offset for each sub-detector as a function of the pseudorapidity and transverse momentum. Details on the jet energy resolution and jet correction algorithms can be found in

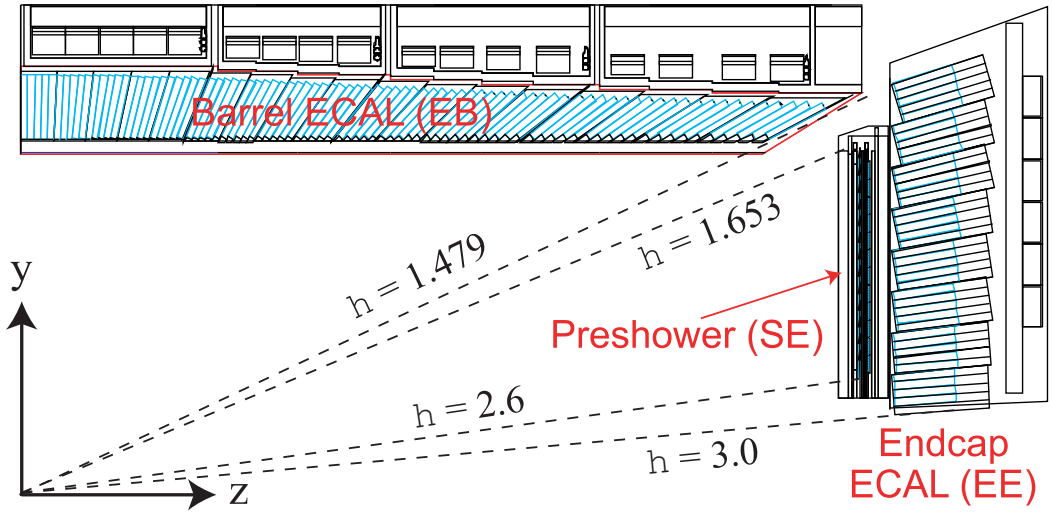

Figure 3.9.: Schematic view of the electromagnetic calorimeter in the r-z plane. The dashed lines indicate the pseudorapidity range not covered completely by the ECAL (taken from [56]).

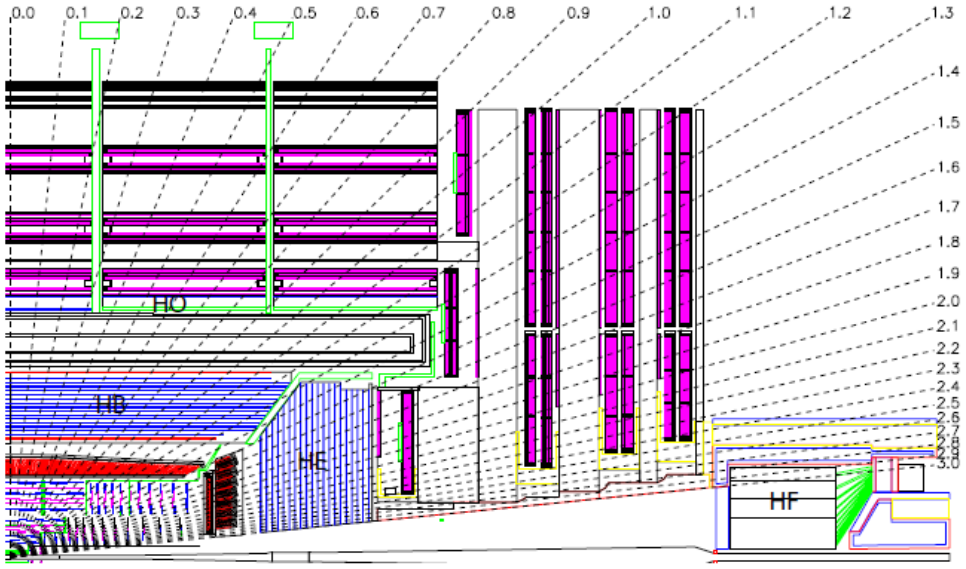

Figure 3.10.: Schematic view of the detector in the r-z plane. The sub-detectors of the hadron calorimeter are labelled in the inner and outer barrel region with HB and HO, in the endcap and forward region they are labelled with HE and HF. The dashed lines indicate the pseudorapidity (taken from [56]).

[57] and [58].

3.3.5. Muon Chambers

The muon detection system is interleaved with the iron return yoke (see Figure 3.11). As minimum ionizing particles, muons can traverse the iron while other particles, e. g. from high energetic jets, are shielded. Gaseous detectors are used for the muon chambers since they have to cover a large area. Aluminium drift tubes (DT) are installed in the barrel region. The endcaps accommodate cathode strip chambers (CSC) which also work reliably in spatially varying magnetic fields. Both detectors provide precise spatial information for an accurate reconstruction of the muon momentum.

Additionally, resistive plate chambers (RPC) are installed in both the barrel and the endcap region. RPCs can be operated at high rates and thus provide fast information which is used for the Level-1-trigger. The muon reconstruction also benefits from the different noise behaviour of the RPCs and the DTs/CSCs.

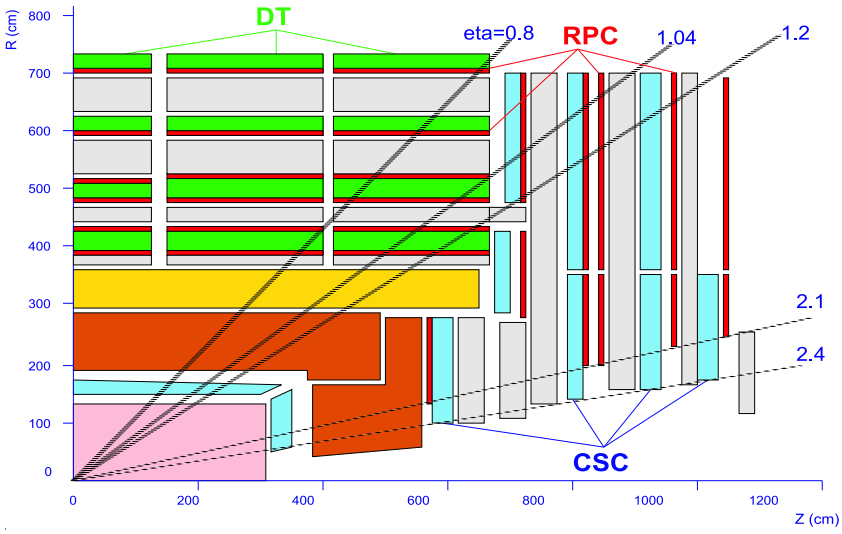

Figure 3.11.: Schematic view of the detector, highlighting the muon chambers with aluminium drift tubes (DT), resistive plate chambers (RPC) and cathode strip chambers (CSC). The components of the iron return yoke are shown in gray, the solenoid is presented in yellow (taken from [53]).

The muon chambers feature detection efficiencies better than 98%. The momentum resolution is only some percent in the barrel region [53]). The trajectories of the muons can be accurately determined using a combination of the muon chambers and the inner tracking system. The reconstruction of muons is outlined in Section 3.4.1.

3.3.6. Trigger and Data Acquisition System

Around a billion collisions take place in the detector every second at design luminosity. Due to limitations of current computing technology, only a small fraction of about 400 events per second can be stored to disks and tapes continuously. Therefore, a cascade of triggers (see Figure 3.12) has to reduce the amount of data to a level that can be handled by available computing resources. Fortunately, the manageable output rate has been increased over the last months due to advances in the capability of computing resources with respect to early design reports, especially during the technical downtime after the 2008 incident.

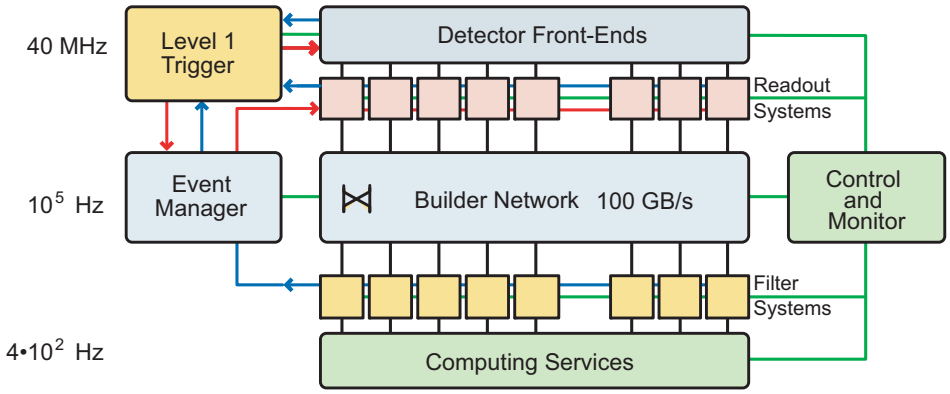

Figure 3.12.: Data acquisition system of the CMS experiment. Improvements in the capability of the computing resources allowed an increase of the final event rate by a factor of $2 - 4$ with respect to previous design reports (taken from [53]).

The first trigger step, called Level 1 trigger, is implemented in hardware and is located next to the detector. The trigger decisions are based on information provided by the calorimeter and the muon system. While the Level 1 decision is made, the whole event data is stored in hardware buffers which are flushed if the event fails the Level 1 filtering. Data samples of interest which pass the first step are forwarded to the next trigger step with a rate of about 100 kHz.

The second trigger step, the High Level Trigger (HLT), is implemented in software. Therefore, it is possible to run algorithms that are identical or – due to time constraints – at least similar to the offline reconstruction that follows later. This kind of trigger also has the advantage that it can be reconfigured during operation and it also benefits from the advances in computing technology. The current continuous output rate for data taking is about 400 events per second, corresponding to a bandwidth utilisation up to 450 MB/s. With additional funding on resources or advancing computer technology this value can be increased over the next years.

3.4. Reconstruction of Physical Objects

The output of the various sub-detectors consists of energy deposits for the calorimetric systems and of single hits, i. e. points of particle interactions in the active detector material, for the other systems, respectively. Therefore, it is necessary to perform a reconstruction and identification of physical objects, e. g. muons and electrons. Hits are connected to tracks, multiple energy deposits are grouped and particles are identified according to the sub-detector where they left a trail.

In the classical reconstruction approach the calorimetric information is not connected to any information from other subsystems. This approach is simple and robust, however the resulting accuracy for hadronic jets, hadronically decaying tau leptons and the missing transverse energy is limited. The Particle Flow reconstruction approach combines the information from all sub-detectors to reconstruct and identify individually charged or neutral, stable particles. Links are created between tracks in the inner tracking system and clusters of energy in the calorimeter which improves the resolution of the energy measurement. Hadronic jets, hadronically decaying tau leptons and the missing transverse energy are then reconstructed based on all stable particles.

The identification algorithms for hadronically decaying tau leptons profit from the extra information provided by the Particle Flow algorithm. As a result the overall performance of the reconstruction at low transverse momenta is improved for all physical objects that involve calorimeter information. It is therefore the preferred reconstruction approach in all current tau analyses and will be used throughout this work. A detailed description of the Particle Flow algorithm and its performance on first data can be found in [59] and [60].

Table 3.3.: Overview of the information used during the reconstruction of different physical objects. The reconstruction algorithms for Particle Flow objects combine information from all sub-detectors.

Object	Tracker	ECAL	HCAL	Muon System
Calorimeter Jets	–	yes	yes	–
Muons	yes	–	–	yes
Particle Flow Objects	yes	yes	yes	yes

3.4.1. Muon Reconstruction

The reconstruction software combines information from the muon system and the silicon tracker to achieve a high reconstruction efficiency and an accurate measurement of the muon momentum.

A first local reconstruction provides track segments based on the measured drift times in the muon chambers. The segments from the innermost layer are used

as seeds for the following muon reconstruction. The state vector of the muon candidate, including momentum, position and direction, is successively improved by taking reconstructed track segments from the adjoining chambers into account. The used Kalman-filter procedure [61, 62, 56] also incorporates the uncertainties on the different track hypotheses. The algorithm iterates through all layers and finally yields a muon trajectory. The energy loss of the muons and scattering in the material between the chambers as well as the inhomogeneous magnetic field are taken into account.

The global muon reconstruction extends the trajectory of the previous standalone reconstruction and matches it with hits in the silicon tracker considering the energy loss and multiple scattering in the detector material, especially in the solenoid and the calorimeter. The extrapolation of the trajectory defines a region of interest within the tracking detector. All hits within this region are used to reconstruct local tracks. If these tracks are compatible with the track from the muon system, a global fit combines the information of the muon chambers and the tracking system into a reconstructed muon referred to as *global muon*.

A determination of the trajectories only based on the hits in the tracking detector and the innermost muon detector layer yields information about muon bremsstrahlung and other energy loss mechanisms. This information improves the reconstruction of muons with large transverse momenta.

In an alternative approach, muons are reconstructed beginning with reconstructed tracks in the silicon tracker system. In the same way as before they are propagated, now outwards to the muon system, and the candidates are matched to locally reconstructed tracks, if available. A final combined fit then yields so-called *tracker muons*. The approach resembles the global muon reconstruction but avoids possible mismatches of muon tracks with tracks in the tracking system. Analyses typically require a successful reconstruction using both methods.

Performance on Data

The precision of the muon momentum reconstruction is directly connected to the knowledge of the alignment of all participating tracking detectors. This task has been tackled already before the start of the LHC by exploiting so-called cosmic muons that originate from collisions of high energetic cosmic particles with molecules in the upper atmosphere. The extended pre-commissioning after the 2008 incident was beneficial for the understanding of the muon reconstruction and the proper alignment of the detector. Due to the alignment with millions of cosmic muons, the relative momentum resolution could be finally measured to be below 2% for muons with a transverse momentum below 100 GeV/c [63]. However these results only hold for muons in the barrel region.

The measurement of the Z line shape allows a determination of the momentum scale resolution for the whole covered range of the pseudorapidity directly from collision data. The relative resolution is reported as $1 - 1.5\%$ for muons with a transverse momentum exceeding 20 GeV/c in the barrel region and less than 6% in

the forward region [64].

Figure 3.13 illustrates the capability of the CMS experiment to reconstruct dimuon resonances. Without any selection criteria on the quality of the reconstructed muons, the well-known resonances are identifiable as well pronounced peaks above the large combinatorial background. Even the first two excited states of the Upsilon meson are distinguishable. It is noteworthy that this remarkable degree of accuracy in the muon momentum reconstruction cannot be achieved by ATLAS, the main competing experiment [65].

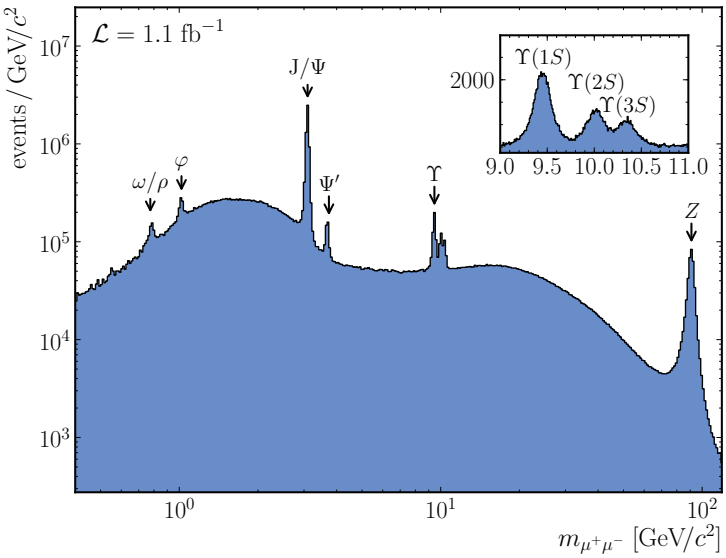

Figure 3.13.: Invariant mass spectrum for pairs of muons that have been reconstructed based on information from the tracking detector and the muon detector. The lack of quality and isolation criteria leads to a large background contribution, but the known resonances which predominantly decay into muons are well pronounced. The visibility of the first three Upsilon states demonstrates the remarkable precision of the muon reconstruction. It is important to note that the ratio for the number of entries in different bins, i. e. the overall shape of the background contribution, depends on the actual compilation of the trigger algorithms used for the data taking.

3.4.2. Tau Reconstruction and Identification

Tau leptons are of great importance for many analyses, especially in searches for new physical phenomena. Unlike muons, tau leptons are not limited to decays into lighter leptons, i. e. muons and electrons ($\mathrm{BR}\,(\tau \to l) \approx 0.30$), they may also decay into charged mesons generally accompanied by neutral pions ($\mathrm{BR}\,(\tau \to h) \approx 0.68$). The latter decay modes show up in the detector in a similar way as hadronic jets originating from quarks and gluons. They are thus referred to as tau-jets. As the production cross section for QCD jets exceeds the one for tau lepton production

by some orders of magnitude, it is necessary to identify tau jets precisely while maintaining a low rate of false identification. The Particle Flow algorithm is well suited as it accumulates information from the tracking system and the calorimeter systems consistently.

The tau reconstruction begins with a jet reconstruction (see Section 3.4.3). A threshold of $p_{\mathrm{T}}^{j} > 0.5$ GeV/c for the jet constituents hereby reduces the effect of pile-up events and the effect of the underlying event. All jets with a leading track near the jet axis

$$\Delta R\,(\mathrm{track}, \mathrm{jet}) < 0.1 \quad \text{with} \quad \Delta R = \sqrt{\Delta\eta + \Delta\phi}$$

and a transverse momentum above 5 GeV/c are then considered as tau candidates. Subsequently, various tau identification algorithms can be exploited to further filter this collection yielding a purer sample of tau candidates.

Isolation-based Classification

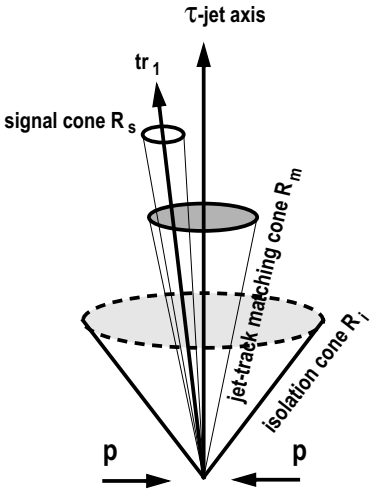

Figure 3.14.: Illustration of the isolation cone which is used for the isolation-based identification of tau leptons (taken from [53]). The signal cone is defined around the leading track of the tau-jet candidate. All contributions within the signal cone are attributed to the tau lepton decay. The isolation quantity is only calculated in the remaining volume of the larger isolation cone.

Hadronically decaying tau leptons have a characteristic, narrow shape that allows a distinction from quark and gluon induced jets. It is therefore useful to define a small signal cone around the leading tau-track with all potential tau decay products inside and a larger isolation cone (usually $\Delta R_{\mathrm{iso}} = 0.5$) as shown in Figure 3.14. A tau candidate is rejected if the space between both cones contains a charged hadron with $p_{\mathrm{T}} > 1$ GeV/c or a photon with $E_{\mathrm{T}} > 1.5$ GeV. The performance of the algorithm can be improved when the fixed signal cone is replaced by a

variable, shrinking cone. The radius of this cone is calculated as a function of the jet transverse momentum reflecting the usually narrower shape of high energetic tau jets:

$$\Delta R_{\text{shrinking}} = \frac{5.0 \text{ GeV}}{E_{\text{T}}} \quad \text{with} \quad 0.07 \leq \Delta R \leq 0.15 \; .$$

All cone sizes have been determined in studies on samples of simulated events.

Tau Neural Classifier

The Tau Neural Classifier (TaNC) [66] is an approach based on neural networks. This classification algorithm identifies specific, individual decay modes. It exploits intermediate resonances that usually occur during hadronic tau lepton decays. The identification and reconstruction of neutral pions which decay instantaneously into photon pairs is a crucial step of the preprocessing.

Afterwards an ensemble of neural networks classifies the tau candidates, one network for each of the five dominant decay modes (see Table 3.4). The classification yields a continuous quantity that can be used for the definition of specific working points, i. e. a pair of tau identification efficiency and the impurity arising from quark and gluon induced jets. The working points have been defined beforehand for 20 GeV/c < $p_{\text{T}}^{\text{jet}}$ < 50 GeV/c to resemble typical tau transverse momenta from Z boson decays.

Table 3.4.: Overview of the tau decay modes that are covered by the Tau Neural Classifier algorithm (taken from [66]).

Visible Decay Products	Resonance	Fraction
$\pi^{\pm}$	-	10.9%
$\pi^{\pm}\pi^{0}$	ρ	25.5%
$\pi^{\pm}\pi^{0}\pi^{0}$	a_1	9.3%
$\pi^{\pm}\pi^{\pm}\pi^{\mp}$	a_1	9.0%
$\pi^{\pm}\pi^{\pm}\pi^{\mp}\pi^{0}$	a_1	4.5%
Covered hadronic decay modes		59.2%
Other hadronic decay modes		5.6%

Hadron Plus Strips classifier

The Hadron Plus Strips [67] (HPS) algorithm extends the idea of the simple isolation based tau identification (see Section 3.4.2). It is designed for an optimal reconstruction of neutral pions within the tau decay. The algorithm collects electromagnetic particles in strips of the η-ϕ plane ($\Delta\eta = 0.05$, $\Delta\phi = 0.20$) iteratively,

comparable to a jet clustering algorithm. The strip form is motivated by the characteristic signature of photon conversion in the calorimeter, where the energy deposits are spread in the azimuthal direction due to the magnetic field. A neutral pion can give rise to no strip if it is low energetic, one strip if the two photons from its decay are close together or two strips if they are well separated.

The HPS tau identification algorithm attempts to identify decay modes with one charged hadron and up to two strips, or three charged hadrons without any reconstructed strip. The four-vector sum of combinations of strips and hadrons have to be compatible with the π^0, ρ or a_1 masses, otherwise they are rejected. In a last step, all charged hadrons and photons that are not associated to a reconstructed tau decay mode are taken into account for the isolation criterion.

While the simple isolation-based tau lepton identification restricts itself to geometrically defined cones, the HPS algorithm defines a variable isolation area by reconstructing the tau decay mode.

Tau Identification Performance

The reconstruction and identification of hadronically decaying tau leptons has been studied for the HPS and the TaNC algorithms on collision data from 2010 [67]. The identification efficiency is reported as 50% for hadronic taus and a tau-fake rate from other hadronic decays, e. g. gluon and quark induced jets, as 1%. With constraints on the $\mathrm{Z} \to ee, \mu\mu$ cross sections, the uncertainty on the tau identification efficiency yields 7%. Finally the tau energy scale is compatible with the expectations from simulated events with a scale uncertainty below 3%.

3.4.3. Jet Reconstruction

Quarks and gluons induce collimated streams of charged and neutral particles. Algorithms group the four-vectors of tracks of these particles or the measured energy deposits in the calorimeter cells, respectively, to so-called jets.

The result of a jet algorithm has to be stable towards small variations of the input. A low energetic particle between two stable jet candidates may not induce a merging into one single jet candidate. This property is called infra-red safety (see bottom plot in Figure 3.15).

Hadronic jets can radiate collinear gluons and as a result of this splitting, the energy of the seeds can be below the predefined threshold for jet candidate seeds (see upper plot in Figure 3.15). Thus, the jet would not be reconstructed and the final result would depend on the splitting processes. Especially for comparisons with theoretical models, it is important that algorithms are immune to collinear radiation. They are referred to as collinear safe algorithms (see [68, 69] for details).

In general, there are two classes of jet reconstruction algorithms available:

- **Cone type algorithms** cluster objects inside a geometrically defined cone in the η-ϕ-space, the cone size is hereby a characteristic quantity. The algo-

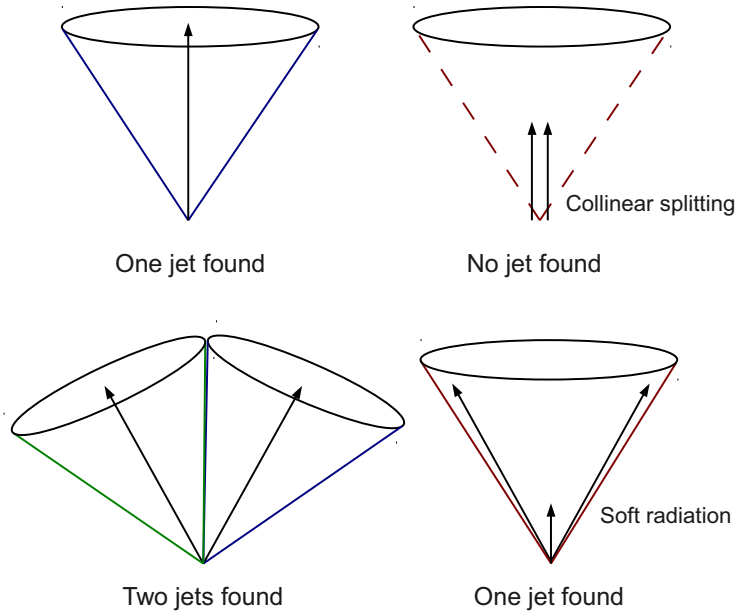

Figure 3.15.: Illustration [68] of collinear (top) and infra-red (bottom) unsafe jet clustering algorithms. In the first case, a jet is not reconstructed after a splitting of the energy into two parts wherein the energy of both parts is below the energy threshold of the chosen jet algorithm. In the second case, a small extra energy contribution induces a merging of two nearby jets. Both behaviour patterns are unwanted for physics analyses.

rithms usually start with high energetic seeds and continue with a merging and splitting of jet candidates until a final stable set of jets is found. Prominent cone-type algorithms are MidPoint [70] and IterativeCone. They are both not infra-red safe and thus not used within the CMS experiment. SISCone [71] is an infra-red safe algorithm which works without seeds. However the infra-red safety is bought with a larger complexity of the algorithm and the execution time grows with $N^2 \ln N$ where N is the multiplicity of objects to be clustered. As a consequence, the CMS collaboration has replaced all cone type algorithms by clustering algorithms that feature infra-red and collinear safety as well as a small complexity.

- In **clustering algorithms** objects are iteratively grouped based on a distance measure that quantifies the separation of two objects. The measure is based on the four-momentum vector of the object, so the invariant mass is naturally taken into account. In contrast to cone-based algorithms, this clustering does not result in fixed geometrical shapes. In a simple approach, the complexity of a distance-ranked algorithm is N^3 where N denotes again the multiplicity of objects. FastJet [72] is an optimized implementation on the basis of Voronoi-diagrams and reduces the complexity down to $N \ln N$. The CMS collaboration implemented the k_T-algorithm [73] and the anti-k_T-

algorithm [74] as representatives of the clustering algorithms in the CMSSW framework.

4. Software Tools

4.1. Monte Carlo Event Generation

The generation of events is based on the probabilistic evaluation of the underlying mathematical description of a specific physical process. The probability of an event to occur is given by the cross section of the specific event. For hadron-hadron collisions it is a convolution of the partonic cross section $d\sigma_{ij\to l_1 l_2}$ and the parton distribution function. It reads for $2 \to 2$ processes:

$$\mathrm{d}\sigma = \sum_{ij} \int \mathrm{d}x_1 \mathrm{d}x_2 f_i(x_1, Q^2) f_j(x_2, Q^2)\, \mathrm{d}\sigma_{ij\to l_1 l_2}(x_1, x_2)$$

The summation runs over all partons and f_i denotes the probability to obtain a parton i carrying the fraction x of the longitudinal momentum of the hadron at scale Q^2. The momentum transfer is typically large for the hard process in high energy collisions, i. e. the main initial interaction between two partons. As a consequence, the partonic cross section can be evaluated by means of pertubation theory.

However it is not possible to perform such a calculation for a complete event. Color charge carrying particles lead to an overwhelming complexity and at small momentrum transfers pertubation theory is not applicable. As a consequence, the evolution of partons is performed with approximative models (see below).

The CMS collaboration employs a number of different generators, among them are Pythia [75], Herwig [76], MadGraph [77], VBFNLO [78] and Powheg [79]. While the last three focus on the calculation of matrix elements, Pythia and Herwig also include models for the QCD evolution of partons.

Pythia

Pythia [75] is a general-purpose Monte Carlo generator written in Fortran 77 for generating events in hadron and lepton collisions. It has been developed since 1978 and is thus well tested and widely accepted in the high energy physics community. Pythia 8, the successor of Pythia 6 is completely written in C++, but it is still under testing at the time of writing. The majority of the officially produced Monte Carlo events is based on Pythia 6.4.

Typically, two incoming particles with a certain centre-of-mass energy and a known partonic substructure are used as input. Pythia provides a large amount of $2 \to 2$ and some $2 \to 3$ processes at leading order for the hard process based on analytical calculations and various QCD-based models. The radiation of gluons by coloured objects, e. g. quarks and gluons, is handled in the parton shower

algorithms [80, 81]. Hereby, a single parton can be splitted into several partons without a time-consuming calculation of higher-order matrix elements. The subsequent hadronisation of the partons is performed on the basis of the Lund string model [75], in which coloured objects are attached to virtual strings that break when objects move apart and the distance becomes larger than about 1 fm creating new $q\bar{q}$ pairs.

In certain decays, particles are polarised and the decay products show a non-isotropic angular distribution. By default, PYTHIA does not take such effects into account during the hadronisation but it can use external libraries with other models, e. g. TAUOLA for τ-decays.

PYTHIA also allows the use of external parton-level generators such as POWHEG (see below) with better models for the hard sub-processes, e. g. $q\bar{q} \to \mathrm{Z}+\mathrm{jets}$. Some of these packages include exact calculations of Feynman diagrams up to a certain order and include correct interference terms or angular distributions. This approach gives a more accurate description of final-states with high jet multiplicities than a calculation only with approximative parton shower models.

The remaining particles of the protons, i. e. the spectator quarks and gluons, are processed by PYTHIA's underlying event models. These models also include the possibility to simulate multiple parton interactions. PYTHIA uses customisable sets of parameters for its phenomenological model to describe the underlying event. These parameter sets (also called *tunes*) have been derived from measurements at LEP and Tevatron. Meanwhile, there exist also tunes which have been complemented with first studies at the LHC. By default PYTHIA uses the tune D6T [82] which is based on the parton distribution function CTEQ6LL [83]. As this tune is not compatible with POWHEG's demand for p_{T}-ordered showers (see below) the newly developed tune Z2 [84] is used. It has been derived from collisions at 900 GeV and 7 TeV at the LHC. Although recent studies [68] suggest that this tune is not optimal in all details, it is the standard tune within the CMS collaboration.

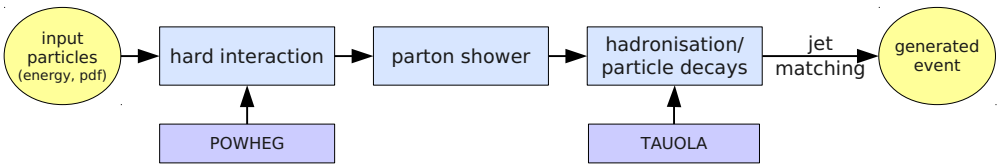

Figure 4.1.: General workflow of PYTHIA: In a first step, a hard process is simulated for the specified input particles, external libraries can be involved at this point for more detailed descriptions of the hard interaction (e. g. POWHEG). Coloured objects are processed subsequently by a parton shower method, the decay of specific particles can be performed again by external libraries (e. g. TAUOLA). For some processes with a defined number of jets in the final state it is necessary to apply a jet matching algorithm to avoid double-counting of jets when combining the matrix-element methods for the hard process and the parton shower models. This can be done by CMSSW.

PYTHIA is fully intergrated into the software framework of the CMS experiment. Therefore, it can be controlled with plain configuration files instead of raw FOR-

TRAN commands. A wrapper from FORTRAN to C/C++ allows direct calls of PYTHIA functions from user modules inside the framework. The results of the generated events are stored in a standardised format (HEPMC) so it can be processed by other modules in the software framework of CMS such as a detector simulation.

Tauola

TAUOLA [85, 86] is a package plugable into PYTHIA which is capable of simulating τ-decays in more than twenty decay channels. In contrast to PYTHIA, it takes spin and polarisation of the taus into account depending on the originating production process. Therefore, tau pairs decay properly pairwise. Radiative corrections are simulated by TAUOLA using the PHOTOS [87] package.

Matrix Elements at Next-to-Leading Order Precision

As mentioned earlier, PYTHIA provides only evaluations of the matrix element at leading order precision. For precise measurements, e. g. with Z and W bosons, it is necessary, or at least desirable, to have exact calculations at next-to-leading order (NLO) precision. This also requires a parton density function that has been determined with calculation at next-to-leading order. However, using a NLO matrix element with the parton shower of PYTHIA without any modifications would lead to inaccurate results (so-called overcounting) since the shower algorithm already includes some approximations for NLO effects.

MC@NLO [88] approaches this problem with a subtraction of the approximated corrections of the subsequently applied shower algorithm from the exact NLO result at the level of the matrix element. It is obvious that this anticipated correction has to be determined once for each version of a shower algorithm. A statistical weight is assigned to each generated event to reflect the calculated correction. As a side effect of this approach, events can even get a negative weight. Although all physical distributions will have positive values for an infinite number of generated events this behaviour cannot be guaranteed in case of limited statistics, e. g. after the application of very selective cuts.

POWHEG[1] [79] is a shower independent approach which by-passes negative event weights and the resulting difficulties in the interpretation of such results. POWHEG generates the hardest radiation in a way that only positive weights appear and then passes the event to a p_{T}-ordered shower algorithm that leaves the already existing radiation untouched. With some modifications it is also possible to use shower libraries with angular-ordered shower algorithms such as HERWIG.

POWHEG offers a number of matrix elements at next-to-leading order precision. This includes the production of single and double W and Z boson [89, 90], top quark production and also the production of Higgs bosons via gluon fusion [91] or vector boson fusion [92]. POWHEG is used for all electroweak signal and background processes in this thesis unless otherwise stated.

[1] POsitive Weight Hardest Emission Generator

4.2. ROOT

ROOT [93] is an object-oriented framework for large scale data analysis widely used in the high energy physics community. In contrast to its FORTRAN-based predecessor PAW, ROOT is written in C++ and uses an object-oriented approach which simplifies its application in user programs. ROOT can be used interactively or via its programming interface.

Among other things, ROOT is capable of creating histograms in various ways and it allows for fits of arbitrary functions. Additionally, it provides classes for comprehensive data input and output operations including storage of tuples of values or even user-defined classes. This serialisation capability also comprehends sophisticated methods to reduce the file size and to decrease the access time for operations that cover only portions of the overall data. Recent developments on parallel data processing with distributed computing extend ROOT's capabilities to handle even very large data samples [94].

4.3. The CMSSW Application Framework

The CMS collaboration decided to provide a framework that covers all steps of an analysis in the experiment, simply called CMS software (CMSSW). This includes the generation and the simulation of events but also analysis steps and the processing of data from the experiment. This approach contrasts the previous software architecture where different applications served for very specific tasks.

The CMS software model facilitates the subsequent execution of different tasks and simplifies comparison studies since algorithms or parameters can be changed without any difficulty. Furthermore, analysis groups can easily provide common standard configurations to other groups. Even less experienced users can utilise CMSSW for full analyses without facing conversion problems or incompatibilities between different programs.

Modular Architecture

The CMSSW framework offers the possibility to process event data with different modules, each covering a specific task. The user passes a job configuration file to the main CMSSW executable and the framework then parses this configuration file to load all necessary modules and libraries dynamically. Parameter sets within the configuration file can be modified without the need of compiling the executed modules again.

A source module provides the events that are to be processed at the beginning of each CMSSW job. They can either be read from a file or can be generated on the fly by a Monte Carlo generator. During the data taking process the data acquisition system acts as data source.

The event data is then passed sequentially through all specified modules which can be categorized into three different classes: *Filter modules* pass or reject events

that match specified requirements. There are for instance modules that reject all events which contain less than two reconstructed muons. *Producer modules* add new objects to the event. All reconstruction algorithms belong to this category but users can also write own modules which produce objects and quantities that are derived from existing information. It is noteworthy that objects can also be intermediate or transient, i. e. they are only processed by subsequent modules but not written to disk at any time. Both filter and producer modules have access to the data of all previously executed models. *Analyzer modules* are the third category of modules. They are used for studies, i. e. they generate and store final quantities in the form of histograms and graphs.

For later processing in stand-alone programs, it is also possible to store a condensed output of the data as collections of quantities (so-called `ntuple`). As their file sizes are much smaller than for the original data samples and the loading of the framework can be avoided, studies on ntuples feature in general shorter turn-around times.

Detector Simulation

The simulation of the passage of particles created by a Monte Carlo generator through the detector is fully integrated into the CMSSW framework. It facilitates the GEANT 4 [95, 96] package which can simulate the interaction of particles with matter in great detail. GEANT 4 is developed by an international collaboration of scientist ranging from medicine to high energy physics combining the knowledge on various types of interactions into one general purpose product. The modelling of a particle traversing matter includes all important physical processes such as bremsstrahlung, Compton and Rayleight scattering or scintillation.

The resulting information on the position and strength of the interaction with the detector material, e. g. hits in the silicon detectors or emitted photons in the calorimeter, is then processed by a simulation of the actual readout electronics. This digitisation step also incorporates the modelling of electronic noise and intrinsic detection thresholds. From a technical point of view, the result of this step is identical to the output of the CMS detector and can be processed by the same reconstruction algorithms that yield the reconstructed physical objects on real data.

The structure of the framework also allows for an easy modification of detector components and their performance. Misalignment scenarios for the tracking detector can be applied without a complete re-simulation but just by changing the coordinates or the orientation of detector cells. This modularity simplifies studies of systematic detector effects.

Fast Simulation

The full simulation is complemented by a fast simulation (called FastSim) which is simplified drastically to gain speed. The interactions of particles which traverse detector material are not calculated in detail. Instead, the trajectories of the par-

ticles are smeared using parameterisations that have been deduced by comparisons with full simulation or real data. The simulation thus basically consists of table look-ups and, as a result, the simulation needs only a fraction of the time that the full simulation needs (about 10^{-3}) hereby justifying its name.

Event Data Model

An integral part of the software architecture is the Event Data Modell (EDM). It is a container for arbitrary C++ objects, e. g. raw data and reconstructed physical objects (e. g. particles, missing transverse energy) or derived quantities of an event. All parts of a production or analysis chain can access all available data of an event and add new objects to the event. The events are stored in a tree structure in files using ROOT libraries. Therefore, they can also be accessed directly via ROOT using the Framework Lite (FWLite) libraries.

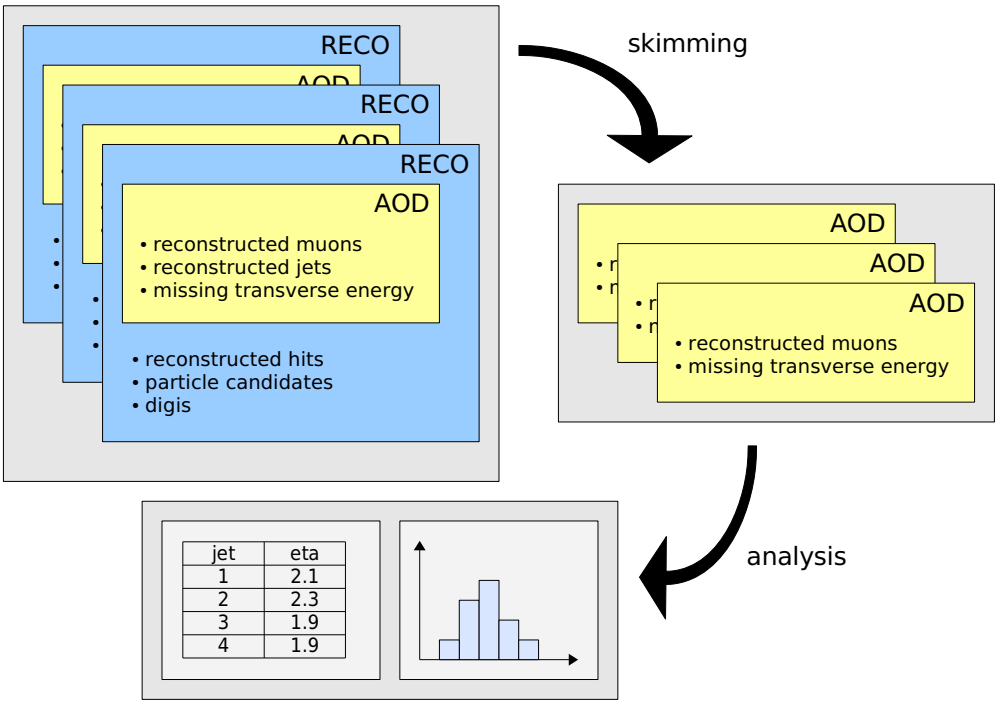

Figure 4.2.: Model of a typical analysis with CMSSW: A reduction of the amount of data (skimming) to select only objects needed for the analysis reduces the storage consumption and the execution time. The final analysis module then produces ouput files with histograms, tables or n-tuples.

The container design allows for a granular refining of the data (in the CMS collaboration usually referred to as *skimming*). The reduction to high level physics objects saves storage space and reduces the runtime of the analysis. CMSSW has also some pre-defined data tier, i. e. sets with specific objects. Among them are the data tier RECO which includes all reconstructed data objects, whereas the data

tier AOD (Analysis Object Data) is only a subset with physical objects needed for a particular analysis.

Framework Services

As in every other scientific experiement, CMS has to do a precise and persistent book-keeping of the conditions during the data taking process. Among others, this includes the magnetic field configuration and the specific state of the sub-detectors, e. g. the applied voltage in the inner tracking detector. Additionally, it is necessary to store information on the calibration and the alignment of the various detector components. In contrast to the aforementioned state observables, these quantities are determined concurrently to the data taking by different working groups and they are subject to regular updates.

Albeit the metadata is in general time-dependent, there is no direct connection to a single event; it would complicate the data processing if these parameters were stored together with the detector output, especially in case of updates or corrections. As a consequence, all information on the detector conditions is stored in a central database at CERN [97].

As soon as an event is processed, the CMSSW framework automatically contacts the central database and retrieves the set of metadata that is required by the executed modules and that corresponds to the current run and luminosity section (see figure 4.3).

An elaborated versioning mechanism also enables the different analysis groups to use and compare consistent sets of alignment and calibration constants in their studies. Beside the calibration of jet energies, the configuration of the High Level Trigger is an important example of such a set of metadata. The High Level Trigger appears again in the corresponding chapter in this thesis (see Section 6).

4.4. World-wide LHC Computing Grid

The CMS experiment has to cope with a large amount of data produced by both Monte Carlo studies and the experiment itself. All data has to be stored reliably and in an organised way. The recorded collision data has to be reprocessed from time to time to reflect the most recent knowledge on the detector conditions.

The equal and unrestricted access of all participating scientists to all available data is one aim of the CMS computing model. At the same time, certain computing tasks, e. g. the reconstruction of events, need priority access to resources as they are valuable for the whole collaboration.

The high energy physics community chose a model with geographically distributed resources which are accessible via common interfaces. This kind of distributed computing is called grid computing. In analogy to the electricity grid, the computing grid shall distribute the workload equally to all connected computing resources and the underlying software layers have to be transparent to the user who uses only a standardised set of commands. The different computing centres

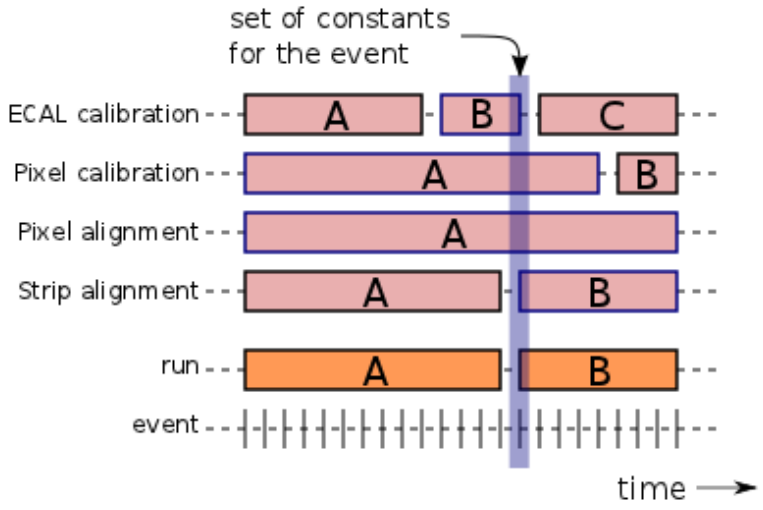

Figure 4.3.: The CMSSW framework automatically provides the correct metadata for each event by accessing a central server hosting the conditions information. The time interval during which a set of parameters is valid is called interval of validity.

are located all over the world. All sites that participate in LHC experiments build together the Worldwide LHC Computing Grid (WLCG).

WLCG structure

The computing model is organised hierarchically in four tiers with different standards and commitments for each layer. The Tier 0 at CERN directly receives data from the data acquistion systems of the experiments. It archives the data on tape storage and runs the event reconstruction in real-time. Both raw and reconstructed data are then continuously transferred to Tier 1 sites. These regional computing centres provide large storage and computing resources. They are used for reconstruction, skimming and other time-consuming tasks. At the same time they act as a backup instance for the Tier 0.

Beside these tasks, Tier 1 centres also transfer the data to subordinated Tier 2 sites for user analyses. Additionally, they contribute to processor-intensive tasks such as Monte Carlo production and offer computing resources to users and analysis groups. Although there are less stringent requirements on the provided storage space, Tier 2 sites have to fulfill several service level agreements as they are fully embedded into offical CMS computing tasks.

Tier 3 sites are the smallest unit within the computing model. These small-scale clusters contribute without specific obligations and offer resources mainly to local groups. They are well suited for private Monte Carlo productions and interactive analyses. Broadband connections allow fast data transfers from the affiliated Tier 2 centre.

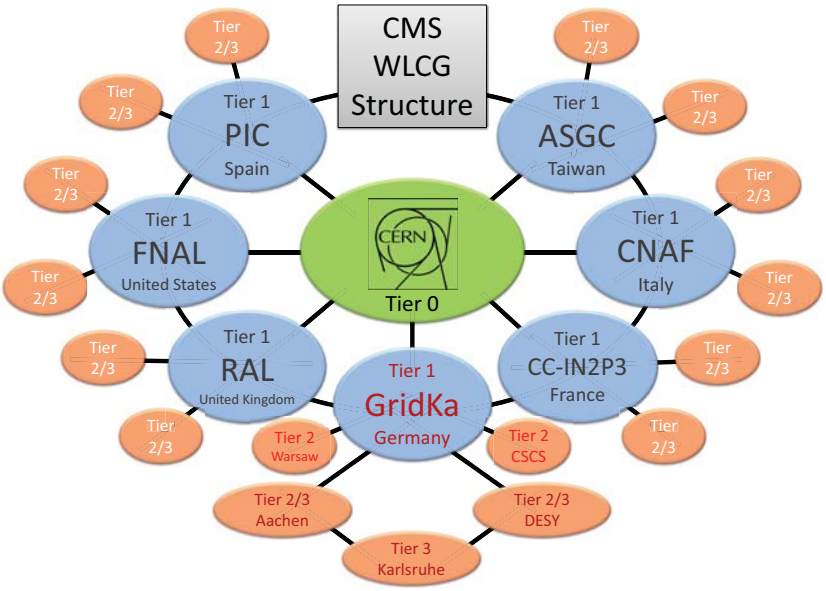

Figure 4.4.: Tiered structure of the CMS part of the WLCG with the central Tier 0 at CERN. Although not shown in this picture, Tier 2 sites can access data from every Tier 1 site (taken from [98]).

GRID Services

The GRID computing system offers access to all computing resources and data via standardised services in a simple way. The underlying structure of the GRID is abstracted using a mediating software layer, the grid middleware.

The authentication of users within the grid and assignment of access rights for resources are carried out via their membership in virtual organisations (VO). These are abstract groups for different subjects, e. g. defined by a scientific project or a regional group. The actual authentication is based on personalised certificates with public-key cryptography using the X.509 standard [99]. A VOMS[2] server delivers on user request a temporary certificate, a so-called grid proxy, that identifies the user towards grid services.

The Workload Management Service (WMS) is another crucial part of the grid infrastructure. Each VO provides WMS servers which receive user jobs and forward them to an appropriate computing centre. To do so, they have to query the Data Location System to determine computing sites that host the necessary data samples if required by the job. The so-called top-level BDII[3] server provides information about the connected computing centres to the WMS server, e. g. the current utilisation, to allow load balancing among all compatible sites.

The job is then handed over to a Computing Element (see below) at a particu-

[2] Virtual Organisation Membership Service
[3] Berkely Database Information Index

lar site which is the site that satisfies the requirements imposed by the user and presumably allows the fastest job execution. The transfer of small output files is done via the WMS server as well, while large files should be copied manually by the user directly from or to Storage Elements (see below). Furthermore, the WMS server provides information about the status of a job to the user, e. g. the return code on the completion of the job.

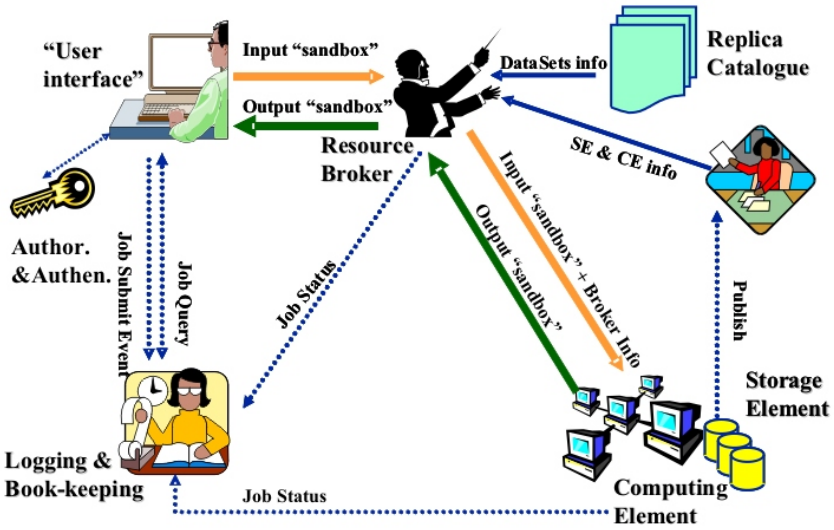

Figure 4.5.: Overview of the submission of a job to the GRID.

Site Services

Each site has to provide several services to participate in the WLCG. The Computing Element (CE) is a server which mediates between the WMS server and the local batch queueing system which then distributes the job to a worker node where it is finally being executed. The CE receives jobs from the WMS, sends some defined output files back to the WMS and also provides information about the status of submitted jobs.

In analogy to the CE, the Storage Element (SE) is the connection between the GRID and the local mass storage system. The SE organises the bookkeeping of all available data on hard disks and tapes and it translates the standard grid commands for file operations into the language of the specific storage system.

The User Interface (UI) provides local users access to the GRID. It consists of several tools for user authentication and job management. This includes the

submission and monitoring of jobs as well as the transfer of data files to storage elements.

Job Submission Tools

A grid job requires a configuration file that specifies its needs and an archive with the actual payload, i. e. a set of executables, configuration files or scripts that are to be run on the worker node. The processing of a task comprehends typically a large number of jobs (100–10000), so a manual preparation and management of that many jobs would obviously be fault-prone and exhausting. The CMS collaboration provides CRAB (CMS Remote Analysis Builder, [100]) as the official grid tool. It takes care of all steps of the job submission, however it is restricted to jobs within the CMSSW framework.

Grid-Control [101, 102] is an alternative tool that has been developed in Karlsruhe over the past few years. It features the submission of jobs that invoke the CMSSW framework in the same way as jobs that consist of stand-alone executables. Therefore, it also allows to run on local user data or to do statistical toy Monte Carlo tests. Furthermore, Grid-Control allows the utilization of resources in local clusters or even on the local machine in a transparent way which ensures a consistent workflow at all steps of an analysis. The modular architecture even facilitates an extensive parameterization of all kinds of jobs. Due to its flexibility and reliability, Grid-Control has been used throughout this thesis for all kind of distributed data processing.

5. Study of Z Boson Decays into Muons

Since its discovery in 1983, the Z boson has been subject to studies at various experiments [17, 18, 103, 104]. The LEP experiments were able to measure the properties of the Z boson with an unprecedented precision. With the start of the CMS experiment, the Z boson is a prominent candidate for the commissioning of the detector. After this first phase of the re-discovery of the Standard Model, the Z boson will be a dominant background contribution to searches for the Higgs boson, heavy Z-like resonances and other new models beyond the current Standard Model.

Due to its design the CMS experiment is well suited for a measurement of Z boson decays into two muons. The ability to reconstruct muons precisely is a good opportunity to impose constraints on parton distribution functions and offer an alternative luminosity measurement – assuming that experimental and theoretical uncertainties are well understood.

This chapter introduces the characteristics of $\mathrm{Z} \to \mu^+\mu^-$ events and continues with a measurement of the production cross section on the 2010 data sample. This task requires a profound understanding of the performance of muon High Level Trigger algorithms in data and simulated samples. The following chapter is dedicated to this particular study. Both chapters are the basis for the estimation of $\mathrm{Z} \to \tau^+\tau^-$ events in Section 7.

5.1. Event Topology

The decay of a Z boson into two muons is a process with a characteristic final state. The two muons carry a distinct transverse momentum with a peak around $p_{\mathrm{T}}^{\mu} = 40\ \mathrm{GeV}/c$ as shown in Figure 5.1 which can easily be identified with the CMS detector. Furthermore, the CMS detector exhibits a very good momentum resolution for reconstructed muons in this particular region of the phase space. The two muons are in general not accompanied by additional activity as they originate from an electroweak production process. Due to the lack of neutrinos in the final state, the hard process itself causes no missing transverse energy.

Throughout this work the contribution from the exchange of a virtual photon will not be mentioned explicitly for the sake of simplicity, albeit it is always included in the measurement unless otherwise stated.

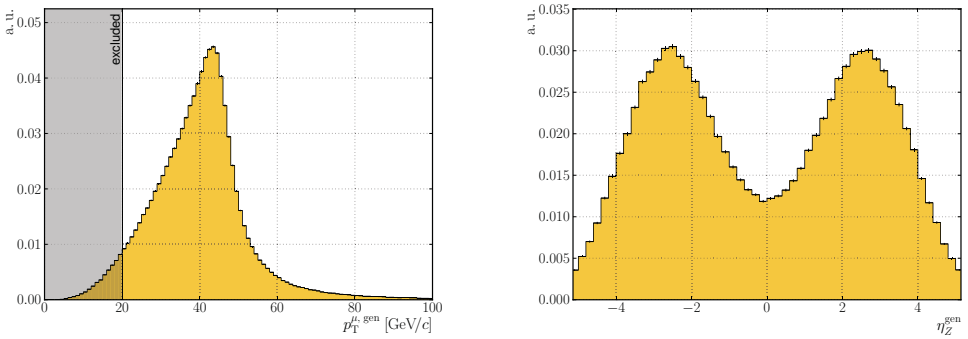

Figure 5.1.: Distribution of the muon transverse momentum (left) and the Z boson pseudorapidity at generator level for Z bosons within the defined acceptance region. Both distributions are normalised to unity. The shaded area in the left plot indicates the range which is excluded by the kinematical acceptance definition

5.2. Event Generation

Physics analyses usually include comparisons of quantities and their distributions with simulated events to cross-check the results of the real data sample. This projection also allows an estimation of the sensitivity for a specific study. In some cases, it is also necessary to apply efficiency correction factors that have to be determined beforehand using samples of simulated events. As the production of such samples implies enormous computational efforts, the CMS collaboration employs a central production. Technical details on the conditions used for the event generation in the official product campaigned can be found in Section A.2.

5.2.1. Signal Processes

The signal process for this analysis has been generated in two steps: the matrix element for the hard process, $qq \to \mathrm{Z} \to \mu\mu$ is generated with POWHEG. The calculation is performed at next-to-leading order in α_s with CT10 [105] as parton density function (PDF). The showering process is done by PYTHIA in a separate, second step. The underlying event is simulated with the Z2 tune which is similar to the Z1 tune [106], but uses CTEQ6L1 [107] as parton density function.

5.2.2. Background Processes

Several processes are able to mimic a final state with two muons or exhibit two real muons in the final state. For this study, they are grouped in three distinct sets: production of electroweak gauge bosons (except $\mathrm{Z} \to \mu^+\mu^-$), $t\bar{t}$ pairs and QCD-induced muons. Table 5.1 lists the main data samples. Special data samples for dedicated studies are mentioned separately and can be found in Section A.2.

Electroweak Gauge Bosons

The dominant background contribution stems from Z bosons that decay into tau pairs with subsequent decays into two muons, i. e. $\mathrm{Z} \to \tau^+\tau^- \to \mu^+\mu^- + 4\nu$. However, the two muons yield a smaller invariant mass compared to the nominal Z mass since the occurring neutrinos carry away a significant amount of energy. Due to the additional branching ratio $\mathrm{BR}(\tau \to \mu)$ the production cross section is much smaller. The $\mathrm{Z} \to \tau^+\tau^-$ sample is produced similarly to the $\mathrm{Z} \to \mu^+\mu^-$ sample, only the tau decays are simulated with TAUOLA.

Although W Z and Z Z decays feature real Z bosons, they are considered as background contribution in this analysis. Along with W W decays, the samples are produced in leading order of α_s with PYTHIA. The contributions from the real Z bosons are visible in the invariant mass distribution as a small peak around the nominal Z mass.

The production of single W bosons complements the set of electroweak processes. Although it gives only rise to single muons from the W decay, independently produced muons can act as second muon. As for the Z samples, the W samples are produced with POWHEG.

$t\bar{t}$ Production

An additional background contribution arises from the production and the subsequent decay of $t\bar{t}$ pairs. Almost all top quarks decay into a bottom quark and a W boson. The latter decays into a muon with a probability of roughly 11% [4], so about 1% of the $t\bar{t}$ pairs contain two muons in the final state. This topology is similar to the signal process as both muons originate from an electroweak decay. However, since the two muons do not originate directly from the same mother particle, the invariant mass distribution shows no distinct peak but a rather flat behaviour.

QCD Background

The scattering of quarks and gluons in proton-proton collisions gives rise to a large amount of hadronic jets. A great variety of particles can occur within these jets, including muons. Unlike the previously described processes, these muons are in general accompanied by other charged and neutral particles in the same spatial direction. Additionally, the transverse momentum of the muons is usually much smaller than for the signal process. Although these properties allow a good discrimination, this contribution has to be studied as the production cross section is 50 times larger than for the signal process.

The large production cross section and the rare occurrence of muons with a distinct muon transverse momentum demands a restriction of the phase space at the generator step. All generated events feature an outgoing parton with $\hat{p}_\mathrm{T} = 20$ GeV/c and at least one muon with $p_\mathrm{T}^\mu > 15$ GeV/c. Without these cuts, the majority of the simulated events would be lost after the kinematical selection of the first muon.

Table 5.1.: Main data sets and Monte Carlo samples for both signal and background processes used in the $Z \to \mu^+\mu^-$ analysis. The cross sections σ_{prod} for the electroweak processes are calculated at next-to-next-to-leading order, the cross section of $t\bar{t}$ at next-to-leading and the QCD cross section is given at leading order. All samples have been created in the official production campaign in fall 2010.

Dataset	Events	σ_{prod} [pb]	$\mathcal{L}$ [pb^{-1}]
Muon dataset (2010A)	51 860 222	–	3.1
Muon dataset (2010B)	33 470 281	–	32.9
$Z \to \mu^+\mu^-$ (POWHEG)	1 998 931	1 702	1 199.8
$Z \to \tau^+\tau^-$ (POWHEG)	1 993 603	1 702	1 196.6
$W^+ \to \mu^+\nu$ (POWHEG)	1 991 320	6 152	323.7
$W^- \to \mu^-\nu$ (POWHEG)	1 996 548	4 286	465.8
$t\bar{t}$ + jets (POWHEG)	999 909	65.83	15 189.3
W W (PYTHIA)	2 061 760	27.8	73 634.3
W Z (PYTHIA)	2 194 752	10.5	209 024.0
Z Z (PYTHIA)	2 113 368	4.3	491 480.9
μ-enriched QCD (PYTHIA)	29 504 866	84 679	370.3
$\hat{p}_{\text{T}} = 20$ GeV/c, $p_{\text{T}}^{\mu} > 15$ GeV/c			

5.3. Event Selection

The event selection expoits the characteristic event topology of typical $Z \to \mu^+\mu^-$ decays. After a pre-selection of the events by the trigger system, stringent selection criteria are imposed on the reconstruction quality of the reconstructed muon candidates and their kinematic properties. The selection concludes with an isolation criterion for the muons.

5.3.1. Online Event Selection

The online event selection is based on a single muon trigger, i. e. an algorithm selecting interesting events for permanent storage based on the presence of at least one muon with a distinct minimum transverse momentum. The threshold for the transverse momentum was being raised during the 2010 data taking period to cope with the increasing beam intensity and the limited bandwidth of the storage systems as introduced in Section 6.2.3. An introduction and detailed study of the single muon trigger algorithm can be found in Section 6. The actually used muon triggers are listed in Table 5.2.

5.3.2. Muon Kinematic Properties

The reconstruction of a $Z \to \mu^+\mu^-$ candidate requires the presence of two oppositely charged muons. One of them has to be associated with the trigger decision that led to the selection of the event.

The transverse momenta of both muons have to exceed 20 GeV/c; this threshold is driven by the demand to have a constant selection threshold and a distinct separation from the lowest unprescaled muon trigger threshold which has been raised several times. Furthermore, both muons must be measured within the central barrel region or the transition region towards the endcaps, i.e. $|\eta_\mu| < 2.1$. This selection excludes the forward region where muons can be measured only with detectors in the endcaps of the CMS apparatus. Studies showed that the trigger decision was not reliable in this region for the configuration of the Level 1 trigger algorithm that was in place in 2010 [64].

Table 5.2.: Single muon triggers used in the $Z \to \mu^+\mu^-$ analysis on the 2010 data sample. $\mathcal{L}$ refers to the integrated luminosity of the specific run range. The thresholds of the trigger steps are given in GeV/c.

Trigger	Thresholds			Run Range	$\mathcal{L}$ [pb^{-1}]
	L1	L2	L3		
HLT_Mu9	7	7	9	133446 – 147116	8.2
HLT_Mu15	7	7	15	147146 – 149442	27.7

5.3.3. Muon Reconstruction Quality Criteria

The selection of reconstructed muons for the analysis is driven by the demand for a clean sample of muons with a negligible fraction of misidentified muons and for a precise measurement of the muon momentum. As this task is common to many analyses, a number of quality criteria [108, 109] have been agreed upon within the CMS collaboration. These quality criteria are outlined in the following and form the baseline selection for all reconstructed muons which are used in this thesis.

Muons can originate from so-called decays in flight of hadrons, i. e. the muon is created within a hadronic jet. As a consequence, these muons are in general accompanied by additional tracks and energy deposits, they are also likely to have no hits in the inner tracking detector. These muons can be suppressed sufficiently by dismissing all muons which are not reconstructed as tracker muons and global muons at the same time. The definition of both kinds of muons is explained in Section 5.5.3. In the case of a matching track in the muon system for an arbitrary track in the tracking system, which originates from a charged particle in the original hadronic jet, the quality of the resulting muon track reconstruction is usually poor. The quality is measured in terms of a χ^2 value for the fit of the track. A threshold

for the normalised χ^2 value of the reconstructed muon track

$$\chi^2/\text{n.d.o.f.} < 10$$

and the necessity to use information from both the tracking and the muon detector systems in the fit reduces the number of muons originating from jets considerably.

A source of fake muons are high energetic jets that traverse the hadronic calorimeter and the solenoid and finally enter the first station of the muon detectors. The iron return yoke reliably prevents a deeper penetration of the muon system. Consequently the presence of a signal in two different layers of the muon detector, one of them in the most outer one, can reduce the number of misidentified muons originating from punch-through jets reliably. At the same time this requirement indirectly improves the momentum measurement during the decision-making process of the trigger.

The measurement of the muon momentum is done solely with the inner tracking detector for muons with a transverse momentum below 200 GeV/c. To ensure a precise measurement it is thus advisable to impose additional requirements on the reconstruction of the muon track within the tracking system. A total number of at least 10 interaction points in both pixel and strip detector, i. e.

$$n_{\text{pixel}} + n_{\text{strip}} > 10 \quad \text{with} \quad n_{\text{pixel}} > 0 \text{ and } n_{\text{strip}} > 0 \ ,$$

ensures a precise reconstruction of the muon momentum.

Although the previous quality cuts and the beam spot constraint during the muon reconstruction reject most cosmic muons, a selection based on the distance of the closest approach to the reconstructed beam spot is exploited. All muons with an impact parameter larger than 2 mm with respect to the luminous area of the beam are rejected as potential cosmic muons. Dedicated studies have shown that the impurity due to cosmic muons is negligible after all mentioned cuts [110, 111].

5.3.4. Muon Isolation

As the decay of a Z boson into two muons does not include any colour charge, the decay itself does not cause any hadronic activity. The amount of deposited energy and additional tracks in a region around the muons is thus limited. As introduced in Section 3.4, the Particle Flow algorithm allows to construct a quantity for the isolation of a muon in a consistent way by summing over all tracks and energy deposits around the muon direction:

$$\text{Iso}\,(\mu) = \frac{1}{p_{\text{T}}^{\mu}} \sum_{\Delta R<0.4} \left(p_{\text{T}}^{\text{charged}} + E_{\text{T}}^{\gamma} + E_{\text{T}}^{\text{neutral}} \right) \ .$$

Measuring the isolation relative to the transverse momentum of the muon allows a larger amount of activity for high transverse momenta, e. g. through bremsstrahlung. Figure 5.2(a) depicts the distribution of the relative combined isolation quantity. The distribution includes the values for both muons after all other

event selection criteria have been applied. Accordingly, the selection based on the isolation quantity is able to suppress events arising from QCD processes reliably.

Figure 5.2(b) illustrates the result of an inversion of the isolation criterion for both muons. The sample is dominated by the QCD sample, nevertheless the Monte Carlo describes the shape of the distribution well. The predicted event yield is underestimated by 11%. However, no event from the simulated QCD sample survives all selection steps. The upper bound for a 95% confidence level yields 0.29 events.

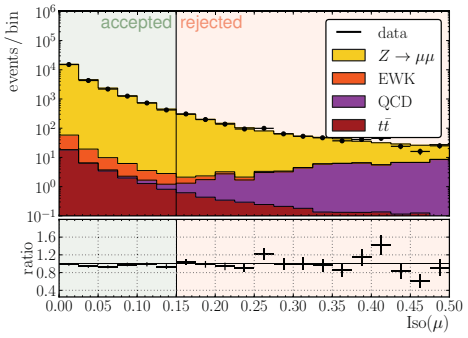

(a) Distribution of the relative combined isolation quantity after all other selection steps. The vertical black line indicates the threshold for the selection based on the isolation quantity.

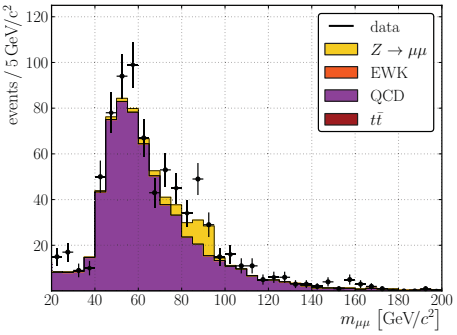

(b) Invariant mass distribution for an inversion of the isolation criterion, i. e. *both* muons are required to be non-isolated.

Figure 5.2.: Study of the muon isolation requirement in di-muon events.

5.3.5. Summary

Table 5.3 presents the number of expected events for the signal and background processes after each step of the selection procedure. All samples are scaled to the integrated luminosity recorded in 2010 to allow a reasonable comparison.

Events from electroweak processes are mainly suppressed through the requirement for two oppositely charged muons with a distinct transverse momentum. The situation is similar for the QCD sample. However, the isolation criterion for the two muons reduces the number of events surviving all cuts to a negligible level. The top pair sample with two leptons in the final state has a small production cross section, however it accounts for one third of the final background contribution.

In total, the simulation predicts 11648 signal and 40 background events for an integrated luminosity of $35.6\,\mathrm{pb}^{-1}$.

5.4. Results for the 2010 Data Sample

The data sample which has been accumulated during the 2010 data taking era contains 11386 events fulfilling all previously described selection criteria. A study

Table 5.3.: Number of expected events for the signal and background contributions after each step of the selection process. The numbers are given for an integrated luminosity of $35.6\,\mathrm{pb}^{-1}$. The last row further includes the statistical uncertainty arising from the limited size of the Monte Carlo samples. The contributions from background processes amount 0.3% of the expected yield for events with a $\mathrm{Z} \to \mu^+\mu^-$ candidate. Since no events from the QCD sample survive all selection steps, the given number corresponds to the upper bound at a 95% confidence level.

Requirement	$\mathrm{Z} \to \mu^+\mu^-$	EWK	$t\bar{t}$	QCD
all events	60 361	432 049	562	3 003 126
High Level Trigger	40 498	234 615	327	2 544 614
opposite charge	28 188	15 887	143	424 080
$p_{\mathrm{T}}^{\mu_1} > 20\,\mathrm{GeV}/c$	17 061	160	53	4 389
$p_{\mathrm{T}}^{\mu_2} > 20\,\mathrm{GeV}/c$	17 061	160	53	4 389
$\lvert\eta_{\mu_1}\rvert < 2.1$	15 631	143	51	3 788
$\lvert\eta_{\mu_2}\rvert < 2.1$	14 359	131	49	3 491
quality: first muon	13 913	93	46	2 336
quality: second muon	13 476	67	44	1 081
associated trigger decision	13 476	67	44	1 078
isolation: first muon	12 403	51	33	3.7
isolation: second muon	12 129	48	29	0.4
invariant mass	$11\,648 \pm 19$	27 ± 0.9	13 ± 0.1	< 0.29

with simulated samples predicts an event yield of 11688 events. This number includes 40 expected events arising from background processes, equivalent to a ratio of $(0.3 \pm 0.1)\%$.

The CMS detector was able to measure the momenta of muons precisely from the beginning of the data taking campaign as outlined in Section 3.4.1.

Figure 5.3 shows an event with two muons fulfilling all selection criteria for a $\mathrm{Z} \to \mu^+\mu^-$ candidate. This example event shows very low hadronic activity and only limited contributions from pile-up events.

Figure 5.4 shows an example set of kinematical quantities of the reconstructed Z bosons. Although the overall agreement of the various distributions for data and Monte Carlo samples is very good, small deviations can be observed for Z bosons with small transverse momenta. These differences indicate that contributions from non-pertubative effects such as the underlying event are not yet well-understood.

The di-muon invariant mass distribution in data shows a minimal shift to the left in comparison to the equivalent distribution in the simulated samples. This shift is manifest and cannot be attributed to statistical fluctuations. However, it is of negligible relevance for this analysis.

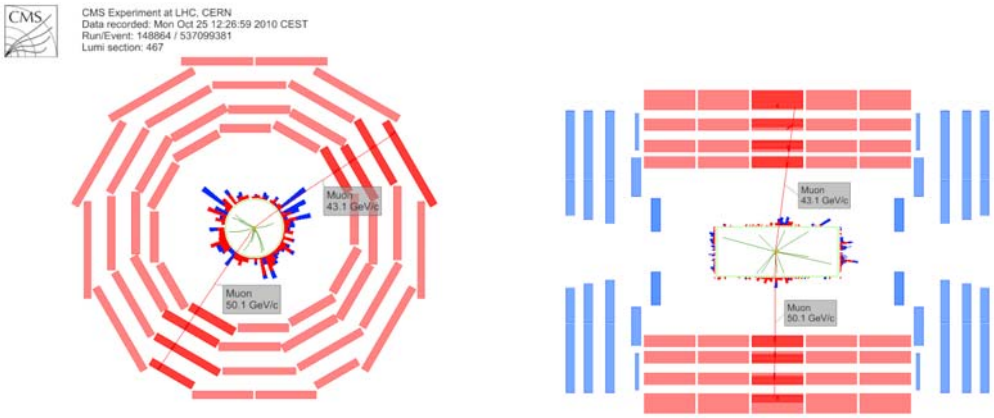

(a) Projection to the r-ϕ plane (b) Projection to the r-z plane

Figure 5.3.: Illustration of a di-muon event recorded on 25 October 2010 (run 148864, ls 467, event 537099381): both muons are situated in the barrel region and fulfil all selection criteria for a Z $\rightarrow \mu^+\mu^-$ candidate. The reconstructed invariant mass of the muon pair is 92.86 GeV/c^2, the di-muon transverse momentum yields 13.94 GeV/c. The energy deposits in the ECAL and the HCAL are indicated by blue and red calorimeter towers. In this event, each calorimeter tower represents less than 3 GeV.

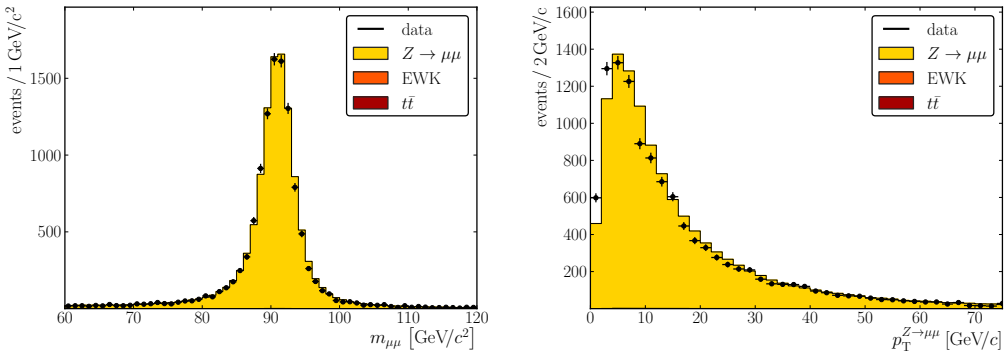

Figure 5.4.: Distributions of the invariant mass (left) and transverse momentum (right) of reconstructed Z $\rightarrow \mu^+\mu^-$ candidates after all selection steps. The background contributions are not visible in this representation. They can be seen in Figure 5.5 which shows the invariant mass distribution in logarithmic scale. Additional kinematical distributions can be found in Appendix A.2.

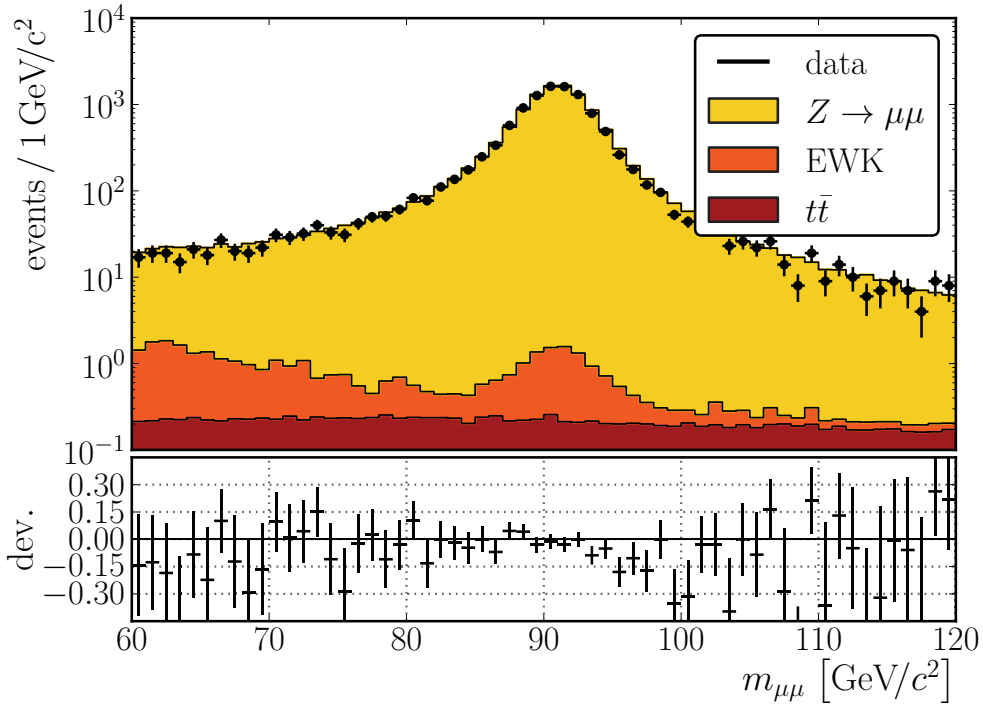

Figure 5.5.: Invariant mass of Z $\to \mu^+\mu^-$ candidates after all selection steps. The peak around the nominal Z mass in the electroweak background contribution (orange) stems from real Z bosons in pair production of electroweak gauge bosons which is considered as background contribution in this analysis.

5.5. Systematic Uncertainties and Correction Factors

A measurement of the Z $\to \mu^+\mu^-$ production cross section is sensitive to any unexpected inefficiency of the muon reconstruction and identification algorithms in data if the modelling in simulation is not correct. As a consequence, it is necessary to show the conformity of the efficiencies derived from simulated samples with results from data-driven methods. Every difference has to be taken into account via correction factors and the uncertainties on the correction factors have to be propagated as uncertainties on the final cross section.

Since muons are of great importance for many analyses within the CMS collaboration, detailed studies have been carried out to address these issues. The comprehensive studies within the Muon Working Group have cumulated in [64]. The results for the muon identification and reconstruction are outlined in Section 5.5.3 and Section 5.5.4 with regard to the Z $\to \mu^+\mu^-$ reconstruction.

5.5.1. Trigger Efficiency

The selection of events by the High Level Trigger (HLT) during the data taking process is the first and most critical part of the selection. It imposes direct and unrecoverable cuts on the phase space of the studied events. A precise understanding of possible differences between the real event selection process and the simulation is thus vital. Section 6 introduces the single muon trigger algorithm, that is used throughout this analysis, in detail. Furthermore, a data-driven estimation of the HLT efficiency is presented there.

The discrepancies in data samples and Monte Carlo samples are accounted for by a correction factor. For the $\mathrm{Z} \to \mu^+\mu^-$ selection, it is sufficient that one of the two muons passes the trigger selection. Accordingly, the probability of an event to pass the trigger step for a given single muon trigger efficiency $\varepsilon^{\mu}_{\mathrm{trigger}}$ reads

$$P^{\mu\mu}_{\mathrm{pass}} = 1 - \left(1 - \varepsilon^{\mu}_{\mathrm{trigger}}\right)^2 = \varepsilon^{\mu\mu}_{\mathrm{trigger}} \,.$$

This probability enters the $\mathrm{Z} \to \mu^+\mu^-$ selection efficiency as one factor. Consequently, the required correction factor results from the fraction of the trigger efficiency $\varepsilon^{\mu\mu}_{\mathrm{trigger}}$ in the data sample and in the simulated sample:

$$k^{\mathrm{trigger}}_{\mathrm{corr.}} = \frac{\varepsilon^{\mu\mu,\,\mathrm{data}}_{\mathrm{trigger}}}{\varepsilon^{\mu\mu,\,\mathrm{MC}}_{\mathrm{trigger}}} \,.$$

Since the data sample spans several periods with different trigger configurations, the individual correction factors are combined. This is done through a weighted sum, with the integrated luminosity as weight. This approach is equivalent to a separate treatment of all intervals with a subsequent combination due to the linearity of the problem. The overall correction factor yields

$$k^{\mathrm{trigger}}_{\mathrm{corr.}} = 0.996 \pm 0.001\,(\mathrm{stat.}) \pm 0.001\,(\mathrm{syst.})$$

where both uncertainties are summed up in quadrature for a later combination of all uncertainties on the final event yield.

5.5.2. Pre-Firing of the Muon Trigger

The association of trigger decisions to time slices during the data taking process is crucial. In a few per mill of the cases, the drift tube subsystem releases a trigger decision too early. The tracker information cannot be read out at this stage and a reconstruction of the event is impossible. The effect has been studied by reconstructing Z candidates out of Level 1 and Level 2 trigger objects in a time slice before the actual bunch crossing only. This approach suffers from the bad momentum resolution of the trigger objects. The uncertainty on the Z event yield due to the premature release of the single muon trigger is estimated as 0.5% [112].

5.5.3. Muon Reconstruction and Selection

The reconstruction of muon candidates is in the first step equivalent to the track reconstruction for arbitrary charged particles. The measurement of the track reconstruction efficiency is described in [113]. The analysis reports a very good agreement with the predictions of the detector simulation over the whole tracker detector acceptance range. A correction for an imperfect description of the track reconstruction is thus not necessary.

The reconstruction of muons further includes the matching of tracks in the tracking detector to tracks in the muon detector and the identification of muons, i. e. the suppression of fake muons. Both steps can be studied with the tag and probe method as used for the trigger efficiency study described in Section 6.4. However, it is necessary to apply a correction for combinatorial contributions from muons and randomly selected tracks. A description of this issue and its solution can be found in [114]. These studies utilise both the Z and the J/Ψ resonances to cover muons with a transverse momentum from a few GeV/c up to 100 GeV/c.

The reported systematic uncertainties are smaller than the statistical uncertainties. A correction factor for this analysis can be calculated as the ratio of the efficiency for the data sample and the Monte Carlo sample. The largest deviation ($\approx 1\%$) from the overall factor over the studied range of the pseudorapidity is taken as conservative estimation of the systematic uncertainty. It is noteworthy that the correction factor is constant if measured as a function of the transverse momentum.

5.5.4. Muon Momentum Scale

The momentum measurement for muons is dominated by the accuracy of the inner tracking detector. Dedicated studies of the momentum scale [109] report a scale uncertainty of up to 1% for the range of the transverse momentum that is important for a $Z \to \mu^+\mu^-$ analysis. The impact on the final event yield is estimated conservatively by scaling the momenta of all reconstructed muons up and down by 1%. The variation of the final event yield is 0.5% and enters as systematic uncertainty.

Dedicated studies exploiting the Z resonance itself [109] also revealed a small dependency of the momentum reconstruction on the sign of the muon charge and the azimuthal angle. However, the uncertainty of the muon momentum covers the observed variations. The result is not taken into account to avoid circular dependencies.

5.5.5. Muon Isolation

The efficiency of the cut on the muon isolation has been studied in various analyses. While one study [112] reports a very good agreement between data and simulation, another one [64] obtains differences up to 1.5%. For a very conservative estimation the muon isolation quantity is varied upwards and downwards by 3% for all reconstructed muons. The propagation to the final final event yields variations of 0.5%. This value is taken as systematic uncertainty.

5.5.6. Limited Size of the Simulated Sample

The limited size of the Monte Carlo samples gives rise to an additional systematic uncertainty of less than 0.2% as listed in Table 5.3. Since the number of simulated events could be increased if necessary, this uncertainty is attributed to the experimental uncertainties.

5.5.7. Underlying Event Tune

The selection of the parameter set for the underlying event has an indirect impact on the results for the $Z \to \mu^+\mu^-$ search via the isolation criterion for the two muons. Unfortunately, underlying event tunes are closely connected to the type of shower algorithm. The use of POWHEG requires a p_T or angular ordered shower. As the official production campaign features only the Z2 tune for the signal process sample, PYTHIA samples are used as replacement.

PYTHIA samples for the signal process are available with a number of different tunes. For this comparison, a sample created with the Z2 tune is used as representative for a p_T-ordered shower algorithm and a sample with the D6T tune as an example for virtuality-ordered showers.

Table 5.4 presents the results for the selection efficiency. The difference amounts to 1% and is taken as systematic uncertainty for the underlying event tune.

Table 5.4.: Effect of the underlying event tune on the final event yield for the signal process. The samples in this test have been generated with PYTHIA and are part of the official production campaign.

	Z2 tune	D6T tune
before all cuts	2 235 697	2 558 038
after all cuts	434 882	492 560
efficiency	0.1945	0.1926

5.5.8. Cross Section

The calculation of the inclusive cross section is done with FEWZ [115, 116] and DYNNLO [117, 118] at NNLO precision in α_s. The computations include the γ-Z interference as well as spin correlations. Both libraries allow a restriction of the phase space for the Z decay products which simplifies the use in analyses. Using the MSTW [15] set of parton distributions function (PDF), it is possible to perform these calculations from leading order up to NNLO in α_s.

The Z production cross section is calculated for a mass range from 60 GeV/c^2 to 120 GeV/c^2 and a pseudorapidity range from -10 to 10. The latter requirement is loose enough for all possible muon detectors but avoids the very-forward region

for the Z boson where the precision of theoretical calculations is usually limited. This idealised acceptance can be the base for a later comparison with results from different experiments. The window for the invariant mass reduces the contribution from the exchange of virtual photons.

The numerical results of both employed libraries are listed in Table 5.5 and the differences are small. The true value for the cross section is not known and it is not possible to decide a-priori which one of the two implementations is more accurate. Consequently, the mean of the two values is taken as theoretical prediction for the cross section hereafter. The uncertainty on this value corresponds to half of the difference between both values:

$$\sigma^{\mathrm{Z}\to\mu^+\mu^-,\,\mathrm{NNLO}}_{60<m_{\mu\mu}<120\ \mathrm{GeV}/c^2} = (990 \pm 12)\ \mathrm{pb}\ .$$

Scale Dependence

The scale dependence of the result for the $\mathrm{Z} \to \mu^+\mu^-$ production cross section is studied with an upward and downward variation of the renormalisation scale (μ_r) and the factorisation scale (μ_f) by a factor of two. The results are listed in Table 5.5. The maximum deviation of 1.3% from the result for the nominal values of μ_r and μ_f is taken as systematic uncertainty.

α_s Dependence

The calculation of the cross sections is based on a fit of the parton distribution function to the results from various experiments. The actual PDF is of course a function of the strong coupling α_s that has to be determined as well. Both quantities are correlated and it is advisable to study the uncertainty on the cross section arising from both inputs at the same time. The MSTW group provides parton distribution functions for fixed values $\alpha_\mathrm{s} \pm \sigma_{\alpha_\mathrm{s}}$, with the 68% confidence level $\sigma_{\alpha_\mathrm{s}}$ [119]. The sets are used to calculate the $\mathrm{Z} \to \mu^+\mu^-$ production cross section and the envelope of the results is taken as band of the systematic uncertainty around the result for the best fit value. Due to technical limitations this task could not be performed with FEWZ. The uncertainty resulting from DYNNLO yields 1%.

5.5.9. Kinematical Acceptance

The chosen kinematical acceptance for the two muons is driven by the geometry of the CMS detector and its muon reconstruction capabilities. Table 5.5 lists the cross sections for this smaller part of the $\mathrm{Z} \to \mu^+\mu^-$ phase space. With these values it is possible to calculate the kinematical acceptance at NNLO precision. The results are listed in Table 5.6. The largest difference between the predictions by the two libraries and the value that can be determined on the simulated sample (0.411, see Table 5.7) is taken as systematic uncertainty. The uncertainty on the kinematical acceptance thus yields 3.1%. It is noteworthy that the uncertainty is smaller if the

Table 5.5.: Overview of the $Z \to \mu^+\mu^-$ production cross sections with FEWZ and DYNNLO for calculations at different orders of α_s. The calculations use the MSTW set of parton distribution functions. The renormalisation and factorisation scale is varied by a factor of 2 to determine the scale dependency. The value for α_s is varied according to its uncertainty, including correlated effects on the result for the parton distribution functions, as provided by the MSTW group. The results for the nominal settings are shown multiple times for illustrative reasons. Uncertainties below 1 are given as 1.

Order in α_s	μ_r, μ_f	α_s	FEWZ		DYNNLO	
			muon acc.	ideal acc.	muon acc.	ideal acc.
LO	m_W	best fit	303 ± 3	778 ± 4	295 ± 1	753 ± 1
NLO	m_W	best fit	397 ± 3	985 ± 5	384 ± 1	944 ± 1
NNLO	m_W	best fit	395 ± 5	1002 ± 4	392 ± 1	978 ± 1
NNLO	$\frac{1}{2}m_W$	best fit	406 ± 6	1004 ± 4	388 ± 1	965 ± 1
NNLO	m_W	best fit	395 ± 5	1002 ± 4	392 ± 1	978 ± 1
NNLO	$2m_W$	best fit	404 ± 5	1010 ± 4	396 ± 1	988 ± 1
NNLO	m_W	-1σ	-	-	388 ± 1	968 ± 1
NNLO	m_W	best fit	-	-	392 ± 1	978 ± 1
NNLO	m_W	$+1\sigma$	-	-	397 ± 1	988 ± 1

difference is calculated with respect to the NLO result, i. e. in the same order of α_s as the generated sample.

5.6. Cross Section Measurement

The cross section for the Z boson decay into two muons can be calculated with the formula

$$\sigma_{Z\to\mu^+\mu^-} = \frac{N_{\text{meas}} - N_{\text{exp}}^{\text{bkg}}}{\epsilon_{\text{acc}}^{Z\to\mu^+\mu^-} \cdot \epsilon_{\text{sel}}^{Z\to\mu^+\mu^-} \cdot \mathcal{L}} \tag{5.1}$$

where N_{meas} denotes the number of observed events after all selection steps. $N_{\text{exp}}^{\text{bkg}}$ is equivalent to the number of expected events from background processes. The muon kinematic acceptance efficiency with respect to the considered mass window, $\epsilon_{\text{sel}}^{Z\to\mu^+\mu^-}$, subsumes all efficiencies concerning the reconstruction, identification and selection of muon pairs. Table 5.7 summarizes the numerical values for the POWHEG signal sample.

With an integrated luminosity for the processed data sample of

$$\mathcal{L} = (35.6 \pm 1.4)\ \text{pb}^{-1},$$

Table 5.6.: Acceptance as calculated with different parton level Monte Carlo programs at various orders with MSTW parton distribution functions. The renormalisation and factorisation scale is varied as well as the used values from the PDF fit. The values with the nominal settings are shown multiple times for illustrative reasons.

Order in α_s	μ_r, μ_f	α_s	FEWZ	DYNNLO
LO	m_W	best fit	0.3900	0.3916
NLO	m_W	best fit	0.4036	0.4068
NNLO	m_W	best fit	0.3949	0.4010
NNLO	$\frac{1}{2}m_W$	best fit	0.4051	0.4023
NNLO	m_W	best fit	0.3949	0.4010
NNLO	$2m_W$	best fit	0.4000	0.4009
NNLO	m_W	-1σ	-	0.4005
NNLO	m_W	best fit	-	0.4010
NNLO	m_W	$+1\sigma$	-	0.4016

the Z production cross section yields

$$\sigma^{\text{exp.}}_{\text{Z}\to\mu^+\mu^-} = 983.0 \pm 9.2\,(\text{stat.}) \pm 40.1\,(\text{exp.}) \pm 35.8\,(\text{theo.})\ \text{pb}\ . \tag{5.2}$$

The individual uncertainties are divided based on their origin and added up in quadrature. The individual uncertainties are listed in summary in Table 5.8. The experimental result agrees well with the theoretical prediction, the difference of 0.7% is covered by the conservatively estimated uncertainties.

The result is also in good agreement with the official result of the CMS collaboration [112]:

$$\sigma_Z^{\text{CMS}} \times \text{BR}\left(\text{Z}\to\mu^+\mu^-\right) = 968 \pm 8\,(\text{stat.}) \pm 39\,(\text{exp.}) \pm 18\,(\text{theo.})\ \text{pb}\ .$$

The small differences between the result of this work and the official CMS result can be explained by small differences in the event selection and in the study of uncertainties: While in this work the muon isolation requirement is based on the Particle Flow algorithm, the muon isolation is only based on tracks in the official CMS analysis. For this thesis, it was further possible to use a second program for cross-checks of the Z boson production cross section and the kinematical acceptance at NNLO precision in α_s, DYNNLO, which results in additional uncertainties. Figure 5.6 presents the Z boson production cross section for different hadron collider experiments.

5.6.1. Luminosity Measurement with Z bosons

The reconstruction of $\text{Z}\to\mu^+\mu^-$ candidates also gives a handle on the integrated luminosity if Eq. (5.1) is solved for $\mathcal{L}$. This approach can be useful for analyses

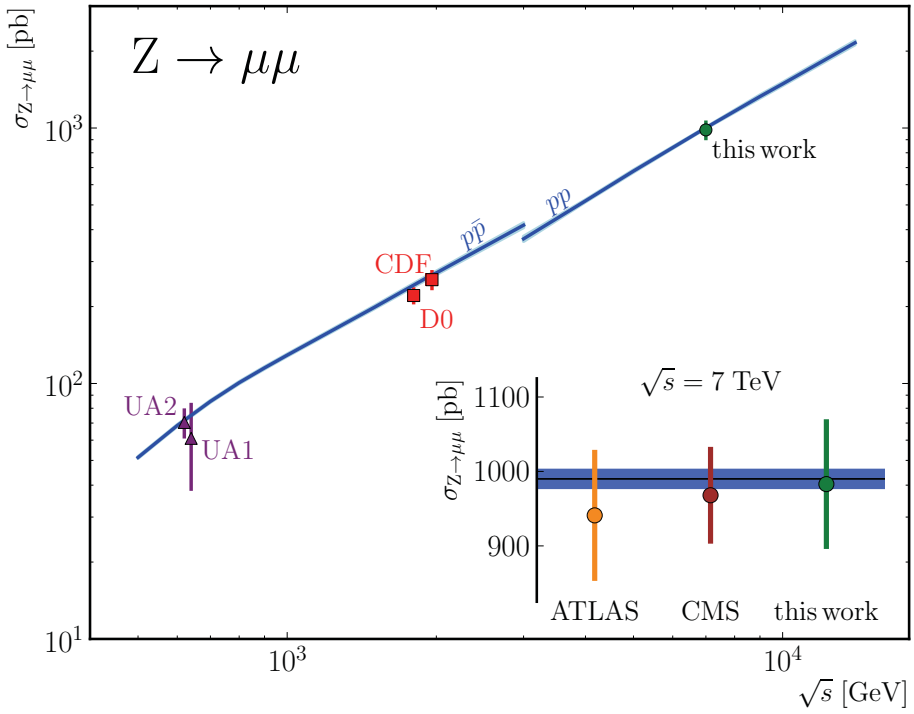

Figure 5.6.: Z boson production cross section at hadron colliders with different centre-of-mass energies [103, 120, 121, 122, 123]: The representation in the lower right corner depicts the result of this work and the official results of the ATLAS and the CMS collaborations at $\sqrt{s} = 7$ TeV. The blue lines have been calculated with FEWZ and the MSTW parton distribution function at NNLO precision in α_s. The error bars indicate the sum of all individual uncertainties.

where the uncertainty on the integrated luminosity is a large contribution to the systematic uncertainty of the final result. However, it is mandatory to reduce the systematic uncertainties coming from theory to actually achieve a higher precision. With the conservative estimation for the theoretical uncertainties of 3.3%, the gained precision would be small at the moment but a more detailed understanding of the theory parameters, e. g. α_s, would pave the way to achieve this goal.

5.7. Additional Studies

5.7.1. Pile-Up

Already in the first year of operation, the increase of the beam intensity and the optimized beam configuration with bunch trains induced the appearance of pile-up events. As explained in Section 3.2.3, pile-up events add additional tracks and energy deposits to an event. While the reconstruction quality of tracks is unaffected

Table 5.7.: Efficiencies for the used sample of simulated $Z \to \mu^+\mu^-$ events. The difference for the value of the kinematic acceptance between the simulated sample and the average value acquired with the direct NNLO calculations is taken as systematic uncertainty.

Step	Events	Rel. Eff.	Abs. Eff.
All events	1998931	-	-
Mass window ($60 < m_{\mu\mu} < 120$ GeV/c^2)	1143944	0.572	0.572
Muon kinematic acceptance	469957	0.411	0.235
After all selection steps	384370	0.818	0.192

in the vicinity of pile-up events due to the robustness of the used algorithms, all other quantities that are sensitive to the presence of additional energy deposits or tracks need special attention. The muon isolation is the most affected quantity for the $Z \to \mu^+\mu^-$ analysis. Figure 5.7 shows a comparison for the two available sets of simulated events. It is clearly visible that the isolation quantity is better described by samples that include the correct amount of additional events.

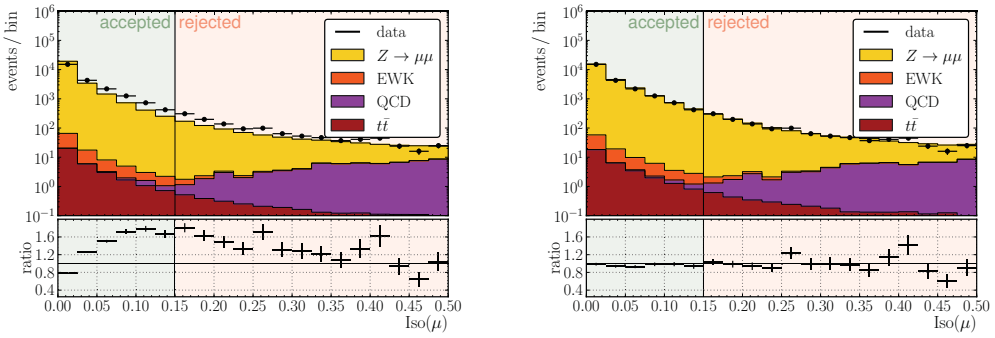

(a) Simulated sample without any pile-up events

(b) Simulated sample with additional pile-up events similar to the 2010 data sample

Figure 5.7.: Distributions of the muon isolation quantity for two sets of simulated samples. The vertical line indicates the selection criteria for $Z \to \mu^+\mu^-$ candidates. The black points correspond to the data sample and are identical in both plots.

5.7.2. Time Evolution

Unlike for simulated data samples, results of a real experiment can exhibit a time dependence due the unintentionally changing experimental conditions. Concerning this analysis, updates of trigger and reconstruction algorithms can have an impact on the event rate or properties of the reconstructed physical objects. Furthermore, any degradation of detector components can influence the final results although they might not be noticed at the time of the data taking process.

Table 5.8.: Overview of the uncertainties on the $Z \to \mu^+\mu^-$ production cross section. The first group is quoted in the text as experimental uncertainty, the second group of uncertainties as theoretical uncertainties.

Source of Uncertainty	Uncertainty [%]
Luminosity	4.0
Muon momentum scale	0.5
Muon trigger efficiency	0.2
Muon trigger prefiring	0.5
Muon isolation	0.3
Sample Size	0.2
Experimental uncertainties (total)	4.1
Scale dependency	1.3
Strong coupling, PDF	1.0
Acceptance	3.1
Underlying event	1.0
Theoretical uncertainties (total)	3.6

Figure 5.8 depicts the event yield for events with $Z \to \mu^+\mu^-$ candidates as a function of the integrated luminosity. For the left plot, the data sample is divided into mutually exclusive subsamples, preserving time order. The right plot shows the fractional event yield for data sample and the Monte Carlo prediction, in this case a constant event rate is expected. A Kolmogorov–Smirnov test yields a measure for the compatibility of both distributions [124]. The level of significance for this study is chosen as $\alpha = 0.1$ and is illustrated as light red band. Both distributions indicate that the event rate is constant over time, any observed fluctuation is compatible with expected statistical fluctuations.

5.7.3. Outlook for an analysis with 2011 data

In 2011, the threshold for the lowest unprescaled trigger algorithm is being raised quickly to cope with the heavy increase of the beam intensity. To operate with a fully efficient trigger it is necessary to increase the threshold for the muon transverse momentum at some points. The implications of this solution are illustrated in Figure 5.9. The event yield for $Z \to \mu^+\mu^-$ events is shown there as a function of the threshold of the muon transverse momentum. The two vertical lines indicate the thresholds for 2010 and 2011. The proposed cut for 2011 assumes a single muon trigger threshold at 24 GeV/c. The illustration shows that the $Z \to \mu^+\mu^-$ event rate will be lowered by about 20% due to the tighter selection criterion. It is important to note that the shown data points are highly correlated.

An alternative approach for higher values of the instantaneous luminosity in 2011

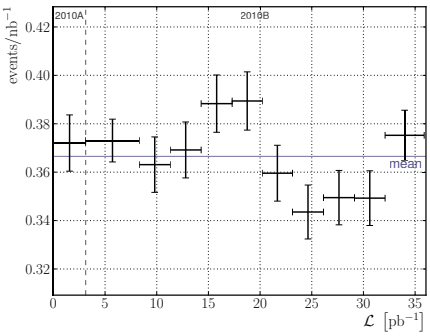

(a) Z event yield per integrated luminosity in mutually exclusive, time ordered intervals of the collected data sample. The error bars indicate the statistical uncertainties. Unlike for the right plot, the data points are uncorrelated.

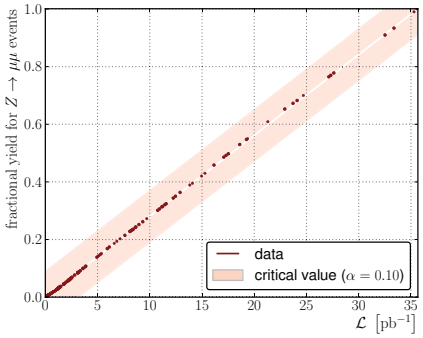

(b) Fractional event yield as a function of the integrated luminosity. The light red band indicates the critical values for a Kolmogorov-Smirnov test with $\alpha = 0.1$ as significance level. The underlying hypothesis is a uniform distribution of the events over the data sample, i. e. a diagonal line. The effect of the different trigger efficiencies in the two data taking periods is hardly visible as the second periods includes the majority of the collected data.

Figure 5.8.: Z event yield as function of the accumulated amount of data, i. e. as a function of time: both representations suggest that there is no indication for a time dependency of the event yield in 2010, beside the aforementioned trigger efficiency.

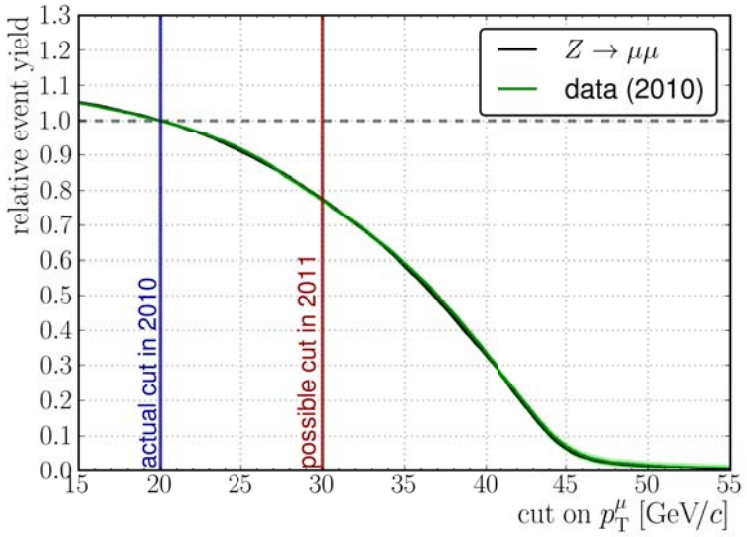

Figure 5.9.: Z event yield as a function of the threshold for the muon transverse momentum during the selection process. Both distributions are normalised to their actual values for the threshold used in 2010. The light green band indicates the statistical uncertainty on the data sample. It is noteworthy that all data points are correlated due to the cumulative presentation.

incorporates a double muon trigger algorithm, i. e. a trigger algorithm that requires the presence of two muons. The threshold for the muon transverse momentum during the trigger decision process can be chosen much lower ($p_{\mathrm{T}}^{\mathrm{HLT}} < 10$ GeV/c) and it is then not necessary to increase the cut on the transverse momentum of the muons. However in this case, the determination of the trigger efficiency is much more complicated as the tag and probe method cannot be employed. It is further not possible to measure the trigger efficiency for a single muon on an unbiased sample as a function of a single muon kinematic variable (p_{T} or η).

6. Muon Trigger

The muon trigger algorithms are of great importance in many analyses, among them the inclusive Z cross section measurement. Any inefficiency or problem has a direct impact on the selection of events during the data taking process and thus also on the final analyses.

The physical analyses define the requirements for the muon trigger algorithm. The efficiency of the muon identification has to be high while the contamination from other objects should remain small. Although the algorithm for the trigger should follow the subsequent offline reconstruction, the selection itself should be loose and transparent. This allows all working groups to impose individual quality cuts that might be necessary to cope with new physical phenomena or technical problems that could not be foreseen.

The trigger decision is based on the result of multiple steps. The first step, called Level 1 trigger, is implemented within the detector hardware and reduces the rate of events from several millions to some thousand events per second. Subsequently the event candidates are processed by a software-implemented algorithm, the High Level Trigger (HLT). At each step of the trigger it is possible to apply a selection based on the number of candidates or the kinematic properties of the trigger objects at this step, i. e. the transverse momentum and the pseudorapidity (see also Table 6.1). It is also possible to refuse a pre-defined fraction of events to lower the event rate, this approach is called prescaling.

A comprehensive introduction to the muon trigger along with results from the commissioning of the trigger algorithms with cosmic muons can be found in [56], [46] and [125].

6.1. Level 1 Trigger

The Level 1 algorithm is implemented within customised hardware to cope with the high processing rate. Four muon subsystems operate independently: the RPC system is divided into a barrel and an endcap region, the DT system covers the barrel region while the CSC is installed in the forward region. Each subsystem provides up to four muon trigger candidates, so-called primitives, ordered by a combination of their transverse momenta and their qualities. The decision is made based on local information, only in the overlap region ($|\eta| = 0.9 - 1.2$) the CSC and the DT systems exchange information on track segments. The global muon trigger (GMT) collects all information and combines primitives if possible.

The CSC trigger cannot provide an estimation of the transverse momentum for $|\eta| > 2.1$. As a consequence all trigger primitives in this region are discarded by

the global muon trigger. Although there were some attempts in 2010 to extend the muon trigger range up to $|\eta| = 2.4$, the forward region has been excluded from all muon-based analyses and will not be covered by the following trigger efficiency measurements.

6.2. High Level Trigger

The High Level Trigger is implemented in software. This allows for a high flexibility and quick development. Internally, the trigger is divided into Level 2 and Level 3. By convention the Level 2 algorithms operate on calorimeter and muon system information while the Level 3 algorithm may also perform track reconstruction which is more time consuming. This distinction is especially important for triggers with isolation.

6.2.1. Level 2

The muon candidates of the Level 1 step act as seeds for a track reconstruction in the muon system. At this stage hit information from all sub-detectors of the muon detector system are combined. The applied algorithm reconstructs a track beginning at the innermost layer of the muon system and advancing outwards. The state vector of the track candidate, i. e. a tuple of the position and the momentum, is iteratively propagated based on the Kalman filter technique [126]. Energy loss, multiple scattering in the detector material and the spatially varying magnetic field are taken into account when the state vector is updated.

Upon reaching the outermost chamber the track is fitted again, now inwards with the constraint that the track originated from the luminous area as defined by the position and the size of the beam spot. The final track candidate for the Level 2 step is rejected if the quality of the reconstruction does not reach a predefined level, for which the χ^2 value of the reconstruction fit is used. This requirement suppresses fake and cosmic muons and thus reduces the processing time of the trigger.

The precision of the momentum reconstruction is higher than on Level 1 as it facilitates information from all muon sub-detectors. For illustrative purposes, Figure 6.1 shows the resolution with respect to a reconstructed offline muon fulfilling quality criteria as defined in Section 5.3.3. The applied threshold for the muon transverse momentum of Level 2 candidates is – at least for the 2010 data taking period – identical to the threshold on Level 1.

As the bending of the trajectory is taken into account during the reconstruction process, Level 2 objects can be matched directly using a ΔR criterion, e. g.

$$\Delta R\left(\mu^{\mathrm{L2}}, \mu^{\mathrm{reco}}\right) < 0.3 \,.$$

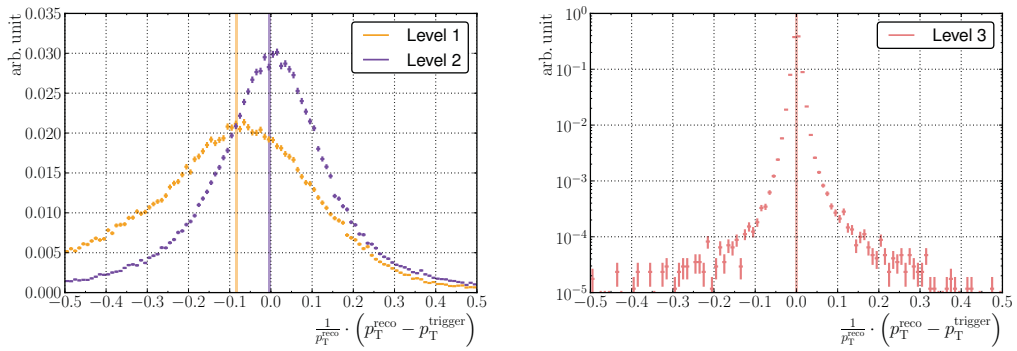

Figure 6.1.: Resolution of the muon transverse momentum for the muon trigger algorithms: the reconstruction using all possible sub-detector on Level 3 (right) yields a better result than the "muon system only" reconstruction (left). The vertical lines indicate the means of the distributions.

6.2.2. Level 3

The Level 3 reconstruction is based on the muon candidate trajectories that have been produced in the preceding Level 2 step. The tracks are extended from the muon system inwards to the silicon tracking detector to yield a globally reconstructed track. As before, energy loss – especially in the interjacent solenoid and the calorimeter – and magnetic field are taken into account. Through this it is possible to get a reliable estimation of the region in the tracker where possible hits, i. e. measured interaction points with the detector material, of a muon candidate can reside. This a priori guess is required to reduce the complexity of the track reconstruction which is a very time consuming task without any localisation. The size of the region of interest depends of course on the uncertainty of the seed and the trajectory propagation.

The seed finding is crucial for the following track reconstruction. With the beginning of the second data taking period in 2010, the muon trigger algorithm has been upgraded and since then employs three different kinds of trajectory seeding algorithms. They are arranged in a cascaded way and called successively if the previous algorithm fails to find seeds. As a consequence this approach ensures a high seeding efficiency without overstraining the time budget. A detailed introduction of this cascaded seed finding can be found in [127].

Finally, all possible tracks in the tracking detector are combined with the hits of the trajectory in the muon system to perform a global fit. A muon candidate passes the Level 3 step and thus the complete HLT if the fit yields a satisfactory quality and if the transverse momentum exceeds a pre-defined threshold. The momentum measurement is at this stage very accurate as the tracking detector allows a precise determination of the muon trajectory. Figure 6.1 illustrates that the momentum resolution at the Level 3 step is of the order of a few percent with respect to a fully

reconstructed muon.

6.2.3. Muon Isolation

With increasing beam intensity, the momentum thresholds of the single muon HLT algorithms have to be increased to match the specified event rate without applying a prescale factor. As many physics analyses study muons that originate from electroweak decays, e. g. $W \to \mu\nu$, it is possible to exploit the absence of additional (hadronic) activity around the muon to keep the momentum thresholds low (see Figure 6.2).

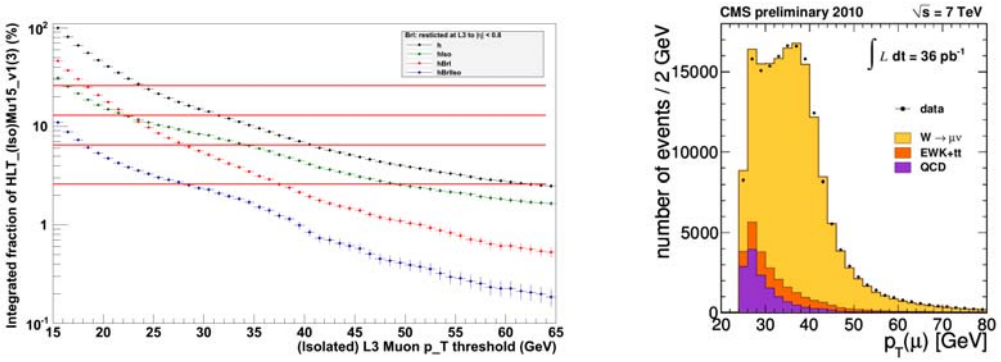

Figure 6.2.: The limited bandwidth of the persistent storage system requires a tightening of the threshold of the muon transverse momentum selection with an increasing beam intensity. The left plot [128] depicts the integrated trigger rate with respect to a (non-)isolated muon trigger with $p_{\mathrm{T}}^{L3} > 15$ as a function of the Level 3 p_{T} threshold. The horizontal red lines indicate the required thresholds for various intensities (5e32, 1e33, 2e33 and 5e33) to cope with predefined event rates. The intersections with the red horizontal lines determine the required thresholds for a non-isolated (black) and an isolated (green) single muon trigger. It is obvious that an isolation criterion can help to preserve the statistical precision in analyses with $W \to \mu\nu$ (right plot: distribution of the muon transverse momentum [129]). The red and blue points in the right plot depict the thresholds for a barrel-only trigger, i. e. a geometrical restriction to the barrel region can further reduce the trigger rates. This approach is currently under discussion for the 2011 data taking period.

As the muon production rate is dominated by decays of kaons, pions and quarks (see Figure 6.3), which lead in general to non-isolated muons, the trigger rate can be reduced by introducing an additional isolation requirement without losing muons from favourable weak boson decays.

The quantity that is used to measure the isolation of a muon is defined as the sum of the transverse momentum or transverse energy of all objects – either tracks or energy deposits – within a cone around the muon direction, i. e.

$$\Delta R\,(\mathrm{obj}, \mu) \leq \Delta R_{\mathrm{max}} \; .$$

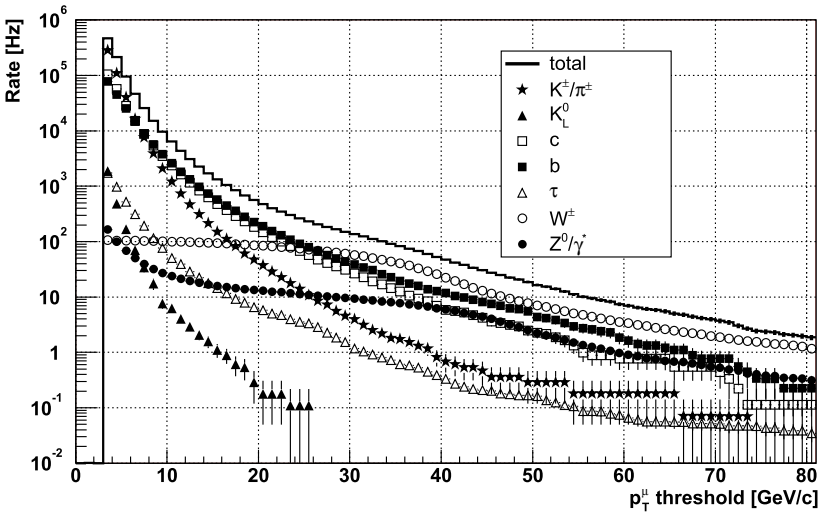

Figure 6.3.: Rate for single muon production as a function of the muon transverse momentum for a luminosity of $10^{34}\,\mathrm{cm}^{-2}\mathrm{s}^{-1}$ [56]. The listed samples have been generated with PYTHIA.

A muon is called *isolated* if the sum is below a certain pre-defined threshold. All thresholds have been determined from reference samples for signal (W and Z bosons) and background (b, c, K, π) contributions beforehand. However, there are ongoing discussions to modify the thresholds based on the experience with real data. The introduction of relative isolation variables,

$$\mathrm{Iso}^{\mathrm{rel.}}\,(\mu) = \frac{1}{p_{\mathrm{T}}^{\mu}} \cdot \mathrm{Iso}\,(\mu)\,,$$

is also under discussion. This definition would exploit the correlation between the momentum of muons from hadronic origin and the momentum of the accompanied hadronic jet without rejecting high energetic muons which usually have larger energy deposits and that would be filtered out by a stricter absolute threshold.

Isolation based on Calorimeter Information

The isolation quantity in the calorimeter system is calculated as the sum of all energy deposits in both calorimetric sub-detectors:

$$\mathrm{Iso}_{\mathrm{calo}}\,(\mu) = \sum_{\Delta R<0.24} \left(\alpha E_{\mathrm{T}}^{\mathrm{ecal}} + E_{\mathrm{T}}^{\mathrm{hcal}}\right) \quad \text{with} \quad \alpha = 1.5\,.$$

Electronic noise in detector cells is excluded from the summation by appropriate thresholds. The weighting coefficient α has been optimised in simulation based studies and is a consequence of the non-compensating character of the calorimeter system. While the cone size $\Delta R = 0.24$ is identical for all muon candidates, the

isolation thresholds are a function of the pseudorapidity and are more stringent in the forward region.

The calculation of the calorimeter isolation as sum over local calorimeter deposits is not very time consuming and can therefore be applied on the Level 2 of isolated muon triggers. It is obvious that the isolation quantity does not include an energy calibration and does not undergo special cleaning procedures that can be applied during the offline reconstruction process.

Isolation based on Pixel Tracks

The pixel-based isolation algorithm evaluates the information on reconstructed tracks from the innermost pixel detector. Tracks are taken into account if they originate from the beam spot region and the isolation quantity then reads

$$\mathrm{Iso}_{\mathrm{pixel}}\left(\mu\right) = \sum_{\Delta R<0.24} p_{\mathrm{T}}^{\mathrm{track}} \quad \text{with} \quad p_{\mathrm{T}}^{\mathrm{track}} > 900\,\mathrm{MeV}\ .$$

The constraint on the track origin removes tracks from pile-up events that have a different production vertex. This holds especially for out-of-time pile-up. The threshold for the isolation quantity is around 1.1 GeV/c with a slight dependency on the pseudorapidity. The pixel track isolation is applied on Level 3 of the muon trigger.

Isolation based on Tracker Tracks

The isolation based on tracks around the muon could also be calculated using information from both pixel and strip detector. Since the time to run even a regional tracking algorithm increases the time to get a trigger decision, the tracker isolation is only applied during analyses on reconstructed muons at the moment. This situation might change with additional computational resources.

6.3. Measurement of Muon Trigger Efficiencies

As outlined before, a precise and credible measurement of the muon trigger efficiency is essential for a great variety of analyses. Although the estimation of the trigger efficiency can be done with simulated events, this approach is not trustworthy as it inevitably suffers from any imperfection in the simulation of the physical processes, the simulation of the detector and the simulation of the trigger algorithms. As a consequence a data-driven estimation of the efficiency is required. In the following, two distinct methods are presented to meet this task.

During the 2010 data taking period, the trigger configuration has been modified several times. The growth of the beam intensity required a successive increase of the thresholds of single muon triggers to comply with the defined data rate for the muon triggers. The following study of the muon trigger efficiencies will only cover periods where the specific triggers were not prescaled. For the inclusive measurement this

restriction is mandatory in order to avoid a bias due to the prescale. For consistency reasons the run ranges are also used for the tag and probe method (see Section 6.4). The studied triggers and their unprescaled run ranges are listed in Table 6.1.

Intermediate objects of the trigger algorithm are not stored as they are not needed in typical physics analyses. However, these objects allow a useful insight into the actual trigger decision. It was therefore necessary to reprocess especially the corresponding simulated samples. The hereby used trigger configuration corresponds to the last configuration of the 2010 data taking campaign.

All uncertainties given in this chapter refer to the 68% binomial proportion confidence level. From the various methods available to estimate this interval, the Clopper-Pearson method [130] has been used. It is based directly on the evaluation of the binomial distribution and it does not suffer from undercoverage, i. e. the confidence interval estimation is conservative.

Table 6.1.: Single muon triggers in 2010 and the corresponding run ranges where the triggers were unprescaled, $\mathcal{L}$ indicates the integrated luminosity of the specified run range. The study of the HLT_Mu9 trigger is split into two parts to reflect the improvements in the global reconstruction on Level 3 after run 146239, between run era 2010A and 2010B. The thresholds of the trigger steps are given in GeV/c.

Trigger	Thresholds			Isolation	Run Range	$\mathcal{L}$ [pb^{-1}]
	L1	L2	L3			
HLT_Mu9	7	7	9	no	133446 – 147116	8.2
HLT_Mu11	7	7	11	no	146315 – 148068	14.5
HLT_Mu13	7	7	13	no	146315 – 148068	14.5
HLT_Mu15	7	7	15	no	147146 – 149442	27.7
HLT_IsoMu9	7	7	9	yes	146315 – 148068	14.5
HLT_IsoMu13	7	7	13	yes	148783 – 149442	18.2

6.4. Tag and Probe Method

The measurement of various kinds of efficiencies with the tag and probe method is an established procedure within high energy physics experiments [114, 131, 132, 133]. The method provides an unbiased estimation and it can be applied on both data and Monte Carlo samples.

The tag and probe method exploits well-known resonances, e. g. the J/ψ or the Z resonance. In the following the Z resonance with a subsequent decay into two muons will be used to measure the efficiency of the single muon triggers.

The $\mathrm{Z} \to \mu^+\mu^-$ candidates for the tag and probe method are in principle selected with asymmetric selection criteria for the two daughter particles. One muon has to pass a very strict selection, including a positive trigger decision that leads to

the actual storing of the event. As it mainly identifies the event it is called *tag*. The selection of the second, oppositely charged *probe* muon is relaxed to allow an unbiased measurement. To estimate the trigger efficiency it is sufficient to test for a trigger decision on this second muon and calculate the fraction that could pass the muon trigger algorithm successfully.

A constraint on the invariant mass of both muons further suppresses events mimicking a $Z \to \mu^+\mu^-$ decay. A correction for background contributions is thus not necessary and a simple counting method with well-defined confidence intervals is possible.

6.4.1. Single Muon Trigger

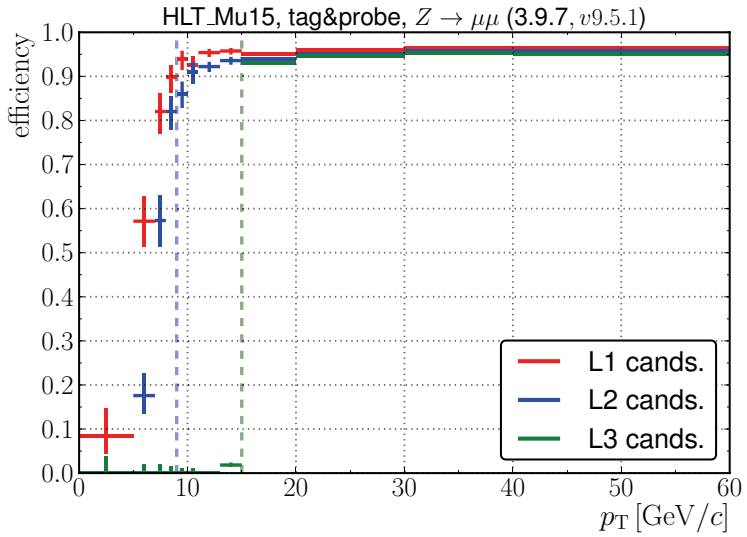

Figure 6.4.: Trigger efficiency as a function of the transverse momentum of the reconstructed muon for the HLT_Mu15 algorithm. The thresholds for the triggers are indicated by dotted lines.

Figure 6.4 shows the the efficiency for the different steps of the HLT_Mu15 trigger algorithm as function of the transverse momentum of the reconstructed muon in a simulated $Z \to \mu^+\mu^-$ sample. It is clearly visible that the thresholds on Level 1 and Level 2 (both 7 GeV/c) differ from the value for Level 3 (15 GeV/c). At the same time one can clearly see that the turn-on curve becomes steeper with every step as the increasing amount of available information improves the accuracy of the trigger candidate reconstruction. The efficiency reaches its plateau at about $p_T^\mu = 20$ GeV/c which coincides with the chosen threshold for the reconstructed muons in the $Z \to \mu^+\mu^-$ analysis.

The trigger efficiency for HLT_Mu15 is shown in Figure 6.5 as a function of the

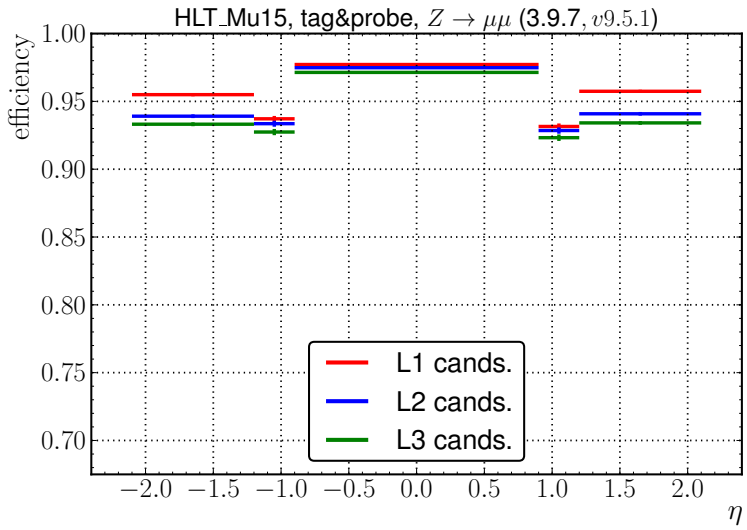

Figure 6.5.: Trigger efficiency as a function of the pseudorapidity of the reconstructed muon for the HLT_Mu15 algorithm. The bins correspond to the central, the intermediate and the forward region of the detector.

pseudorapidity of the reconstructed muon. The plot demonstrates the dependency of the reconstruction efficiency on the actual structure of the detector. The clear deterioration in the transition region from $|\eta| = 0.9$ to $|\eta| = 1.2$ (see also Figure 3.11) is connected to muon tracks that are distributed over the barrel and the endcap in the overlap region. This worsens the Level 1 reconstruction efficiency as the information is at this step allocated after a local reconstruction in each sub-detector. Moreover, the plot reveals clearly that the main inefficiencies of the trigger decision arise from the Level 1 algorithm which has – as mentioned before – only limited information at its disposal.

The comparison of the measured efficiency on data with the estimation based on a simulated sample shows distinct differences. Figure 6.6 indicates that an imperfect description of the Level 1 step is the main source for the deviation while the agreement for the High Level Trigger is quite good. Table 6.3 lists the numerical values of the efficiencies for both data and Monte Carlo samples as well as the ratio of both efficiencies. This ratio acts as a correction factor for analyses that use the single muon trigger.

6.4.2. Isolated Muon Trigger

With increasing beam intensities, the thresholds for all single muon triggers have to be raised. The alternative introduction of prescales should be avoided since it heavily reduces the number of event gain per collected amount of data. While

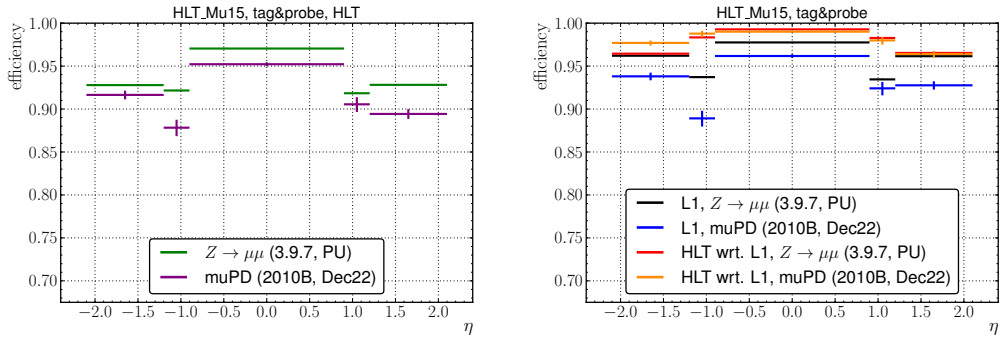

Figure 6.6.: HLT_Mu15 trigger efficiency as a function of the pseudorapidity for data and Monte Carlo samples. The right plot reveals that the description of the High Level Trigger is quite good in the detector simulation (red/orange) while there are clear discrepancies for the simulation of the Level 1 trigger (black/blue).

Table 6.2.: Trigger efficiency for the HLT_Mu9 trigger for data and simulated events.

Data Sample	absolute pseudorapidity			
	$0.0 - 0.9$	$0.9 - 1.2$	$1.2 - 2.1$	$0.0 - 2.1$
simu. $Z \to \mu^+\mu^-$ sample	0.970	0.920	0.928	0.948 ± 0.001
data sample (2010A)	0.934	0.745	0.872	0.881 ± 0.008
data sample (2010B)	0.944	0.864	0.896	0.915 ± 0.005

the selection of $Z \to \mu^+\mu^-$ events can also be done with a double muon trigger, i. e. requiring the existence of two muons already at Level 1, this is not possible for channels with only one muon in the final state, such as $W \to \mu\nu$. The implementation of isolation requirements can bypass this problem to some extent. However, it also introduces additional sources of inefficiencies. Due to the aforementioned time constraints, the isolation calculation differs for the trigger and the offline reconstruction and selection in the analyses.

The trigger efficiency can be measured as a function of an arbitrary isolation quantity by dropping the isolation requirement on the probe muon. For consistency, the tag muon has to fulfil the same type of isolation using standard values as thresholds (see Table 6.4). All other selection criteria concerning the kinematic and the quality properties remain unchanged.

Figure 6.7 shows the efficiency in the data and Monte Carlo samples for tracker and calorimeter based isolation. These two quantities are sensitive to distinct parts of both the detector and the trigger algorithm. There are major differences between the two data samples for the triggers with isolation criteria, i. e. the reason for the difference is likely to arise from the isolation itself. The absolute difference for the

Table 6.3.: Trigger efficiency for the HLT_Mu15 trigger for data in the 2010B period and a Monte Carlo sample.

Data Sample	absolute pseudorapidity			
	$0.0 - 0.9$	$0.9 - 1.2$	$1.2 - 2.1$	$0.0 - 2.1$
simu. $Z \to \mu^+\mu^-$ sample	0.970	0.920	0.928	0.948 ± 0.001
data sample (2010B)	0.952	0.892	0.905	0.927 ± 0.002

Table 6.4.: Standard values for the isolation cut in the analysis of the trigger efficiencies as a function of the isolation criteria.

Isolation Type	Standard Value
Tracker isolation	3 GeV/c
Calorimeter isolation	3 GeV
Relative combined isolation	0.15
Rel. comb. Particle Flow isolation	0.15

first bins can be explained by the imperfect Level 1 description. The differences between the shapes are studied in the following in detail.

The efficiency can also be studied individually for each step of the trigger algorithm. Figure 6.8 shows the efficiencies with respect to the previous step for the simulated sample of Drell-Yan processes; the analogous presentation for data is not conclusive due to the large statistical uncertainties. Especially the efficiency for the pixel track isolation on Level 3 is striking as the threshold

$$\sum p_{\mathrm{T}}^{\text{pixel tracks}} \leq 1.1 \text{ GeV}/c$$

does not reflect in the results at all.

Figure 6.10 depicts the same efficiencies as before when using the latest configuration for trigger used during the 2010 data taking process. Simulation and data now show much better agreement. In the course of this study it turned out that the configuration for pixel track isolation had been faulty until the end of October 2010: The reference point was wrongly set to the origin of the coordinate system instead of using the position information of the beam spot. As simulated events are generated at a different position nearly all tracks were omitted when calculating the pixel track isolation quantity (see also Figure 6.9). As a consequence the isolation criterion was mostly ineffective.

A large portion of the 2010 data ($\approx 30\,\mathrm{pb}^{-1}$) is also affected but the effect is limited as the beam spot is in most cases near the origin of the coordinate system for data and is thus well covered by the radius used for the track vertex association. The agreement between real and simulated events is satisfying and

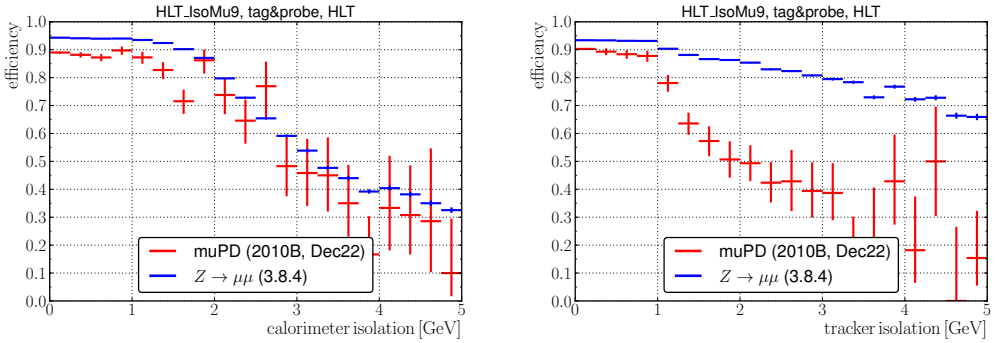

Figure 6.7.: HLT_IsoMu9 trigger efficiency as a function of the deposited energy around the muon direction for data and Monte Carlo samples: the left plot presents the results for a calorimeter based isolation, the right plot the same quantities for a tracker based isolation. The latter one is not well descibed by the simulation (see text).

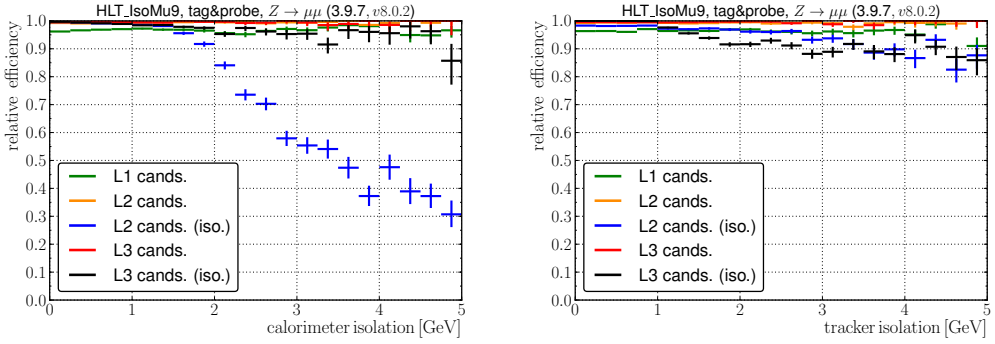

Figure 6.8.: Efficiencies of each step of the HLT_IsoMu9 algorithm as a function of the deposited energy around the muon direction for a Monte Carlo sample: The thresholds of the calorimeter based isolation (left) are – as expected – visible for the Level 2 isolation requirement (blue). The threshold for the pixel track isolation on Level 3 should be visible in the right plot (black). The reason for the deviation is connected to the trigger design on Level 3 (see text).

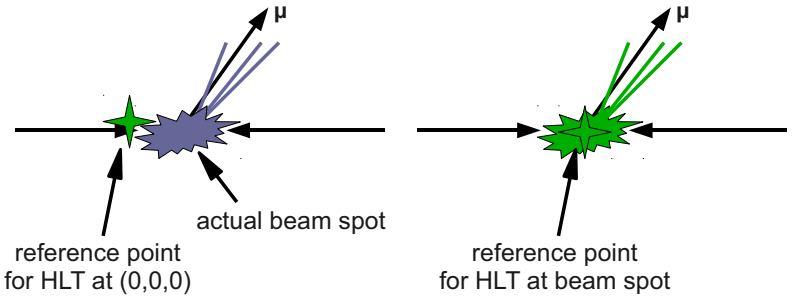

Figure 6.9.: Until end of October 2010, the reference point for the pixel track isolation was wrongly set to the origin of the coordinate system in the isolated muon trigger algorithm (left). As a result, most of the existing tracks were not considered when calculating the isolation quantity for a muon in the Level 3 algorithm. The right plot depicts the correct calculation that is based on the beam spot position (the results can be seen in Figure 6.10).

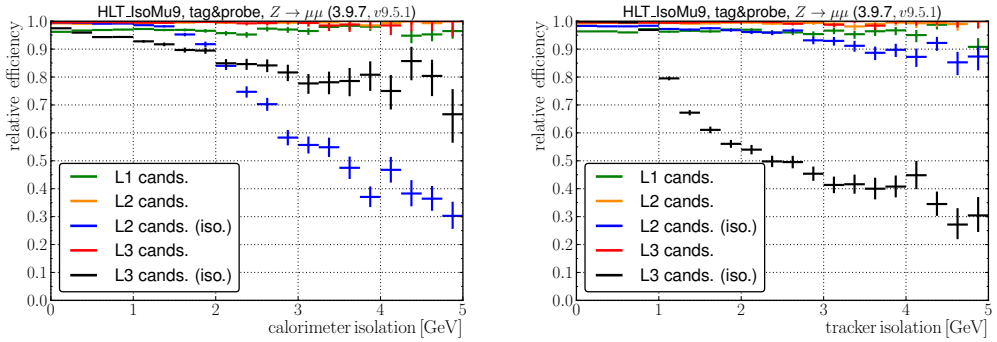

Figure 6.10.: Efficiencies of each step of the HLT_IsoMu9 algorithm as a function of the deposited energy around the muon direction for a Monte Carlo sample: a correct trigger configuration reveals the thresholds of the calorimeter based isolation (left plot) and the threshold for the pixel track isolation on Level 3 (right plot).

within the expected limits. The threshold for the pixel track isolation is clearly visible in both samples. Also the thresholds in the calorimeter based isolation are visible although the decline is smoother due to the η-dependent thresholds. It is also noteworthy that the efficiencies are not expected to drop to zero exactly as the isolation cone is larger in the offline reconstruction. Additionally, the tracker isolation does not evaluate the origin of tracks and their distances to the beam spot in the offline analysis.

Figure 6.11 presents the accumulated efficiencies, i. e. the effective trigger efficiency when applying a cut $\mathrm{Iso}(\mu) < x$ on the reconstructed muons. The large statistical weights of the first bins dominate the whole distribution. However, this well tempered behaviour also implies that the uncertainty on the trigger efficiency arising from possible variations of the isolation quantity or the threshold itself is small, under the assumption that the studied physical process has predominantly clean muons.

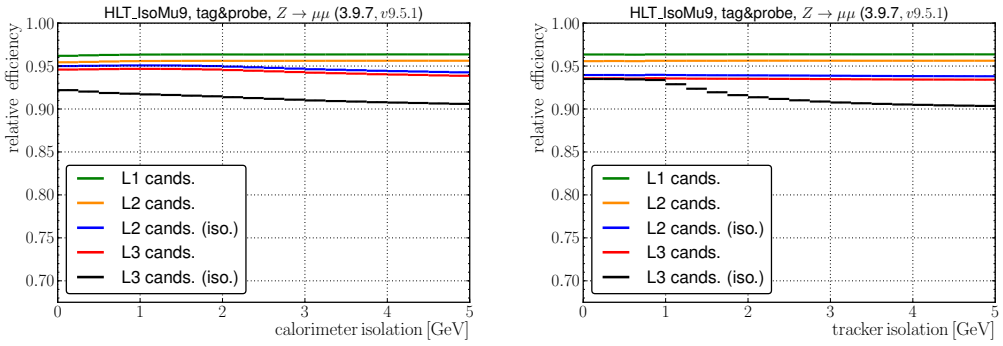

Figure 6.11.: Accumulated efficiencies for the HLT_IsoMu9 algorithm as a function of the deposited energy around the muon direction for a Monte Carlo sample.

Finally, Figure 6.12 depicts the efficiency of an isolated muon trigger with respect to a non-isolated muon trigger with the same thresholds for the muon transverse momentum. This presentation illustrates the very good modelling of the isolation criteria with the muon HLT.

6.4.3. Evolution of the Trigger Algorithm

Although the preparation of the data taking has been done carefully and in great detail, the development of the trigger algorithms is still not finished. At the same time, it is necessary to detect any changes of the trigger efficiencies over time, e. g. a degradation of some hardware component could affect the trigger efficiency. Two examples illustrate this on-going evolution and its implications on analyses.

Figure 6.13(a) shows the single muon trigger efficiency as a function of the pseudorapidity for the two data taking periods in 2010, namely 2010A and 2010B. As explained before the matching of track candidates in the muon system and in the

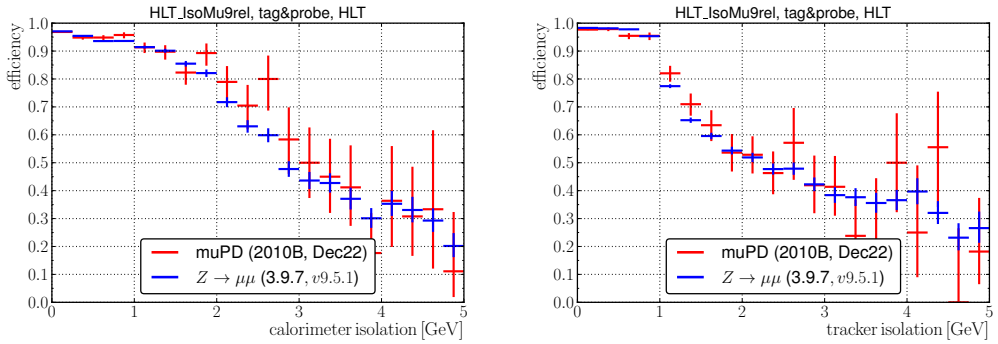

Figure 6.12.: Efficiency of the the HLT_IsoMu9 algorithm with respect to the HLT_Mu9 algorithm as a function of the deposited energy around the muon direction. The prediction based on the Monte Carlo sample agrees well within the statistical uncertainties with the measured values for the data sample.

inner tracking detector could be improved by introducing a cascaded algorithm resulting in an increase of the trigger efficiency in 2010B. This example illustrates the flexibility of a software based trigger system as used for the HLT system.

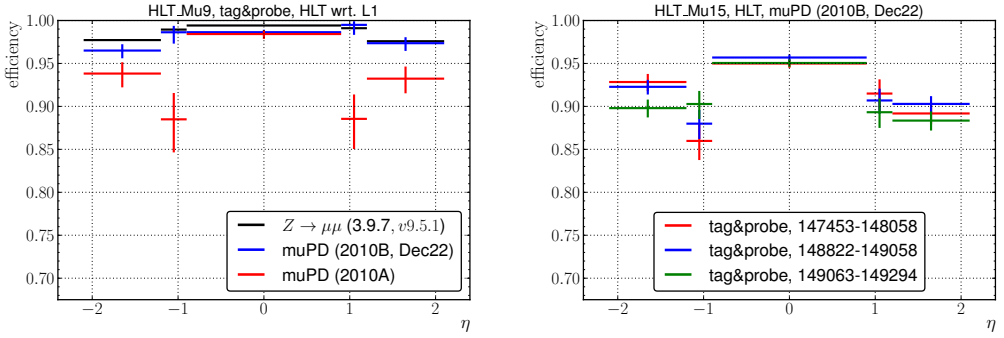

Figure 6.13.: Evolution of the trigger algorithms: The introduction of the cascaded seed finding algorithm for the High Level Trigger in 2010B has clearly improved the efficiency (left plot). The right plot depicts the HLT_Mu15 trigger efficiency as a function of the pseudorapidity for three different run ranges in the data taking period 2010B. Since there were no modifications of the trigger algorithm, the variations are compatible within the statistical fluctuations.

Although difficult with the limited amount of data, it is possible to study the trigger efficiency for different run ranges. Figure 6.13(b) depicts the results for HLT_Mu15 in three different run ranges of similar integrated luminosity from the 2010B run period. The results are compatible within the statistical uncertainties.

6.4.4. Pile-up Dependence

An increase of the instantaneous luminosity generally leads to the occurrence of pile-up events. As these events are mostly scattering processes with low momentum transfer, they are not a source of muons that fulfil the imposed selection criteria. Nevertheless the induced additional activity can spoil the efficiency of muon trigger algorithms, especially if an isolation criterion is applied during the trigger decision process.

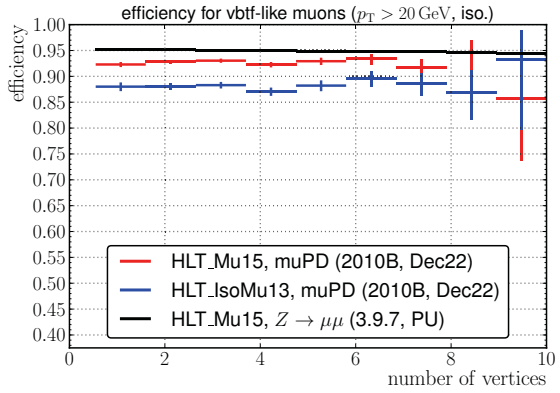

Figure 6.14.: High Level Trigger efficiency as a function of the number of reconstructed vertices. The flat distributions suggest that the dependence of the efficiency on the number of additional events from pile-up contribution is negligible.

Figure 6.14 presents the trigger efficiency as a function of the number of reconstructed vertices. This categorisation is used as this number is a reliable measure for the amount of additional pile-up events. The flatness of the distributions suggest that the dependence of the efficiency on the number of additional events from pile-up contribution is negligible for the considered scenario.

Taking into account the cumulative efficiency as shown in Figure 6.11 it is not expected that higher instantaneous luminosities with an even larger amount of pile-up events will bias the efficiencies drastically.

6.5. Inclusive Measurement

The tag and probe method can be complemented by an inclusive measurement of the trigger efficiencies. Here, the ability to fire a muon trigger is examined for *all* muons in an event as long as they fulfil the selection requirements.

However, it is not possible to use a sample of data events that has been collected using a muon trigger as this would obviously bias the result. This approach needs instead an orthogonal, unbiased data sample based on a jet-based trigger selection. As the number of events containing muons that fulfil all imposed criteria is small

and the muons will originate from hadronic processes in most cases. The resulting statistical precision is therefore much smaller than in the tag and probe method.

Single Muon Candidates

Figure 6.15 shows the comparison of the trigger efficiencies for muons that fulfil the aforementioned requirements on the kinematic properties and the reconstruction quality in data and simulated event samples. The inclusive method has a clear tendency to lower efficiencies compared to the tag and probe method, the results are summarised in Table 6.5.

The differences for the results on a real data sample and a simulated muon-enriched multi-jet sample (see Section 5.2.2) originate again from the the Level 1 algorithm as seen before (see Figure 6.16). The description of the High Level Trigger in software is satisfactory.

Due to the very limited number of isolated muons that are suitable for this study, this approach is not followed further. A detailed study with focus on non-isolated muons in events with hadronic activity can be found in [64].

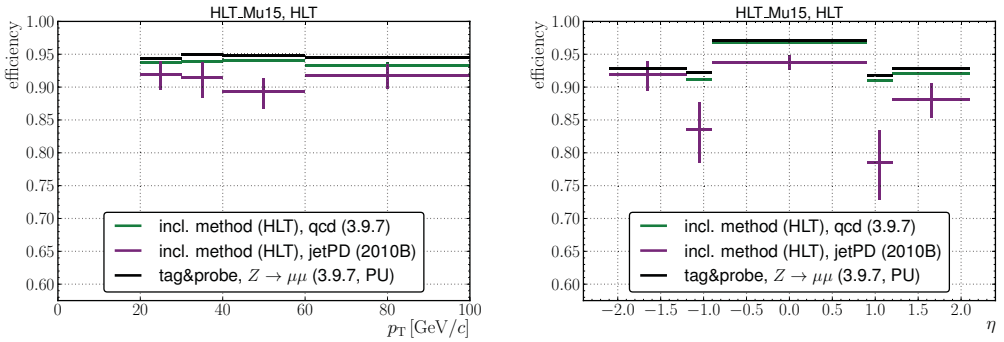

Figure 6.15.: Efficiency of the HLT_Mu15 trigger in a data and a Monte Carlo sample as a function of the transverse momentum and the pseudorapidity of the reconstructed muon. For comparison the black line indicates the result of the tag and probe method on a data sample.

Direct Search for Z $\to \mu^+\mu^-$ Candidates

It is also possible to study Z $\to \mu^+\mu^-$ decays on an orthogonal sample, although the number of candidate events is in this case very limited. In contrast to a muon triggered sample there can also be events where both muons could not initiate a muon trigger decision.

The trigger efficiency can be calculated with

$$\epsilon_{HLT} = \frac{N_1 + 2N_2}{2\,(N_0 + N_1 + N_2)}$$

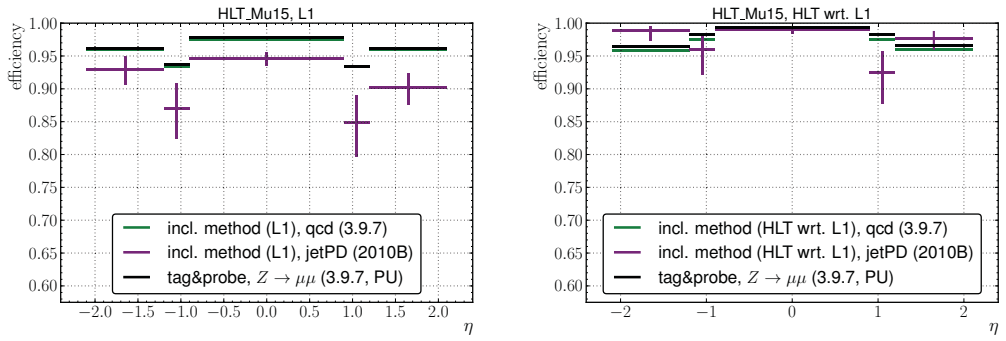

(a) Level 1 efficiency

(b) HLT efficiency with respect to the Level 1

Figure 6.16.: Efficiency of the HLT_Mu15 trigger in a data and a Monte Carlo sample as a function of the pseudorapidity of the reconstructed muon.

Table 6.5.: Trigger efficiency for the HLT_Mu15 trigger for data in the 2010B period and a Monte Carlo sample using single muons in a jet sample. The last line repeats the results for the tag and probe method on data.

Data Sample	absolute pseudorapidity			
	$0.0 - 0.9$	$0.9 - 1.2$	$1.2 - 2.1$	$0.0 - 2.1$
simulated QCD sample	0.968	0.911	0.920	0.937 ± 0.001
data sample	0.938	0.811	0.900	0.906 ± 0.010
tag and probe method (data)	0.970	0.920	0.928	0.948 ± 0.001

where N_i is the number of events with i muons from the $Z \to \mu^+\mu^-$ decay that could initiate a muon trigger decision. The resulting efficiencies are listed in Table 6.6 and agree within the large uncertainties with the results of the other approaches in this chapter.

Beside this inclusive measurement the orthogonal sample offers as well the possibility to detect correlations of the trigger decision in di-muon events. The correlation is here defined as the linear correlation between the decision for the positively charged muon and the negatively charged muon. The results that are given in Table 6.6 confirm the a priori expectation that the trigger decision is not correlated to the muon charge.

6.6. Conclusion

The understanding of the muon trigger algorithms is essential for a Z boson production cross section measurement and all other analysis depending on muon triggers. As a contribution to the official trigger performance measurement, two indepen-

Table 6.6.: Inclusive measurement of the trigger efficiency with $Z \to \mu^+\mu^-$ candidates: The trigger efficiencies agree within the large statistical uncertainties with the results for the tag and probe method and the inclusive method. The linear correlation factor between the trigger decision for μ^+ and the decision for μ^- is compatible with 0. All uncertainties indicate the 68% confidence level.

trigger	0 HLT	1 HLT	2 HLT	efficiency	lin. correlation
HLT_Mu9 (2010A)	1	11	31	$0.85^{+0.06}_{-0.08}$	$+0.00^{+0.16}_{-0.15}$
HLT_Mu9 (2010B)	0	9	32	$0.89^{+0.05}_{-0.07}$	$-0.12^{+0.16}_{-0.15}$
HLT_Mu11	1	16	52	$0.87^{+0.04}_{-0.06}$	$-0.02^{+0.13}_{-0.12}$
HLT_Mu15	1	9	41	$0.89^{+0.05}_{-0.06}$	$+0.10^{+0.13}_{-0.15}$

dent data-driven measurements for the the single muon trigger efficiency have been introduced at the beginning of this chapter and subsequently applied to the data sample collected in the first year of the LHC operations. It could be demonstrated that the largest deviations of the trigger efficiency arise from an imperfect description of the Level 1 step of the trigger in simulation while the High Level Trigger description is very good. In addition, an unintended configuration of the isolated muon trigger algorithm could be revealed and explained. The results of the studies in this chapter are used as input to both the official CMS muon trigger performance study and the other chapters in this work.

7. Modelling of $Z \to \tau^+\tau^-$ Events

The decay of a Z boson into tau leptons is similar to a decay into muons. However, the larger mass of the tau leptons allows a variety of possible final states for the Z boson.

In the long run, Z boson decays into tau leptons are of great importance since a light Standard Model Higgs boson does also decay into pairs of tau leptons. The coupling of the Higgs boson to tau leptons is larger than for electrons and muons due to the larger mass. For a $H \to \tau^+\tau^-$ search, the $Z \to \tau^+\tau^-$ decays represent the most important background contribution and a detailed understanding is thus mandatory.

Uncertainties on the shape and the absolute normalisation of the $Z \to \tau^+\tau^-$ events directly affect the uncertainty of the estimated significance of a discovery of the Higgs boson. The estimation of this background contribution is challenging and data-driven methods for an estimation of the $Z \to \tau^+\tau^-$ contribution are needed. In the scope of this work, a data-driven method to tackle these issues using reconstructed $Z \to \mu^+\mu^-$ events has been developed, tested and applied on a 2010 data sample as well as on samples of simulated events. While any measurement of $Z \to \tau^+\tau^-$ events is possibly polluted with $H \to \tau^+\tau^-$ events, the Higgs boson contribution to a $Z \to \mu^+\mu^-$ measurement is negligible due to the very small branching ratio $\mathrm{BR}(H \to \mu^+\mu^-)$.

At the beginning of this chapter, the basic principles for a reconstruction of $Z \to \tau^+\tau^-$ candidates are presented and the interplay with Higgs boson searches is outlined. Following these introductory sections, a data-driven method for the estimation of $Z \to \tau^+\tau^-$ events is introduced and explained. The validity of the proposed method and its predictive power is then examined with simulated events. The chapter finally concludes with an exemplary application on the 2010 data sample.

7.1. $Z \to \tau^+\tau^-$ Decays

Tau leptons can decay leptonically into a muon or an electron but a hadronic decay into a so-called τ-jet is possible as well. Table 7.1 lists the main decay modes for a tau lepton which are dominated by hadronic decays. As described in Section 3.4.2, the identification of the resulting τ-jets is challenging and even a small mis-identification rate of gluon and quark induced jets can spoil the analysis of $Z \to \tau^+\tau^-$ events. Furthermore, it is difficult to identify these events with High Level Trigger algorithms. As a consequence analyses preferably restrict themselves to decays with at least one lepton.

The decays into two lighter leptons,

$$\mathrm{Z} \to \tau\tau \to ll + 4\nu \quad \text{with} \quad l = e, \mu \ ,$$

have characteristic final states. This holds especially for the mixed final state with one electron and one muon as processes mimicking this decay are rare. Analyses exploiting the decay into two muons have to cope with a large contribution from $\mathrm{Z} \to \mu^+\mu^-$ decays which has to be suppressed. The final state with two muons is described in [134].

The semi-leptonic decay with one hadronically decaying tau lepton and one tau lepton decay into a lighter lepton,

$$\mathrm{Z} \to \tau\tau \to \mu + \tau\text{-jet} + 3\nu,$$

is a good trade-off between a characteristic signature and sufficiently large statistical precision. This specific decay mode has an overall branching ratio of about 23%. A cross section measurement and other studies are feasible with the 2010 data sample and first conclusions for future analyses are possible [135].

Table 7.1.: Overview of the main tau decay modes [4]. In contrast to Table 3.4, the listed decay modes include decays with neutral kaons. For reasons of readability the neutrinos are not listed in this table.

Decay Mode	Fraction
$\tau^\pm \to e^\pm$	17.85%
$\tau^\pm \to \mu^\pm$	17.36%
$\tau^\pm \to \pi^\pm$	10.91%
$\tau^\pm \to \pi^\pm\pi^0$	25.51%
$\tau^\pm \to \pi^\pm\pi^0\pi^0$	9.51%
$\tau^\pm \to \pi^\pm\pi^\pm\pi^\mp$	9.80%
$\tau^\pm \to \pi^\pm\pi^\pm\pi^\mp\pi^0$	4.75%
other decay modes	4.47%

7.1.1. Event Topology

The final state for the semi-leptonic decay depicted in Figure 7.1 is characterized by the tau decay products, namely a muon, a tau induced jet and at least three neutrinos.

The neutrinos cannot be detected in the CMS apparatus due to their very low interaction rate with matter. They carry a certain amount of the overall momentum away, leaving an imbalance in the sum of the momenta of all visible particles.

Momentum conservation can help to reconstruct the sum of all escaping neutrinos partially. As proton remnants and other particles from the collisions can

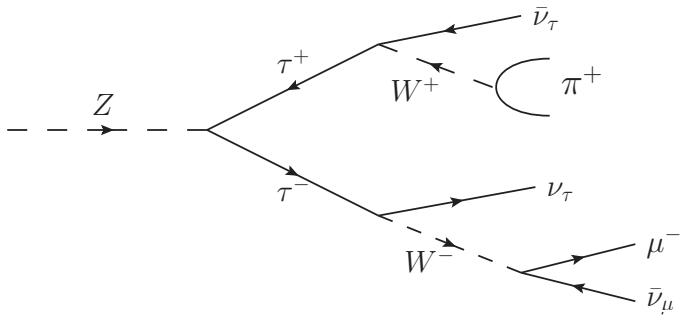

Figure 7.1.: Exemplary Feynman graph for a $Z \to \tau\tau \to \mu + \tau-$jet decay where the leptonically decaying tau lepton decays into a positively charged pion. The neutrinos are not detectable and produce a certain amount of missing transverse energy.

exit undetected through the beam pipe, where no calorimeters can be placed for technical reasons, the following consideration is restricted to the plane perpendicular to the beam direction. With a negligibly small transverse momentum of the incoming parton, the vectorial sum over all measured particles yields the so-called missing transverse energy (with a negative sign). In a simple approach, the missing transverse energy corresponds to the negative vectorial sum of the readout cells of the calorimeter and the muons which cannot be detected in the calorimeter. In the picture of the Particle Flow algorithm, the missing transverse energy is calculated simply through the sum over all stable particles.

7.1.2. Background Processes

The selection of $Z \to \tau\tau \to \mu + \tau-$jet[1] decays suffers from all processes with an energetic muon and a quark- or gluon-induced jet spuriously identified as a τ-jet.

Multi-jet events can exhibit energetic muons originating from heavy flavour decays or decays in flight. An additional misidentified jet then results in a contribution to the $\tau\tau \to \mu + \tau-$jet selection. Since the jet and the muon are uncorrelated, their electrical charges are random. It is thus possible to estimate the absolute normalisation through events where both objects carry the same charge [136].

Events with a W boson and additional jets can mimic the studied Z boson decays in a similar way. In contrast to the multi-jet contribution, the muons are real, isolated and the reconstructed muon objects yield a high quality. Although a $W \to \tau \to \mu$ decay is possible, the contribution from direct decays of the W boson into a muon is larger.

Z boson decays into pairs of muons are similar to a $Z \to \tau\tau \to \mu + \tau-$jet decay if one of the two muons is not reconstructed due to inefficiencies of the detector. Furthermore, it is possible that one of the muons – together with some deposited energy – is falsely identified as a τ-jet. However, special selection criteria which

[1] For reasons of clarity and readability neutrinos are not listed explicitly in the following.

are described later are able to suppress this contribution sufficiently for the semi-leptonic final state.

Finally, decays of top quark pairs and pair production of electroweak gauge bosons are sources of real tau lepton pairs. Due to the small combination of their production cross section and branching ratio, theses contributions only mildly affect the final results.

7.1.3. Event Selection

The selection of $Z \to \tau\tau \to \mu + \tau-$jet events follows the official CMS guideline and are laid out in [136] and [137]. The various steps are briefly described and motivated without any further study in the next paragraphs.

Muon Selection

The occurrence of neutrinos in the tau decays leads to a smaller momentum for the muon and the τ-jet compared to the originally decaying taus. Figure 7.2 depicts the distributions of the transverse momenta at generator level for the taus and their decay products. Although muons are required to fulfil the same quality criteria as in the selection of $Z \to \mu^+\mu^-$ events, it is necessary to lower the threshold for the transverse momentum to 15 GeV/c to preserve the statistical precision after the application of all selection criteria. An even lower threshold would conflict with the implicit selection given by thresholds of the muon trigger algorithm which selects the studied events. Nevertheless, the muon trigger efficiency is in this case susceptible to additional resolution effects occurring in the temporary muon reconstruction during the trigger decision making process as shown in the right plot of Figure 6.1. However these effects are assumed to be small and a further study is out of the scope of this work.

Tau Selection

The identification of the hadronically decaying tau leptons is based on the HPS algorithm (see Section 3.4.2). All candidates with a transverse momentum above 20 GeV/c are considered for the following steps. The loose, inherent isolation criterion of the HPS algorithm already suppresses a large fraction of quark and gluon induced jets. For technical reasons single muons and electrons can also be identified as τ-jets. It is thus necessary to reject these two sources of fake tau candidates. The muon rejection is based on the presence of compatible reconstructed tracks in the muon system. The rejection of electrons exploits the negligible fraction of energy deposited by an electron in the hadron calorimeter. Tau candidates are dismissed if they fail one of the two veto requirements.

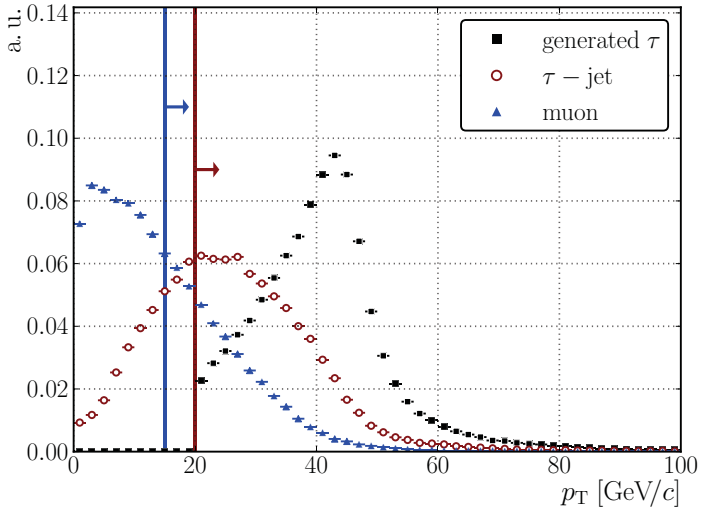

Figure 7.2.: Comparison of transverse momenta at generator level in $Z \to \tau^+\tau^-$ decays with $p_T^{\tau,\,gen} > 20$ GeV/c: the spectrum for the muon originating from the leptonic tau decay is softer than the spectrum for the visible part of the hadronically decaying tau since it includes one additional neutrino. The solid lines indicate the thresholds for the reconstructed transverse momenta during the selection process. All distributions are scaled to unity.

Further Requirements

All muons and τ-jets surviving the aforementioned preselection are then combined to di-tau candidates if they carry opposite charges and are not overlapping in the $\eta - \phi$ plane, i. e.

$$\Delta R\,(\mu, \tau - \text{jet}) > 0.5\ .$$

The contribution from $Z \to \mu^+\mu^-$ events can be further reduced by rejecting all events that contain a second isolated muon ($I_{rel}^{PF} < 0.26$) with a transverse momentum exceeding 10 GeV/c.

In the last step of the selection process, the background contribution arising from $W^\pm \to \tau^\pm\nu$ and $W^\pm \to \mu^\pm\nu$ is reduced through a W boson reconstruction attempt. The missing transverse energy and the momentum of the reconstructed muon are input to a calculation of the so-called transverse mass

$$M_T = \sqrt{2p_T^\mu E_T^{miss} \cdot \left(1 - \cos\Delta\phi\left(\mu, E_T^{miss}\right)\right)}\ .$$

Candidates are rejected if the transverse mass exceeds 40 GeV/c^2. Figure 7.3 illustrates that this chosen threshold is able to suppress a large fraction of events coming from electroweak background processes.

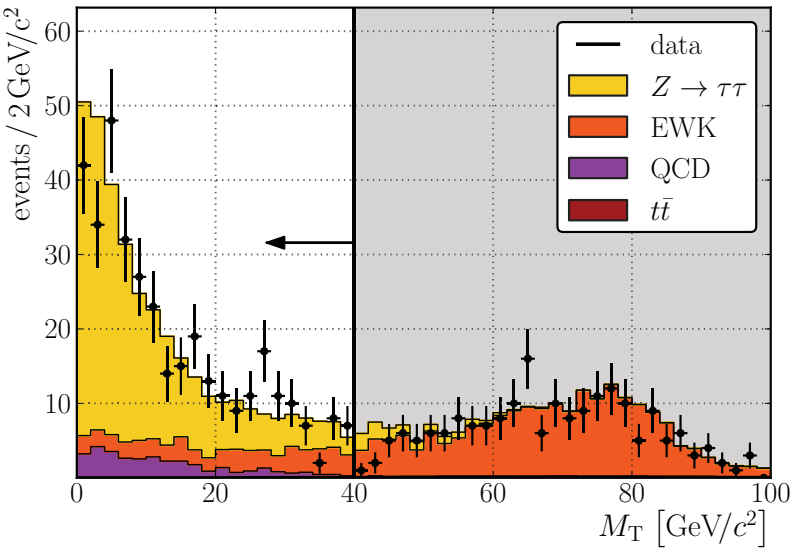

Figure 7.3.: Distribution of the transverse mass after all other selection steps. The shaded area with a large fraction of tau lepton pairs from electroweak background processes is excluded.

7.1.4. Mass Reconstruction

Resonances decaying into pairs of muons or electrons can be easily reconstructed. In this case the resolution of the mass measurement is dominated by the resolution of the momentum or the energy reconstruction of the detector apparatus, respectively. The reconstruction of a tau lepton is more complicated since at least two neutrinos from the decays escape the detector without any measurable interaction with the detector material.

The loss of information due to the collapse of all neutrino momenta into one two-dimensional vector, the mass reconstruction of a tau lepton pair cannot be perfect. Several approaches and estimative algorithms have been developed over the time to tackle this problem. Figure 7.4 presents the results for the three different mass definitions that are explained in the following.

Visible Mass

The visible mass neglects any contribution from the neutrinos and sums up only the visible tau lepton decay products. These are the muon and the τ-jet, resulting in an underestimation of the mass of the intermediate boson. The separation of a potential light Higgs boson and the dominating Z resonance is thus more complicated than with the other methods described in the following. The clear advantage for first observations is however the independence from the reconstruction of the

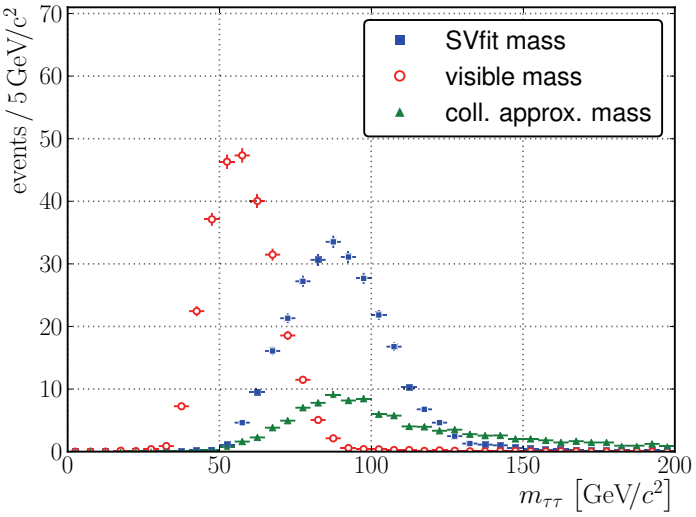

Figure 7.4.: Comparison of the distributions for the visible mass, the collinear approximation and the SVfit method in simulated $Z \to \tau\tau \to \mu + \tau$–jet events. The loss of events during the mass calculation with the collinear approximation is clearly visible.

missing transverse energy.

Collinear Approximation

In decays of high energetic, boosted tau leptons, both the neutrinos and the visible decay products are in general close to the original direction of the tau lepton in three-vector space. With this assumption of collinearity the missing energy can be projected onto the direction of the visible decay products to finally obtain the unavailable z-component of the missing energy.

The collinear approximation defines the fraction x_i of the tau transverse momentum as the fraction of the visible transverse momentum $p_{\mathrm{T}}^{\mathrm{vis}_i}$ and the yet unknown tau transverse momentum $p_{\mathrm{T}}^{\tau_i}$. With this information, the mass of the intermediate resonance can be approximated as

$$m_{\tau\tau} = \frac{m_{\mathrm{vis}}}{\sqrt{x_1 x_2}} \,.$$

Appendix B.2 describes this method in more detail.

The collinear approximation causes a broadening of the invariant di-tau mass distribution as Figure 7.4 shows. Hence the tail of invariant mass distribution of the irreducible background coming from $Z \to \tau^+\tau^-$ events interferes with the Higgs boson signal peak. It is important to note that this contribution is irreducible. The resolution of the mass reconstruction is further affected by the limited resolution of the detector and any imprecision of the reconstruction of the occurring physical objects.

A potential Higgs boson is produced preferably at rest and the decay products are then emitted back-to-back. This leads to a small or - in the worst case - to no measurable missing transverse energy at all. The application of the collinear approximation then fails. The same holds for cases where the fractions x_i come out unphysical, i. e. $x_i \notin (0, 1)$. Such events have to be omitted leading to a severe loss of statistical precision.

Secondary Vertex Fit Method

The Secondary Vertex Fit (SVfit) approach is a recently developed method which is based on the maximisation of a likelihood function to give a mass hypothesis for the di-tau pair [138]. The input values are given by the kinematical properties of the reconstructed tau lepton decay products and the missing transverse energy. The construction of the likelihood function is described in detail in [138].

Various coordinate transformations exploit the topologies of tau lepton decays to improve the results of the likelihood function. In this context it is important to note that the construction of the likelihood function incorporates information gathered on samples of simulated events. Some parts of the likelihood, e. g. some assumption on the missing transverse energy resolution, also require a fine tuning with data.

The eponymous fit of secondary vertices resulting from the tau lepton decays is currently not used since the uncertainties on the vertex reconstruction are too large. However, the constraint given through the tau lepton lifetime could give additional information for the mass reconstruction in the future.

Contrary to the collinear mass approximation, the SVfit method is able to compute an invariant di-tau mass hypothesis for every event. Furthermore, the width of the distribution is smaller and the mass distribution peaks near the nominal Z mass for a sample of $Z \to \tau^+\tau^-$ decays. The well-defined shape of the resulting mass distribution simplifies a distinction between a Z boson induced background contribution and a potential light Higgs boson. In other words, the SVfit method yields larger significances or tighter exclusion limits for Higgs boson searches.

7.1.5. Results for the 2010 Data Sample

Figure 7.5 and Figure 7.6 show the reconstructed mass for $\tau\tau \to \mu + \tau-$jet candidates in the 2010 data sample using the discussed mass reconstruction methods. The background contributions are scaled according to their cross sections and the integrated luminosity. The imperfect description of the trigger algorithm in simulation is considered by the corresponding correction factor as explained in Section 6. More kinematical distributions can be found in Appendix B.3.

Prediction and actual measurement agree within the statistical uncertainties. As expected the calculation of the invariant di-tau mass using the collinear approximation exhibits a worse statistical precision compared to the lossless prediction via the secondary fit or the visible decay products.

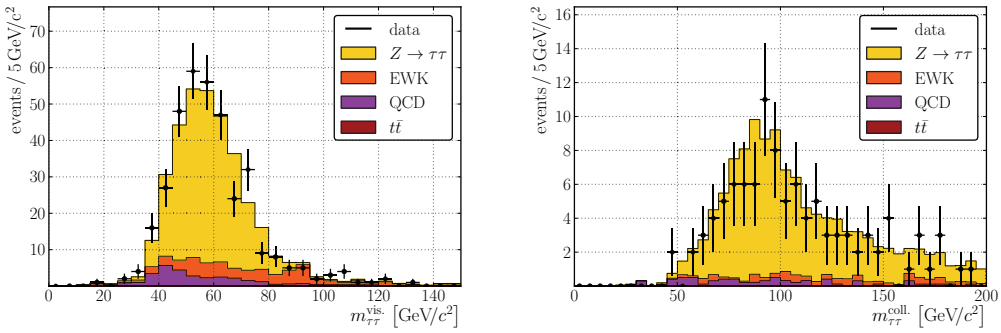

Figure 7.5.: Comparison of the reconstructed mass for $\tau\tau \to \mu + \tau$−jet candidates in the data sample in simulated event samples using the visible mass definition (left) and the collinear approximation (right). The simulated samples are scaled according to their production cross sections and the integrated luminosity.

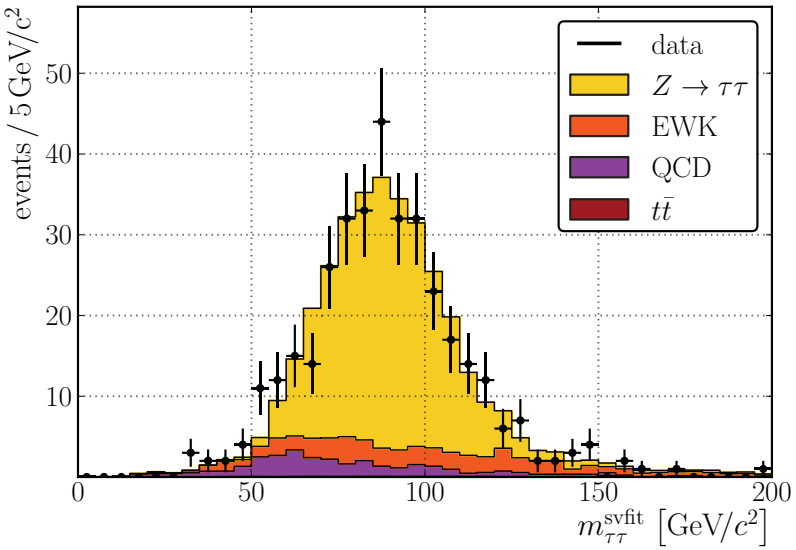

Figure 7.6.: Comparison of the reconstructed mass for $\tau\tau \to \mu + \tau$−jet candidates in the data sample in simulated event samples using the SVfit method. The simulated samples are scaled according to their production cross sections and the integrated luminosity.

7.2. Relevance of $Z \to \tau^+\tau^-$ for Higgs Searches

The search for the Higgs boson is one of the major tasks of the CMS experiment. As outlined in Section 2.7, electroweak precision measurements and direct searches at previous experiments favour a Higgs boson mass below 135 GeV/c^2. The decay into two tau leptons is the dominant leptonic decay mode since the coupling of the Higgs boson is proportional to the mass of the involved particles.

The significance of a discovery can be estimated with statistical means. The discriminating variable for this purpose is usually the invariant mass of the reconstructed tau leptons and their decay products, respectively. An observed excess in a particular mass range has to be large enough to exclude random statistical fluctuations of the background.

Since the Z boson and the Higgs boson differ only in spin and mass, the final states of the decays into tau leptons are very similar. Figure 7.7 illustrates the mass distributions for Higgs bosons and Z bosons. The Higgs signal thus shows up as an excess on the tail of the Z boson mass distribution as shown in Figure 7.8. The $Z \to \tau^+\tau^-$ contribution is shown together with other background contributions and the results from the 2010 data sample. It is important to note that the Higgs boson production cross section is enhanced by a factor of 10 for illustrative purposes in the representation.

The determination of the significance is sensitive to the modelling of the $Z \to \tau^+\tau^-$ contribution as dominating background process. The theoretical uncertainties on the prediction of the total number of these background events and the uncertainty on the shape of the tail have great influence on the systematic uncertainty of the expected significance. It is thus unavoidable to exploit methods which reduce both classes of uncertainty. The data-driven estimation of $Z \to \tau^+\tau^-$ events shown in the following is such a data-driven approach that can help to improve the confidence of a Higgs boson discovery.

7.3. Data-driven Estimation of $Z \to \tau^+\tau^-$ Events

The combination of reconstructed $Z \to \mu^+\mu^-$ events from data and separately simulated tau lepton decays is a possible way to estimate the shape of all relevant kinematic distributions in $Z \to \tau^+\tau^-$ events as well as their absolute normalisation. To retrieve a $Z \to \tau^+\tau^-$ event from a measured $Z \to \mu^+\mu^-$ event it is necessary to remove the two muons and replace them by the decay products of simulated tau leptons with the same energies and the same direction. The result is an *embedded event* where large parts of the events is inherited from a real event. Therefore, it is not necessary to model effects such as pile-up and the underlying event. Uncertainties associated to these models due to possible imperfect descriptions in simulation thus vanish.

The production of events that combine a reconstructed event and a simulated partial event, which contains the $\tau^+\tau^-$ decay, can be done basically in two ways.

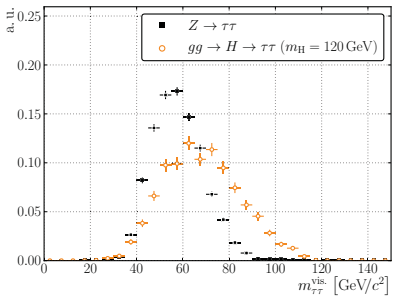

(a) visible mass

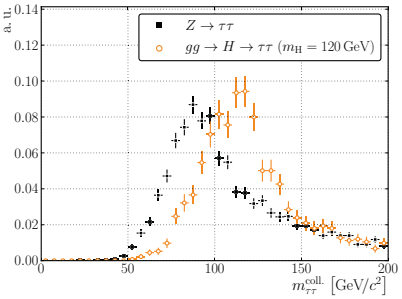

(b) collinear approximation

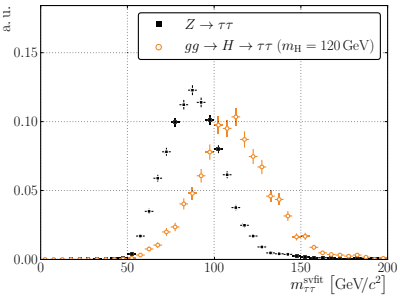

(c) secondary vertex fit mass

Figure 7.7.: Comparison of the shape of the invariant mass spectra of Z $\to \tau^+\tau^-$ and H $\to \tau^+\tau^-$ events with different reconstruction methods. All distributions are scale to unity. The smaller width of the SVfit mass distribution compared to the result of the collinear approximation leads to a higher significance when performing a Higgs search.

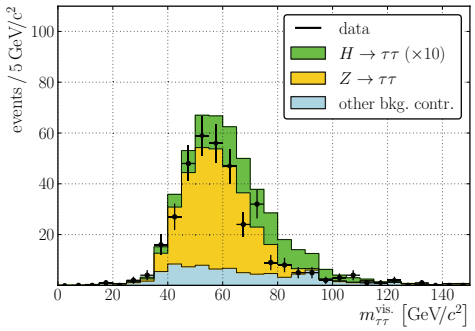

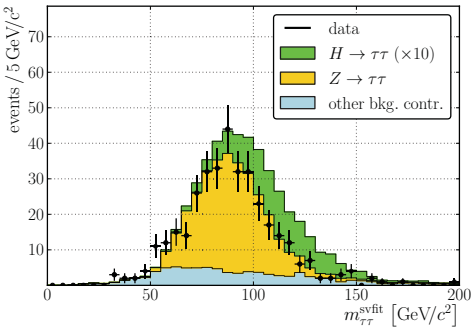

Figure 7.8.: Comparison of the invariant mass spectrum in the data sample and simulated samples using the visible mass definition (left) and the secondary vertex fit method (right) for a Higgs mass of 120 GeV/c^2. The Higgs cross section is multiplied by a factor of 10 for illustrative purposes. Both representations indicate that a precise knowledge of the background contribution arising from Z decays is necessary to detect a possible Higgs signal.

Both approaches are outlined in the following and they both allow the subsequent application of standard analysis code although the complexity is different.

7.3.1. Overlay on the Level of Digitized Output

Two events can be merged by adding values of the digitised output of the real detector and the detector simulation. At this level simulation and data acquisition are technically identical. All reconstruction algorithms including the trigger decision process this raw data. As a consequence this approach leads to overlaid events in a very natural way including a simulation of the trigger decision for the hybrid event. The overlay on the level of the digitized output has been studied for simulated events in [139] before the start of the LHC.

However, this method requires a precise description of the detector geometry in the simulation. Any deviation of the underlying geometry model would lead to measured quantities at non-physical locations in space during the merging process. The result would be the appearance of tracks or other physical objects at incorrect positions and an untrustworthy modelling of hybrid events.

Measurements show that in reality the silicon tracker is slightly shifted relative to the nominal centre of the detector and the other sub-systems [140]. This displacement is illustrated in Figure 7.9. Additionally, the two independent halves of the tracking detector are slightly tilted towards each other and show a small longitudinal movement over time [141, 142]. These effects are under observation but there are no efforts to reflect these movements in the geometry used for the simulation of events.

It is important to note that this effect neither affects the reconstruction of simulated events nor the reconstruction of real events as the geometry models for both reconstruction processes are self-consistent and – for data – based on data-driven alignment procedures.

As a consequence this approach is currently not applicable on real data events and is not used throughout this analysis.

7.3.2. Overlay on the Level of Intermediate Objects

A different approach in the overlay employs the two-tiered Particle Flow algorithm. A first step yields a collection of plain tracks and intermediate objects, so-called particle candidates. They are produced on the basis of information from the various sub-detectors. Afterwards the actual identification of physical objects such as electrons, photons or τ-jets takes place in a second step.

As a logical consequence it is also possible to merge two events using these candidate objects which contain all required information for the following steps. At the same time it is obvious that this approach is not suited for analyses that make use of lower level objects. This includes analyses where the hadronically decaying taus are reconstructed solely with calorimeter information. However, nowadays

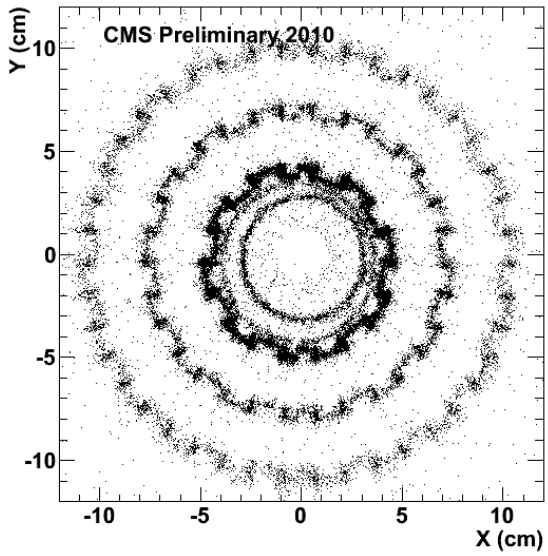

Figure 7.9.: Visualisation of the tracker displacement based on the position of photon conversions into electron positron pairs with $|z| < 26\,\text{cm}$. As the probability of a conversion process increases with the atomic number and the density of the traversed material, the density of the reconstructed conversion vertices is a measure for the material budget. The innermost ring corresponds to the beam pipe which is centred with respect to the nominal reference point. The three cog wheel like structures depict the three layers of the silicon pixel detector which are shifted with respect to the reference frame [140].

all major tau analyses are restricted to objects reconstructed by the more precise Particle Flow algorithm and this drawback is only a theoretical one.

The imprecise model of the actual detector geometry in simulation does not affect this approach as the resulting physical objects are abstracted from the geometry.

A clear disadvantage of the method is the inability to perform a trigger decision on the hybrid event. The trigger algorithm can only perform on the partial event that is simulated and implanted. As the event selection of the di-tau events can always rely only on the existence of the characteristic decay products, the difference to the previous approach is only the lack of the underlying event during the trigger decision process. The 2010 data sample studied in this thesis is not affected as only a non-isolated single muon trigger has been used for the tau analyses.

As a summary, it is important to note that all current tau analyses using Particle Flow objects can make use of hybrid events and that – based on the current situation – the trigger decision can be modelled in a reliable way. The overlay on the level of intermediate objects is thus the best choice until the detector geometry in simulation is improved.

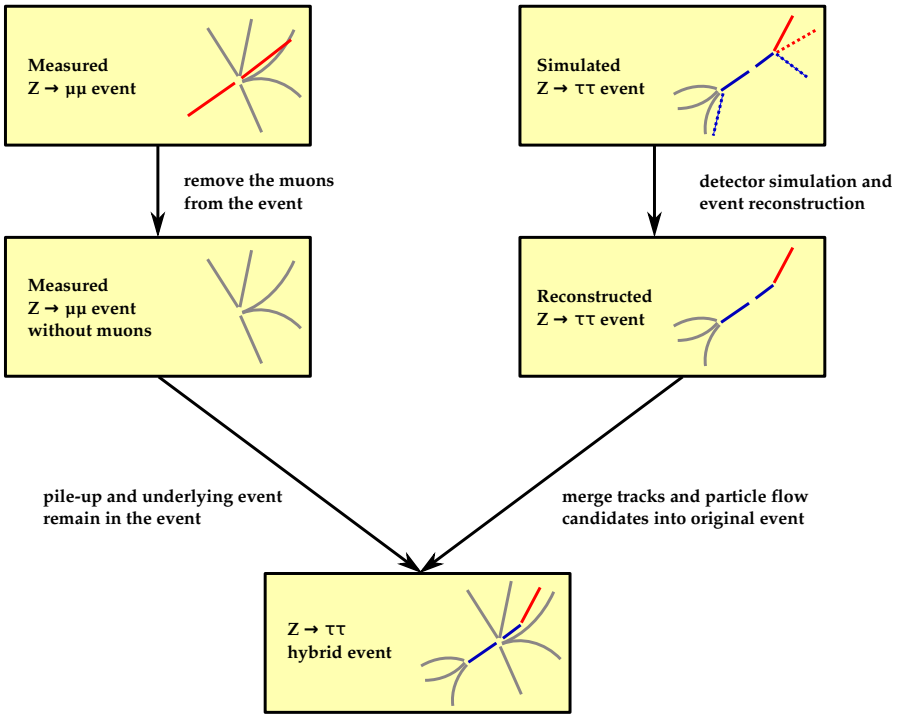

Figure 7.10.: Illustration of the overlay on the level of intermediate objects. Red lines indicate muons, blue lines tau leptons and other particles are depicted in gray (courtesy of Armin Burgmeier).

7.4. Embedding Procedure

The creation of hybrid events is a two-folded procedure. In the first step, the separate $\tau^+\tau^-$ decay has to be simulated based on the reconstruction of a $Z \to \mu^+\mu^-$ candidate. Afterwards the result of the separate event is overlaid with the measured event omitting the muons from the original Z decay.

7.4.1. Generation of Embedded $\tau^+\tau^-$ Events

The generation of embedded $\tau^+\tau^-$ events starts with the reconstruction of $Z \to \mu^+\mu^-$ events as described above. For reasons that will be explained later, the criterion for the invariant mass of the muon pair is loosened to $m_{\mu\mu} > 20$ GeV/c^2.

For the replacement of the muons it is necessary to apply a boost transformation into the rest frame of the Z boson. Only in this reference frame the direction of the two Z decay products is identical for all types of particles as they are back-to-back. This invariance under a rescaling of the four-momenta is exploited in the following modification of the four-momentum vectors. As with the change of the particle identifier the rest mass has to be adjusted as well, it is necessary to rescale the spatial component of the momentum appropriately. Afterwards the inverse of the initial boost transformation returns to the laboratory frame.

During this transformation procedure the decay vertex of the Z boson remained at its reconstructed position of the $\mu\mu$ decay. For the standard production of Monte Carlo events, an artificial smearing is usually applied on the primary vertex of the generated event to simulate the luminous region at the interaction point. This is of course not necessary for artificial events as the reconstructed position of the Z boson decay can be used directly.

The generated event consisting of the two tau leptons and the Z boson as mother particle is then passed to TAUOLA which takes care of the tau decays. Due to the existing mother-daughter relationship, TAUOLA is able to take spin correlations into account. At the same time it is possible to specify a decay mode [143]. This restriction of the phase space allows a conservation of the statistical precision gained by the $Z \to \mu^+\mu^-$ selection. Nevertheless it is necessary to apply a correction factor for other decay modes that mimic the selected decay mode. This will be discussed later in detail.

Furthermore, it is possible to generate only events where the visible tau decay products exceed a certain threshold for the transverse momentum. Such a rejection procedure is reasonable since events with low energetic decay products are very unlikely to pass the selection steps, e. g. muons with a transverse momentum below 9 GeV/c would not even pass the selection process by the single muon trigger algorithm. However it is necessary to keep track of this intentional distortion of the phase space by introducing weights for the events. The event weight is calculated by a repetitive invocation of the TAUOLA library for the given tau pair:

$$w_{\text{event}} = \frac{\#\,(\tau\tau \text{ decays passing the selection})}{\#\,(\text{all tested } \tau\tau \text{ decays})} \,.$$

In the following the embedded data samples have a restricted phase space with a visible transverse momenta sum exceeding 8 GeV/c unless otherwise stated. The decay mode is set to $\tau\tau \to \mu + \tau-$jet.

The production of the separate $Z \to \tau^+\tau^-$ event concludes with a simulation of the detector response for the newly generated decay particles and the subsequent reconstruction of physical objects.

7.4.2. Reconstruction of Embedded Events

With the intermediate objects from the reconstruction of the separate event it is possible to continue with the actual overlay of both events. The collections of particle candidates are simply merged except for the two candidates representing the muons from the original $Z \to \mu^+\mu^-$ decay which are removed. The same procedure is applied on the collection of reconstructed tracks which are used by some of the subsequently executed identification algorithms. Finally, the re-reconstruction of the actual physical objects with the Particle Flow algorithm completes the creation of the hybrid event. More technical details on the embedding process can be found in Appendix B.1.

7.5. Properties of Embedded Events

Samples of simulated $Z \to \mu^+\mu^-$ and $Z \to \tau^+\tau^-$ events allow an evaluation of the embedding method with a large statistical precision. In a first step, the shapes of all relevant kinematic quantities are checked. The absolute normalisation is outlined and tested later.

7.5.1. Kinematic Quantities at Generator Level

Figure 7.11 shows a comparison of the kinematic distributions of the tau leptons and their decay products in simulated $Z \to \tau^+\tau^-$ events and embedded events. It is important to note that the tau leptons in the latter sample correspond to reconstructed muons from a sample of simulated $Z \to \mu^+\mu^-$ events. Consequently the distributions of the artificial taus reflect this reconstruction step with its inefficiencies. The local loss of efficiency at $|\eta| \approx 0.3$ can be attributed to a small gap between two rings of the detector in the barrel region. Small discrepancies in the peak structure of the p_T distribution are caused by the finite momentum resolution of the muon reconstruction.

However the overall agreement of the distributions shows that the embedding procedure is valid up to this step.

7.5.2. Reconstructed Hybrid Events

After the simulation and reconstruction of the partial $Z \to \tau^+\tau^-$ event, the candidates of final physical objects and the tracks are merged. The muons from the

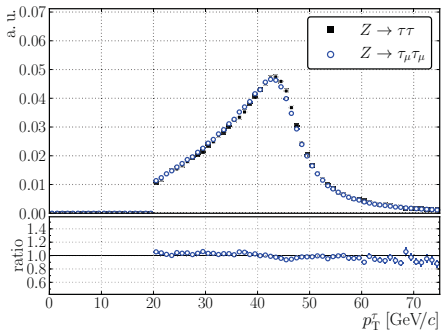

(a) Transverse momentum of the generated taus

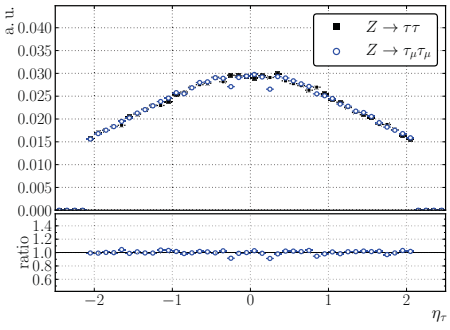

(b) pseudorapidity of the generated taus

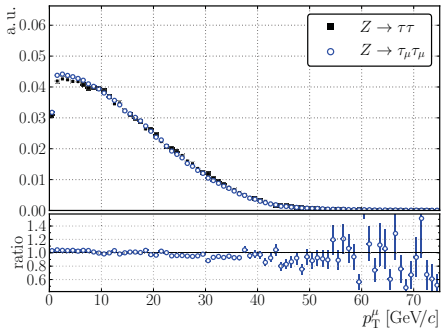

(c) Transverse momentum of the muon

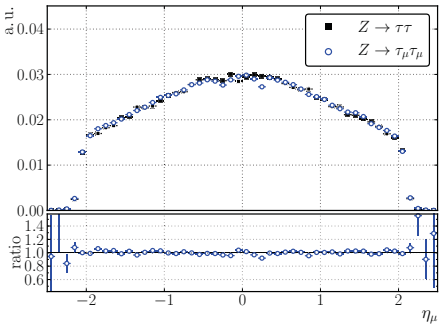

(d) pseudorapidity of the muon

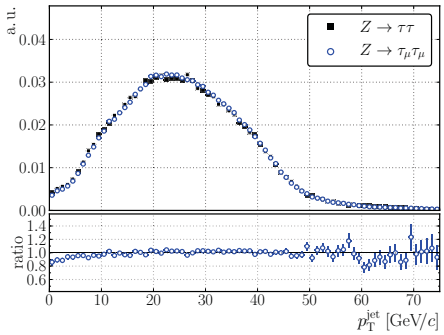

(e) Transverse momentum of the visible part of the hadronically decaying tau lepton

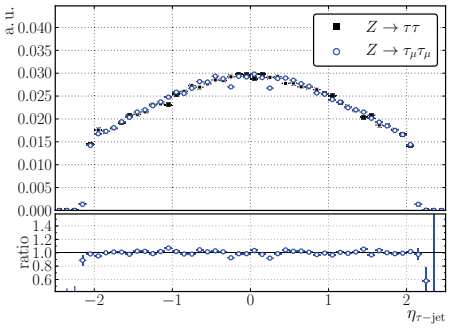

(f) pseudorapidity of the visible part of the hadronically decaying tau lepton

Figure 7.11.: Distributions of the transverse momentum and the pseudorapidity of $\tau\tau \to \mu + \tau-$jet decays at generator level for simulated $Z \to \tau^+\tau^-$ events and embedded events which have been created using simulated $Z \to \mu^+\mu^-$ events. The distributions are scaled to unity, the error bars indicate statistical uncertainties. Only events within the defined acceptance region are used for this plot, i. e. $p_T^\tau > 20$ GeV/c and $|\eta_\tau| < 2.1$.

original $Z \to \mu^+\mu^-$ decay are removed during this step. Following this fusion process, the remaining reconstruction algorithms can be executed.

The information about the position of the beam spot is critical as the position differs in data and the normal simulation setup. Figure 7.12 shows the distribution of the beam spot position in the x-y plane in simulated $Z \to \tau^+\tau^-$ events, in events from the data sample and in embedded events. While the beam spot is displaced on purpose in simulated events, the information is taken correctly from the original data sample for the embedded events.

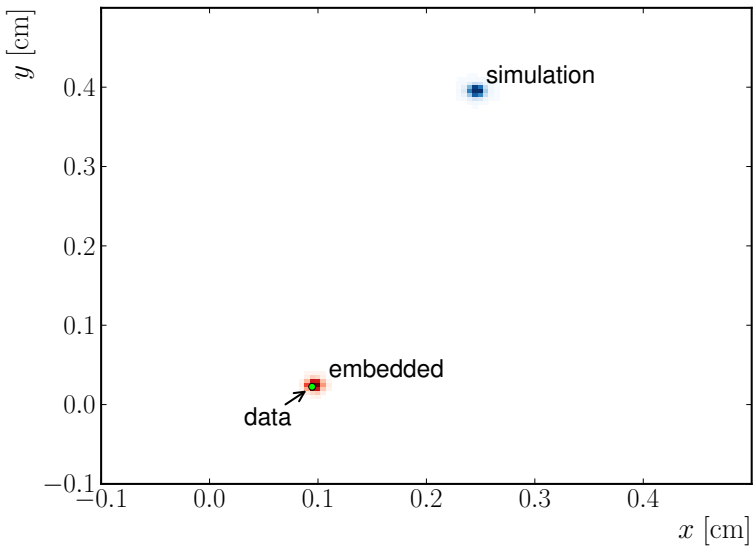

Figure 7.12.: Distributions of the primary vertex position in the x-y plane for simulated, embedded and data events. The small green point indicates the mean position of the primary vertices in data. The figure indicates that the position of the primary vertex is set correctly during the embedding process.

The distributions for the visible mass and the secondary vertex fit mass are shown in Figure 7.13 for simulated and embedded events neglecting the absolute scaling factor. The corresponding plots for the tau decay products can be found in Appendix B.3. A comparison with $\tau\tau \to \mu + \tau-$jet candidates using an absolute normalisation will be presented later as it requires additional scaling factors that will be deduced in the following.

The distributions of both event classes are compatible within the statistical uncertainties. The embedded events are thus able to predict the shapes of the distributions that will later play a crucial role in searches for a light Higgs boson.

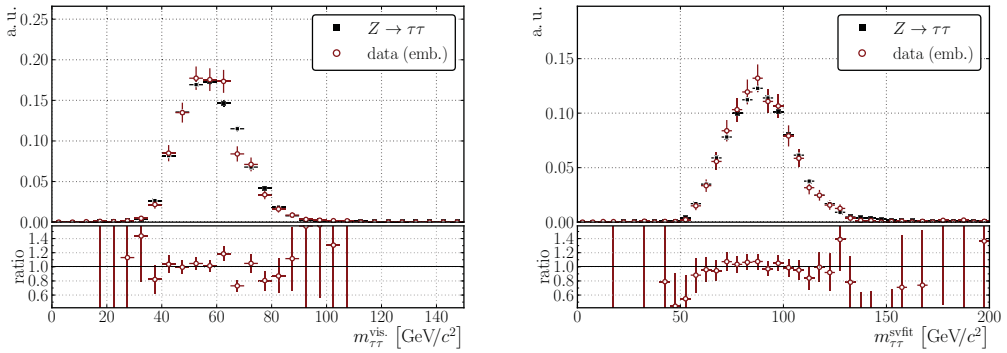

Figure 7.13.: Comparison of the invariant mass distributions for embedded events created from $Z \to \mu^+\mu^-$ candidates in data and simulated $Z \to \tau\tau \to \mu + \tau-$jet events. The distributions are scaled to unity.

7.6. Correction Factors and Systematic Uncertainties

The embedding method with its hybrid events allows for an estimation of various kinematical distributions of $Z \to \tau^+\tau^-$ events by default. For an absolute normalisation it is necessary to calculate all correction factors and keep track of all arising systematic uncertainties.

For the following considerations the acceptance for the selection of $Z \to \mu^+\mu^-$ events is slightly modified with respect to the studies in previous chapters. It is advantageous to repeal the requirement for the invariant di-muon mass. The justification for this relaxation is explained later. Accordingly, the acceptance now reads

$$p_{\text{T}}^{\mu} > 20 \text{ GeV}/c \quad \text{and} \quad |\eta^{\mu}| < 2.1 \, .$$

All correction factors will be given with respect to this definition.

Any initial selection of $Z \to \mu^+\mu^-$ events implicitely imposes a restriction on the phase space of the $\tau^+\tau^-$ events that are produced during the embedding process. The main focus will thus lie on corrections for this restriction.

7.6.1. $Z \to \mu^+\mu^-$ Selection

The previously presented selection of $Z \to \mu^+\mu^-$ candidates includes a cut on the invariant mass of the reconstructed muon pair. It is interesting that a modification of this selection step indirectly alters the kinematic properties of the muons. This effect is pronounced for high and low transverse momenta as presented in Figure 7.14.

A reliable description is especially important for large transverse momenta since the transverse momenta of the tau leptons are on average larger for a potential Higgs

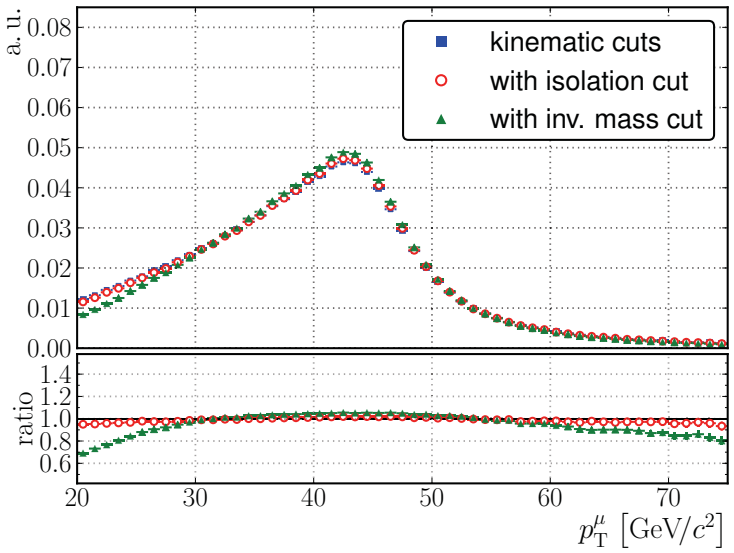

Figure 7.14.: Impact of the $Z \to \mu^+\mu^-$ selection on the shape of the transverse momentum distribution for reconstructed muons. The blue points represent the result for simple kinematic cuts on the two muons, i. e. $p_{\mathrm{T}}^{\mu} > 20$ and $|\eta_{\mu}| < 2.1$. Then, the isolation cut and the invariant mass cut are added successively (red and green). The invariant mass cut introduces significant deviations for both small and large values of the muon transverse momentum. As a consequence, the invariant mass cut is abandoned for the selection of $Z \to \mu^+\mu^-$ candidates for the embedding process. All distributions are scaled to unity.

boson. Any distortion in this regime would lead to an under- or overestimation of the Z boson contribution.

An imperfect description in the low momentum region is less important as the tau leptons result in decay products with – on average – even lower visible transverse momenta. Thus these events in general do not survive the cut on the transverse momentum for the tau decay products and the impact on a Higgs boson search is hence limited.

A broadening of the invariant mass window is a solution for this problem and the next to last row in Table 5.3 shows that the resulting contamination with events from background processes remains below 1% if the mass constraint is abandoned. It is thus sufficient to re-calculate the selection efficiency. Omitting the mass cut, the selection efficiency with respect to the defined acceptance is estimated for the POWHEG Monte Carlo sample with a negligible statistical uncertainty as

$$\epsilon^{\mu\mu}_{\text{acc.}} = 0.8833 \pm 0.0005\ (\text{stat.}) \pm 0.0018\ (\text{syst.})\ .$$

The selection efficiency for the PYTHIA sample reads 0.8851. The difference of 0.0018 between both results is taken as systematic uncertainty.

7.6.2. Muon and τ-jet Energy Scales

The energy scale for hadronically decaying tau leptons is known with an uncertainty of 3%. The corresponding uncertainty on the muon momentum is reported as 1% [109]. By a variation of the momenta of the reconstructed objects and the correlated missing transverse energy it is possible to estimate the impact on the final event yield. A conservative estimation with direct scaling is listed in Table 7.2. The deviation for the final event yield from the nominal value is maximal for an upward scaling of both quantities as the selection includes lower bounds for the transverse momenta. The largest difference of 4.6% is taken as systematic uncertainty due to the energy scale in the following.

Table 7.2.: Impact of the muon momentum and τ-jet energy scale variation on the final event yield. The largest value is taken as systematic uncertainty.

Muon scale	Tau scale	Event yield
+1%	+3%	−4.62%
+1%	−3%	+2.75%
−1%	+3%	−2.61%
−1%	−3%	+4.51%

7.6.3. Influence of Pile-up Events

With the appearance of pile-up events some of the quantities used in the event selection may change. This holds especially for all isolation quantities, the missing

transverse momentum and to some extent also for the τ-jet energy measurement.

Several methods are currently tested to reduce the impact of pile-up events on the final result, e. g. [144]. For the data collected during 2010, pile-up subtraction methods are not mandatory since the number of additional events is low. The available samples of simulated events contain pile-up contributions similar to the actual occurrence in data.

Anyway the clear advantage of the embedding method is its immunity to pile-up events since the overlay procedure preserves any additional activity in the event and passes it to the final hybrid event.

7.6.4. Influence of Photon Radiation

The radiation of photons by the muons in the original $\mathrm{Z} \to \mu^+\mu^-$ decay can have an effect on the embedded events. This concerns the absolute scaling as well as the isolation quantities for the muon and the τ-jet in the embedded event. Additionally, radiated photons lead to lower muon momenta and thus distort the mass spectrum of the reconstructed intermediate Z resonance.

The rejection of a $\mathrm{Z} \to \mu^+\mu^-$ event due to radiated photons inside the isolation cones is covered by the selection efficiency of the $\mathrm{Z} \to \mu^+\mu^-$ selection. This effect has been discussed in Section 5.5.5.

The effect of photon radiation is studied at this point, with reconstructed photons from the original $\mathrm{Z} \to \mu^+\mu^-$ event around the muon in the $\tau\tau \to \mu + \tau-$jet decay. A more general discussion regarding the isolation quantity follows in Section 7.6.7.

To restrict the study to photons connected to the original $\mathrm{Z} \to \mu^+\mu^-$ events, each investigated reconstructed photon is required to match a photon on generator level. The matching is done as usual on the basis of a ΔR criterion:

$$\Delta R\left(\gamma_{\mathrm{gen}}, \gamma_{\mathrm{reco}}\right) < 0.3 \; .$$

Additionally, the transverse energy of the reconstructed photon has to exceed 1 GeV.

Then the sample of the embedded Monte Carlo events is divided into two subsamples based on the existence of such a reconstructed photon from the $\mathrm{Z} \to \mu^+\mu^-$ event in the vicinity of the reconstructed muon in the $\tau\tau \to \mu + \tau-$jet decay:

$$\Delta R\left(\gamma_{\mathrm{reco}}, \mu_{\tau\to\mu}\right) < 0.4 \; .$$

The wider threshold for the distance measure and the energy threshold reflect the settings of the $\tau\tau \to \mu + \tau-$jet selection.

The muon isolation quantity after all other cuts is depicted in Figure 7.15 for events with and for events without photon radiation. With an isolation cut at 0.1 only a fraction of the events with radiated photons survive the isolation cut. The impact on the distribution of the missing transverse energy and the invariant di-tau mass is illustrated in Figure 7.16. The observed differences are compatible with the statistical uncertainties.

The absolute normalisation and the potential necessity of a correction factor for embedded events is discussed in Section 7.6.7.

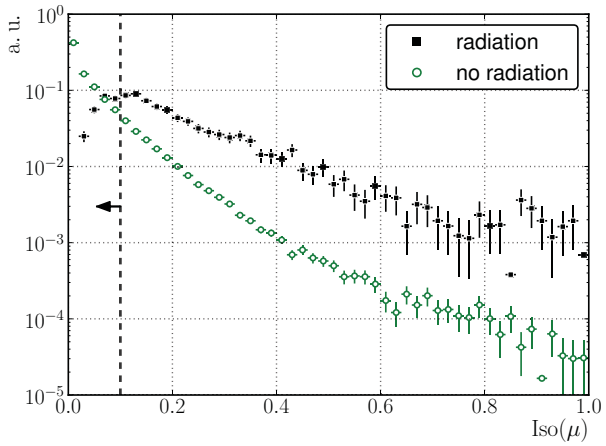

Figure 7.15.: Distribution of the muon isolation quantity in embedded events with and without photon radiation in the original $Z \to \mu^+\mu^-$ events. The definition of radiation that is used here is explained in the text. The threshold of the isolation criterion is indicated by the dashed line, both distributions are scaled to unity.

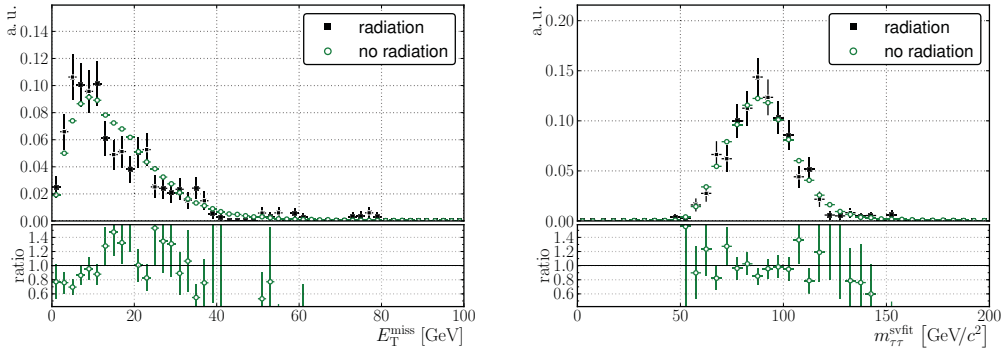

Figure 7.16.: Distributions of the missing transverse energy (left) and the reconstructed invariant di-tau mass (right) after all selection steps. The fraction of events with an additional radiated photon yields about 0.7%. All distributions are scaled to unity.

7.6.5. Effect of $\tau^+\tau^-$ Phase Space Restriction

The selection of the $Z \to \mu^+\mu^-$ candidates obviously imposes a restriction on the phase space for the $Z \to \tau^+\tau^-$ events that are created during the embedding

process. Each generated tau lepton necessarily fulfils

$$p_{\mathrm{T}}^{\tau} > 20 \text{ GeV}/c \quad \text{and} \quad |\eta_\tau| < 2.1 \,. \tag{7.1}$$

Any choice of a specific decay mode additionally restricts the phase space. However, some events with other tau decay modes can fulfil the selection criteria as well. This mimicking of $\tau\tau \to \mu + \tau-$jet events leads to additional contributions and may change the important final distributions. This effect is not covered by the embedding method as long as a specific decay mode is set to preserve the statistical precision.

Kinematical Acceptance

The effect of the phase space restriction can be studied on a sample with simulated $\mathrm{Z} \to \tau^+\tau^-$ events as generator information is required. The whole sample is divided into two classes: the first category consists of $\tau\tau \to \mu + \tau-$jet events where both generated taus fulfil the requirements as defined in Eq. (7.1). The second category includes all other events, i. e. events where at least one generated tau falls outside the kinematical acceptance.

Figure 7.17 presents the comparison of the mass spectra for the reconstructed tau lepton pairs after all selection steps. The agreement is reasonably good although the second category, the non-reachable part of the phase space, shows a lack of statistical precision. Less than 2% of all finally selected $\tau^+\tau^-$ events fall in this category.

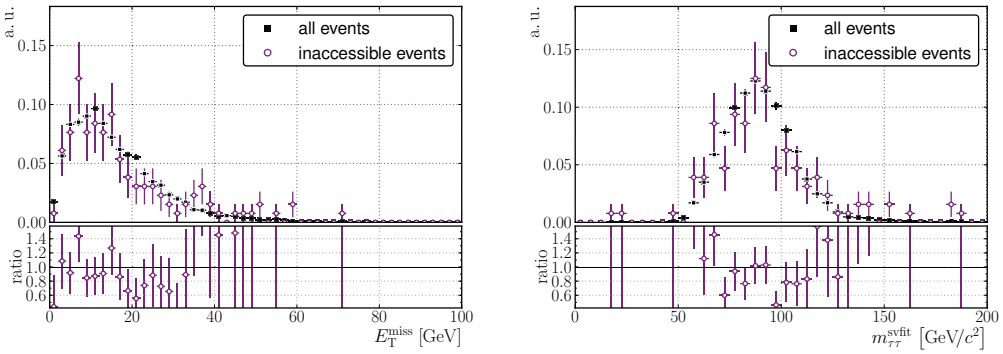

Figure 7.17.: Illustration of the implicit cut on the $\mathrm{Z} \to \tau^+\tau^-$ phase space due to the $\mathrm{Z} \to \mu^+\mu^-$ selection. The shown spectra for the missing transverse energy (left) and the SVfit mass (right) show the corresponding quantities for conventional $\mathrm{Z} \to \tau^+\tau^-$ events. The sample is divided into two classes based on the ability of the tau leptons to fulfil the kinematical acceptance during the $\mathrm{Z} \to \mu^+\mu^-$ selection.

As a consequence of the good agreement in the shape, the effect of the non-reachable phase space can be absorbed into a single scaling factor:

$$k_{\mathrm{corr.}}^{\mathrm{phase\ space}} = 0.9864 \pm 0.0020\,(\mathrm{stat.}) \pm 0.0007\,(\mathrm{syst.}) \,.$$

Here the statistical uncertainty corresponds to the binomial error originating from the classification process. The systematic error is derived from a comparison with a sample of $Z \to \tau^+\tau^-$ events created with PYTHIA which shows a similar behaviour for the studied quantities. Table 7.3 summarizes all event yields and the resulting correction factors.

Table 7.3.: Overview of the correction for events from inaccessible regions of the phase space. This includes other tau decay channels mimicking $\tau\tau \to \mu + \tau-$jet decays and events with tau leptons that do not fulfil the acceptance definition in the $Z \to \mu^+\mu^-$ selection but pass the $\tau^+\tau^-$ selection.

Generator	All Events	Inaccessible	Correction Factor
POWHEG	9645	131	0.9864 ± 0.0020
PYTHIA	9035	129	0.9857 ± 0.0021

Tau Branching Ratio

Beside the required correction it is also necessary to take the tau branching ratio into account to get a correct overall normalisation. The TAUOLA package calculates the branching ratio as

$$\mathrm{BR}\left(\tau\tau \to \mu + \tau-\mathrm{jet}\right) = 0.2265 \; .$$

With the tabulated values from the particle data group [4] the branching ratio can be calculated as

$$\begin{aligned}\mathrm{BR}\left(\tau\tau \to \mu + \tau-\mathrm{jet}\right) &= 2 \cdot \mathrm{BR}\left(\tau \to \mu\right) \cdot \left(1 - \mathrm{BR}\left(\tau \to l\right)\right) \\ &= 0.2250 \; .\end{aligned}$$

The difference between the branching ratios for both approaches is taken as systematic uncertainty resulting in the corresponding correction factor:

$$k_{\mathrm{corr.}}^{\mathrm{BR}(\tau\tau\to\mu+\tau-\mathrm{jet})} = 0.2265 \pm 0.0015 \; .$$

7.6.6. Effect of the Single Muon Trigger

The single muon trigger algorithm exhibits in reality a worse performance than in simulation. This discrepancy has been elucidated in Section 6. The consequences of this imperfect description are more distinct for the selection of $Z \to \tau\tau \to \mu+\tau-$jet events than for the selection of $Z \to \mu^+\mu^-$ events. Since only one muon is present to fire the trigger mechanism, the correction factor is applied directly:

$$k_{\mathrm{corr.}}^{\mu+\tau\text{-jet triggering}} = 0.967 \pm 0.001 \; .$$

In contrast, the correction is smaller for the $Z \to \mu^+\mu^-$ selection as only one out of two muons is required to pass the trigger algorithm successfully. The correction factor is taken directly from Section 5.5.1 and reads:

$$k_{\text{corr.}}^{\mu\mu\ \text{triggering}} = 0.996 \pm 0.002 \ .$$

7.6.7. Effect of the Muon Isolation Cut

The isolation requirement for the muon in the $Z \to \tau\tau \to \mu + \tau-$jet decay is a critical point in artificial events for two reasons. First, the muons in the original $Z \to \mu^+\mu^-$ decay can suffer from photon radiation. For soft photon radiation, the event is likely to survive the selection process and the photon remains in the event. In the resulting $Z \to \tau^+\tau^-$ event it is then still present although it does not belong to the event.

The second reason concerns the isolation in a more general way. Physical processes besides the main hard interaction, e. g. from the underlying event or pile-up events, can induce additional activity in the detector around the direction of the leptons in a Z decay. The isolation requirement during the $Z \to \mu^+\mu^-$ selection might bias the derived artificial $\tau^+\tau^-$ event in the sense that the spatial environment around the tau leptons and their decay products is too clean.

The impact of both effects can be studied by evaluating the efficiency of the isolation criterion for the muon in the $\tau\tau \to \mu + \tau-$jet decay in an embedded sample and a conventional $Z \to \tau^+\tau^-$ sample. To allow a meaningful comparison, it is again important to take the implicit phase space restriction into account. The fraction of $\tau^+\tau^-$ decays mimicking $\tau\tau \to \mu + \tau-$jet is different before and after the application of the isolation cut. The resulting numbers including the correction are summarised in Table 7.4.

The POWHEG generated samples yield a correction factor of

$$k_{\text{corr.}}^{\mu\ \text{isolation}} = 0.9781 \pm 0.0075\ (\text{stat.}) \pm 0.0062\ (\text{syst.}) \ .$$

Here the event yield for the embedded sample is corrected for the inaccessible phase space as explained before. A parallel study on the samples generated with PYTHIA reads $k = 0.9843$ and is used as cross-check. The difference between both correction factors is taken as systematic uncertainty.

7.7. Closure Test for a Sample of Simulated Events

The samples of simulated $Z \to \mu^+\mu^-$ and $Z \to \tau^+\tau^-$ events allow to test the prediction of the absolute number of events with high statistical precision. Unlike for data, every step can be examined and the result should be compatible within the statistical uncertainties.

The embedded sample yields 35929 ± 155 events after all steps of the $\tau\tau \to \mu + \tau-$jet selection. A sample without a preselection based on the transverse

Table 7.4.: Effect of the muon isolation cut in a conventional sample of simulated $Z \to \tau^+\tau^-$ events and in a sample of embedded $Z \to \tau^+\tau^-$ events.

Data Sample	Before Isolation	Iso < 0.1	Efficiency
$Z \to \tau^+\tau^-$ (POWHEG)	11469	9514	0.8295
Emb. $Z \to \tau^+\tau^-$ (POWHEG)	44140	35929	-
Corrected for phase space	44894	36424	0.8113
$Z \to \tau^+\tau^-$ (PYTHIA)	10818	8906	0.8233
Emb. $Z \to \tau^+\tau^-$ (PYTHIA)	46570	37861	-
Corrected for phase space	47394	38410	0.8104

Table 7.5.: Correction factors and their uncertainties for an absolute normalisation of the embedded $Z \to \tau^+\tau^-$ sample. The correction factors in the lower half only apply to the estimation of embedded events in data.

Quantity	Symbol	Value	Uncertainty	
			stat.	syst.
$Z \to \mu^+\mu^-$ Acceptance	$\epsilon_{\text{acc.}}^{\mu\mu}$	0.8833	0.0005	0.0018
Branching Ratio	$k_{\text{corr.}}^{\text{BR}(\tau\tau\to\mu+\tau-\text{jet})}$	0.2265	-	0.0015
Inaccessible Phase Space	$k_{\text{corr.}}^{\text{phase space}}$	0.9864	0.0020	0.0007
Muon Isolation	$k_{\text{corr.}}^{\mu \text{ isolation}}$	0.9781	0.0075	0.0062
Trigger in $Z \to \mu^+\mu^-$ event	$k_{\text{corr.}}^{\mu\mu \text{ trigger}}$	0.996	0.001	0.001
Trigger in $Z \to \tau^+\tau^-$ event	$k_{\text{corr.}}^{\mu+\tau\text{-jet trigger}}$	0.967	0.001	0.001
Tau Jet Energy Scale	$k_{\text{corr.}}^{\tau\text{-jet energy}}$	1	-	0.046

momenta of the visible decay products at generator level results in 35983 events but with a larger statistical uncertainty of ± 190 events.

The event yield has to be corrected for the branching ratio due to the selection of a specific decay mode. An appropriate correction is also necessary since the phase space of the taus in the embedded sample is restricted. The correction for the small differences in the muon isolation cut efficiency complements the corrections and the final scaling factor reads

$$\begin{aligned} k_{\text{scale}}^{\text{MC}} &= \frac{k_{\text{corr.}}^{\text{BR}(\tau\tau\to\mu+\tau-\text{jet})}}{\epsilon_{\text{acc.}}^{\mu\mu} \cdot k_{\text{corr.}}^{\text{phase space}} \cdot k_{\text{corr.}}^{\mu \text{ isolation}}} \\ &= 0.2661 \pm 0.0021 \, . \end{aligned} \tag{7.2}$$

The correction factors are summarised in Table 7.5.

The event yield is then multiplied with the previously determined scaling factor

and the prediction for the final event yield reads:

$$N^{\mathrm{MC}}_{\mathrm{predicted}} = 9563 \pm 41 \text{ (stat.)} .$$

The scaling procedure is also listed in detail in Table 7.6. The $\tau\tau \to \mu + \tau$−jet selection on the conventional sample of $Z \to \tau^+\tau^-$ events, which has the same equivalent integrated luminosity, yields

$$N^{\mathrm{MC}}_{\mathrm{expected}} = 9514 \pm 98 \text{ (stat.)} .$$

The difference between prediction and estimation is below 0.5% and covered by the statistical uncertainties. As a result the estimation of the absolute number of $\tau^+\tau^-$ events works well for simulated events. The distributions of the reconstructed $\tau^+\tau^-$ mass using the collinear approximation and the SVfit mass are depicted in Figure 7.18 using the aforementioned scaling factor for the embedded sample.

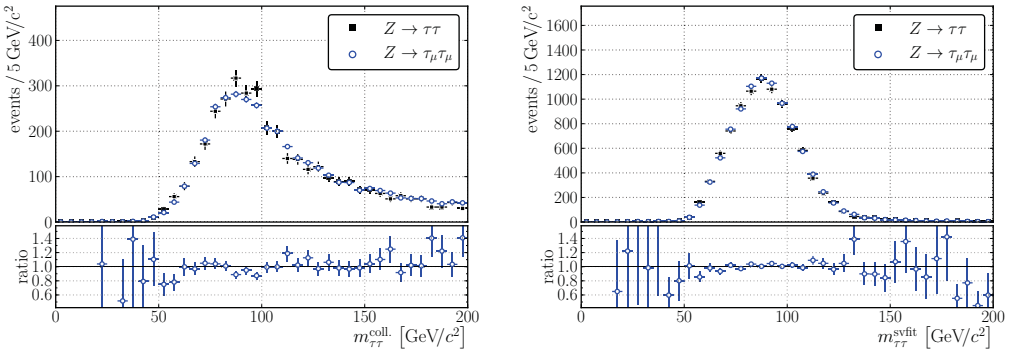

Figure 7.18.: Closure test using a sample of conventional simulated $Z \to \tau^+\tau^-$ events and a sample of embedded events, which is derived from a sample of simulated $Z \to \mu^+\mu^-$ events. The distributions of the reconstructed $\tau^+\tau^-$ mass using the collinear approximation (left) and the SVfit mass (right) are scaled properly for the embedded sample (blue circles) using the result from Eq. (7.2).

7.8. Absolute Normalisation for a Data Sample

The prediction of the absolute number of $Z \to \tau^+\tau^-$ events for a sample consisting of real events requires additional correction factors. These factors cover mainly the imperfect description of the muon High Level Trigger and the uncertainty on the performance of the tau jet energy reconstruction.

The overall scaling factor for a sample of $\tau\tau \to \mu + \tau$−jet events yields

$$\begin{aligned} k^{\mu+\tau\text{-jet, data}}_{\text{scaling}} &= \frac{k^{\mathrm{BR}(\tau\tau\to\mu+\tau-\text{jet})}_{\text{corr.}} \cdot k^{\mu+\tau\text{-jet trigger}}_{\text{corr.}}}{\epsilon^{\mu\mu}_{\text{acc.}} \cdot k^{\text{phase space}}_{\text{corr.}} \cdot k^{\mu\text{ isolation}}_{\text{corr.}} \cdot k^{\mu\mu\text{ trigger}}_{\text{corr.}}} \\ &= 0.2585 \pm 0.0139 \text{ (syst.)} . \end{aligned}$$

Table 7.6.: Overview of the scaling process for the number of expected $Z \to \tau^+\tau^-$ events based on a sample of simulated $Z \to \mu^+\mu^-$ events. The last line presents the number of reconstructed $Z \to \tau\tau \to \mu + \tau-$jet events in a simulated $Z \to \tau^+\tau^-$ sample of equal size.

	Correction	Events	Stat. Uncert.
Selected $Z \to \mu^+\mu^-$ Events		505245	710
Selected $Z \to \tau^+\tau^-$ after Embedding		35983	155
corr. for $Z \to \mu^+\mu^-$ efficiency	$1/\epsilon^{\mu\mu}_{\text{acc.}}$	40676	175
corr. for branching ratio	$k^{\text{BR}(\tau\tau\to\mu+\tau-\text{jet})}_{\text{corr.}}$	9213	40
corr. for inaccessible phase space	$1/k^{\text{phase space}}_{\text{corr.}}$	9340	40
corr. for isolation efficiency	$1/k^{\mu\text{ isolation}}_{\text{corr.}}$	9563	41
Predicted Number of $Z \to \tau^+\tau^-$ Events		9563	41
Number of $Z \to \tau^+\tau^-$ Events		9514	98

The systematic uncertainty is the result of a Gaussian propagation of the individual uncertainties.

The initial sample of $Z \to \mu^+\mu^-$ events contains 14863 events. It should be noted that the event yield is larger than in the dedicated $Z \to \mu^+\mu^-$ study before since the constraint in the invariant di-muon mass has been abandoned.

The reconstructed $Z \to \mu^+\mu^-$ candidates transform into the same amount of hybrid $Z \to \tau\tau \to \mu + \tau-$jet events. In total 959 events of this artificial sample survive all selection steps of the $Z \to \tau^+\tau^-$ analysis. With the scaling factor from above the embedding method thus predicts within the given acceptance:

$$\begin{aligned} N^{\text{pred.}}_{Z\to\tau\tau\to\mu+\tau-\text{jet}} &= k^{\mu+\tau\text{-jet, data}}_{\text{scaling}} \cdot N^{\text{emb.}}_{Z\to\tau\tau\to\mu+\tau-\text{jet}} \\ &= 248 \pm 13\ (\text{syst.}) \pm 8\ (\text{stat.})\ . \end{aligned}$$

It is notable that the relative statistical uncertainty is again determined by the number of events before the scaling. The scaling process is presented in detail in Table 7.7.

The selection of $\tau\tau \to \mu + \tau-$jet candidates on data unavoidably includes contributions from background processes. For a comparison with data it is thus necessary to estimate these additions. The results for the studied background channels are scaled according to their individual production cross sections and the integrated luminosity of the data sample. This calculation yields 84 events with an uncertainty of 3 due to the uncertainty on the luminosity measurements and a statistical uncertainty of 3 events. Any other systematic uncertainties on the background contributions are neglected at this point for the sake of simplicity.

The total number of expected $\tau\tau \to \mu + \tau-$jet events reads in consequence of this additional contribution:

$$N^{\text{exp.}}_{\tau\tau\to\mu+\tau-\text{jet}} = 332 \pm 13\ (\text{syst.}) \pm 9\ (\text{stat.}) \pm 3\ (\text{lumi.})\ .$$

Table 7.7.: Overview of the scaling process for the number of expected $Z \to \tau^+\tau^-$ events based on the data sample recorded in 2010. The last line presents the number of reconstructed $Z \to \tau\tau \to \mu + \tau-$jet events in the data sample. The number of predicted background events is solely based on simulated samples and is not associated with the embedding process.

	Correction	Events	Stat. Uncert.
Selected $Z \to \mu^+\mu^-$ Events		15270	124
Selected $Z \to \tau^+\tau^-$ after Embedding		959	31
corr. for $Z \to \mu^+\mu^-$ efficiency	$1/\epsilon^{\mu\mu}_{\text{acc.}}$	1086	35
corr. for branching ratio	$k^{\text{BR}(\tau\tau\to\mu+\tau-\text{jet})}_{\text{corr.}}$	246	8
corr. for inaccessible phase space	$1/k^{\text{phase space}}_{\text{corr.}}$	249	8
corr. for isolation efficiency	$1/k^{\mu\text{ isolation}}_{\text{corr.}}$	255	8
corr. for trigger in $Z \to \mu^+\mu^-$	$1/k^{\mu\mu\text{ trigger}}_{\text{corr.}}$	256	8
corr. for trigger in $Z \to \tau^+\tau^-$	$k^{\mu+\tau\text{-jet trigger}}_{\text{corr.}}$	248	8
Predicted Number of $Z \to \tau^+\tau^-$ Events		248	8
Predicted Number of Bkg. Events		84	3
Total Number of Predicted Events		332	9
Number of Observed $\tau^+\tau^-$ Events		357	19

The application of the selection procedure on the data sample from 2010 yields in total 357 ± 19 (stat.) events with $\tau\tau \to \mu + \tau-$jet candidates. So the prediction differs by 8% from the actual result. This difference is currently covered by the statistical and systematic uncertainties. Only a larger data sample will allow a decision whether this is a systematic deviation or just a statistical fluctuation. The final di-tau invariant mass distributions are also depicted in Figure 7.19.

7.9. Conclusion

The test of the embedding method on a sample of simulated events proved that the procedure is able to estimate the shape of all relevant quantities reliably. It could be further shown that an estimation of the absolute number of events is possible. The successful application of the method on data recorded in 2010 complements the picture. The estimation based on embedded events agrees with the direct reconstruction of $Z \to \tau^+\tau^-$ events within the given uncertainties which are dominated by the statistical uncertainty.

These results are the basis for more detailed study on the data sample from 2011 with a much larger statistical precision. During the year 2011, samples of embedded events will also become important for the first Higgs boson searches.

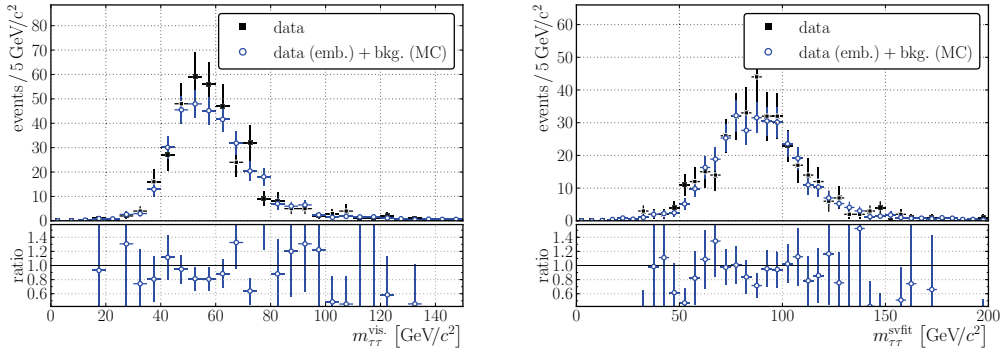

Figure 7.19.: Comparison of the mass spectra of reconstructed $\tau\tau \to \mu + \tau-$jet candidates using the visible mass definition (left) and the SVfit method (right) in a sample of embedded events and reconstructed $\tau\tau \to \mu + \tau-$jet candidates in the 2010 data sample. As the embedded sample covers only $Z \to \tau^+\tau^-$ events, it is necessary to add background contributions as well. They are scaled according to their individual production cross sections and the integrated luminosity.

8. Conclusion & Outlook

The start of proton-proton collisions at a centre-of-mass energy of $\sqrt{s} = 7$ TeV at the Large Hadron Collider opened a new, yet unprecedented range of energy for high energy physics. Analyses using the data sample recorded in 2010 are focussed on the commissioning of the detector and the re-discovery of the Standard Model.

The Z boson is one of the particles within the Standard Model which allows a deeper understanding of the detector. The reconstruction through decays into two muons profits from the ability of the CMS experiment to reconstruct muons precisely. The presented study on the $\mathrm{Z} \to \mu^+\mu^-$ decay in this work shows a remarkably good agreement between reconstructed candidates in data and simulated $\mathrm{Z} \to \mu^+\mu^-$ events. The additionally performed measurement of the Z production cross section yields

$$\sigma_Z \times \mathrm{BR}\left(\mathrm{Z} \to \mu^+\mu^-\right) = 983 \pm 9\,(\mathrm{stat.}) \pm 40\,(\mathrm{exp.}) \pm 36\,(\mathrm{theo.})\ \mathrm{pb}\ .$$

This result is in good agreement with the theoretical prediction,

$$\sigma_Z^{\mathrm{theo}} \times \mathrm{BR}\left(\mathrm{Z} \to \mu^+\mu^-\right) = 990 \pm 12\ \mathrm{pb}\ ,$$

and it is further in good agreement with the official result of the CMS collaboration,

$$\sigma_Z^{\mathrm{CMS}} \times \mathrm{BR}\left(\mathrm{Z} \to \mu^+\mu^-\right) = 968 \pm 8\,(\mathrm{stat.}) \pm 39\,(\mathrm{exp.}) \pm 18\,(\mathrm{theo.})\ \mathrm{pb}\ .$$

Within the work presented here, significant contributions to the official result were made and additional systematic studies have been performed.

A detailed study of the muon High Level Trigger algorithms revealed an unexpected inefficiency with respect to the expectation from simulation. This study also showed that the isolation criteria were not implemented correctly until late 2010. The correction factors were deduced in a data-driven way and applied within the muon related studies throughout this thesis.

The decay of a Z boson into two taus is a very important process for Higgs boson discovery searches where this process acts as the major background contribution. This work presents a new data-driven method for the estimation of all relevant kinematic quantities in $\mathrm{Z} \to \tau^+\tau^-$ events derived from reconstructed $\mathrm{Z} \to \mu^+\mu^-$ events from data. Simulated $\tau^+\tau^-$ decays of Z bosons are embedded in measured $\mathrm{Z} \to \mu^+\mu^-$ events, which are cleaned of the muons. This results in a realistic description of $\mathrm{Z} \to \tau^+\tau^-$ events by such hybrid events. This approach reduces systematic uncertainties arising from modelling of the underlying event and pile-up contributions as both effects are taken from the measured event and do not require any simulation.

It was demonstrated that the embedding procedure results in a realistic description of $Z \to \tau^+\tau^-$ events. The shapes of the relevant distributions are robust with respect to the studied uncertainties. Therefore they can be used as a template distribution for fits in a Higgs boson search or a Z boson production cross section measurement. The necessary tools have been implemented within the CMS software framework and are available for general use within the collaboration. This thesis further presented an absolute estimation of the number of $Z \to \tau^+\tau^-$ events predicted from $Z \to \mu^+\mu^-$ events. The application on both simulated samples and the data sample recorded in 2010 yielded a good agreement with directly measured $Z \to \tau^+\tau^-$ candidates within the estimated uncertainties.

Outlook

The data taking campaign in 2011 will allow to perform first searches for Higgs bosons. Indirect precision measurements at previous collider experiments favour a Higgs boson mass below 190 GeV/c^2, the Tevatron experiments could exclude a Higgs boson mass around 165 GeV/c^2. Studies in the channels $H \to \gamma\gamma$, $H \to b\bar{b}$ and most notably $H \to \tau\tau$ will be performed to surpass the existing exclusion limits.

The study of the latter decay channel will benefit from the results presented in this work in multiple ways. First and foremost the tau embedding provides a reliable data-driven estimation of the background contribution arising from $Z \to \tau^+\tau^-$ decays. This leads to a smaller uncertainty on the expected significance compared to an estimation solely based on simulation.

According to the current plans of the LHC operation group and the status of the Higgs boson studies within the CMS collaboration, the exclusion limits set by the Tevatron experiments for the Standard Model Higgs boson mass will be extended in 2011.

A. Supplement to $Z \rightarrow \mu^+\mu^-$

A.1. Comparison of Event Generators for $Z \rightarrow \mu^+\mu^-$

In addition to the evaluation of the uncertainties on the final event yield due the dedicated uncertainties in the theoretical calculation, it is also possible to compare the results of independent Monte Carlo generators.

The official production campaign also provides a sample of $Z \rightarrow \mu^+\mu^-$ events procuded with MC@NLO which uses HERWIG for the parton shower process. MC@NLO has its own implementation of the hard process at next-to-leading order precision, the same holds for HERWIG's parton shower algorithm. The comparison of POWHEG and MC@NLO is thus orthogonal in every sense of the production. The results for the event yield after all cuts are shown in Table A.1 and differ by 2.8%.

Table A.1.: Results for different generators. The PYTHIA sample is calculated only at leading order precision and thus shown here only for illustrative purposes.

	PYTHIA	POWHEG	MC@NLO
before all cuts	2 235 697	1 998 931	2 224 564
after all cuts	434 882	411 853	443 616
efficiency	0.1945	0.2060	0.2003

A.2. Additional Information

Simulated Samples

The samples of simulated events that are used throughout this thesis have been produced during the official production campaign of the CMS collaboration in Fall 2010 with the 3.8 branch of the CMSSW framework. The precision of the underlying detector alignment reflects the precision of the actual alignment. The most important samples, including all major samples of this analysis, have been produced with pile-up contribution. The number of additional events follows the amount of pile-up events that has been observed in 2010. A list of the used data samples is shown in Table A.2.

Table A.2.: Main data sets and Monte Carlo samples for both signal and background processes used in the $Z \to \mu^+\mu^-$ analysis. The cross sections σ_{prod} for the electroweak processes are calculated at next-to-next-to-leading order, the cross section of $t\bar{t}$ at next-to-leading and the QCD cross section is given at leading order. All samples have been created during the official production campaign in fall 2010.

dataset	events	σ_{prod} [pb]	$\mathcal{L}$ [pb^{-1}]
muon dataset (2010A)	51 860 222	–	3.1
muon dataset (2010B)	33 470 281	–	32.9
$Z \to \mu^+\mu^-$ (POWHEG)	1 998 931	1 702	1 199.8
$Z \to \mu^+\mu^-$ (PYTHIA)	2 235 697	1 702	1 313.6
$Z \to \tau^+\tau^-$ (POWHEG)	1 993 603	1 702	1 196.6
$Z \to \tau^+\tau^-$ (PYTHIA)	2 011 186	1 702	1 182.7
$W^+ \to \mu^+\nu$ (POWHEG)	1 991 320	6 152	323.7
$W^- \to \mu^-\nu$ (POWHEG)	1 996 548	4 286	465.8
$W^\pm \to \mu^\pm\nu$ (PYTHIA)	5 283 540	9 779	540.3
$t\bar{t}$ + jets (POWHEG)	999 909	65.83	15 189.3
$t\bar{t}$ + jets (PYTHIA)	1 095 950	65.83	16 648.2
WW (PYTHIA)	2 061 760	27.8	73 634.3
WZ (PYTHIA)	2 194 752	10.5	209 024.0
ZZ (PYTHIA)	2 113 368	4.3	491 480.9
μ-enriched QCD (PYTHIA)	29 504 866	84 679	370.3
$\hat{p}_{\text{T}} = 20$ GeV/c, $p_{\text{T}}^{\mu} > 15$ GeV/c			

Additional Plots

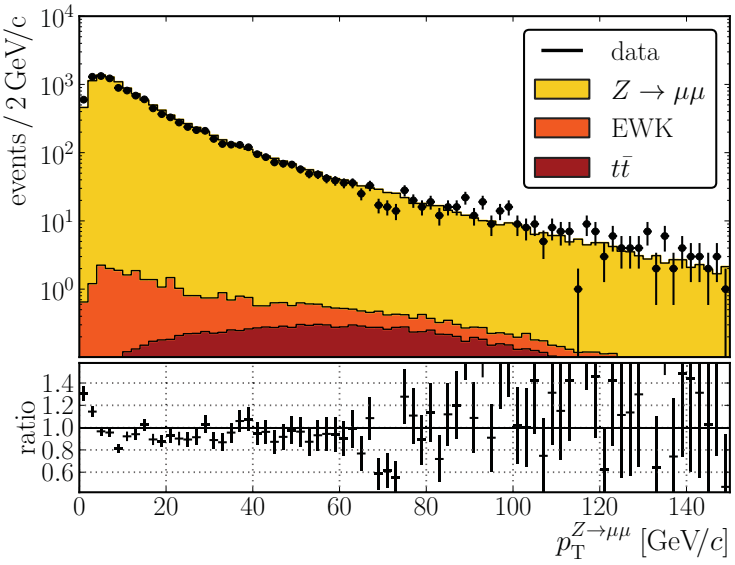

Figure A.1.: Distribution of the Z boson transverse momentum in $\mathrm{Z} \to \mu^+\mu^-$ events.

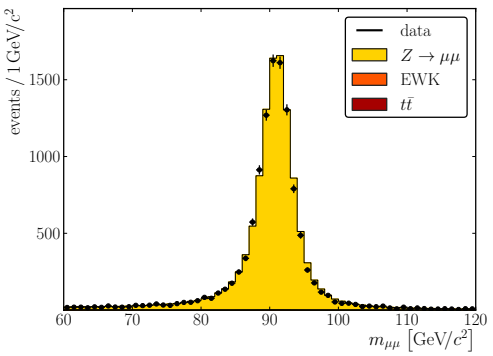

(a) invariant mass: linear scale

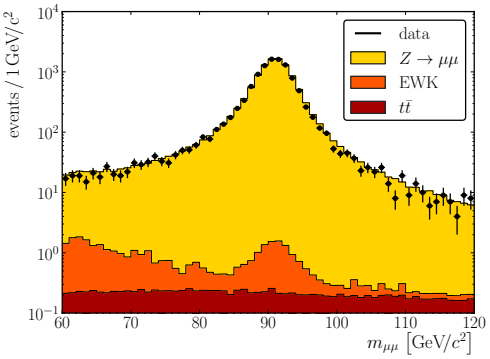

(b) invariant mass: logarithmic scale

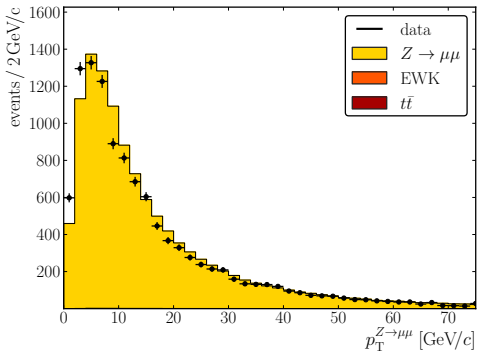

(c) transverse momentum: linear scale

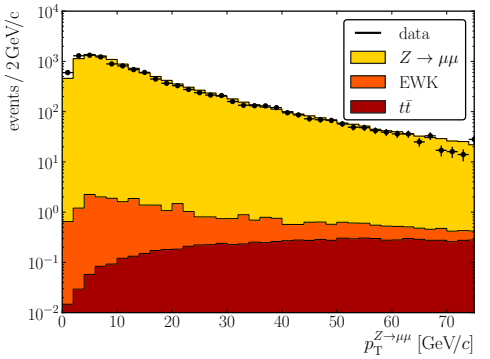

(d) transverse momentum: logarithmic scale

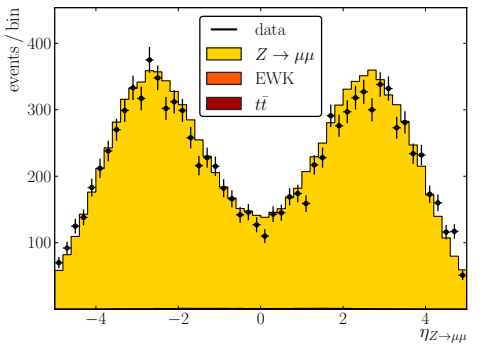

(e) rapidity: linear scale

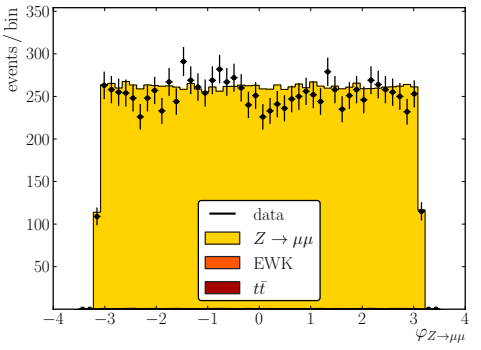

(f) azimuthal angle: linear scale

Figure A.2.: Various distributions for $Z \to \mu^+\mu^-$ candidates after all selection steps.

Configuration file for DYNNLO

The following exemplary code fragment has been used for the cross section calculation with DYNNLO 1.1 [145]. In contrast to other programs, the required restriction of the phase space for the outgoing leptons of the Z boson decay are configured inside the source code before compiling the program. Hence, the corresponding values do not appear in the following configuration fragment.

```
7d3               ! sroot
1 1               ! ih1, ih2
3                 ! nproc
80.339d0 80.339d0  ! mur, muf
2                 ! order
'tota'            ! part
.false.           ! zerowidth
20d0 7d3          ! mwmin, mwmax
15 800000         ! itmx1, ncall1
30 800000         ! itmx2, ncall2
42                ! random seed
92 0              ! set, member (native PDFs)
'MSTW2008nnlo68cl.LHgrid' 0  ! set, member (LHAPDFs)
'outfile'            ! runstring
```

Configuration file for FEWZ

The following exemplary configuration fragment has been used for the cross section calculation with FEWZ 2.0.1.a3 [146]. For unknown reasons, FEWZ ignored the option for a variation of α_s (second-to-last parameter).

```
========= Which sector to run, if only one =====
'NNLO sector                    = ' 1
=============================================
'CMS collision energy (GeV)     = ' 7000d0
=============================================
'Factorization scale  (GeV)     = ' 80.339d0
'Renormalization scale  (GeV)   = ' 80.339d0
=============================================
'Z production (pp=1,ppbar=2)    = ' 1
=============================================
'Alpha QED                      = ' 0.0078125d0
'Fermi constant (1/GeV^2)       = ' 0.0000116637d0
=============================================
'W mass (GeV)                   = ' 80.339d0
'Z mass (GeV)                   = ' 91.1876d0
'Z width (GeV)                  = ' 2.4952d0
'W width (GeV)                  = ' 2.141d0
'Z->ll partial width            = ' 0.083988d0
'W->lv partial width            = ' 0.2263d0
'sin^2(theta)                   = ' 0.22255d0
'up quark charge                = ' 0.6666667d0
'down quark charge              = ' -0.3333333d0
'lepton chage                   = ' -1d0
'up quark vector coupling       = ' 0.4091d0
'down quark vector coupling     = ' -0.7045d0
'lepton vector coupling         = ' -0.11360d0
'up quark axial coupling        = ' -1d0
'down quark axial coupling      = ' 1d0
'lepton axial coupling          = ' 1d0
```

```
==========================================
Vegas Parameters
'Relative accuracy (in %)           = ' 1 ! 1
'Absolute accuracy                  = ' 1d-2 ! 1d-2
'Number of calls per iteration      = ' 10000
'Number of increase calls per iter. = ' 10000
'Maximum number of evaluations      = ' 10000000
'Random number seed for Vegas       = ' 26
==========================================
'Perturb. Order (0=LO, 1=NLO, 2=NNLO) = ' 1
'Z pole focus (1=Yes, 0=No) = ' 0
'Lower M limit (for non-Zpole)  = '  50.0d0
'Upper M limit (for non-Zpole)  = ' 110.0d0
'Turn off photon (1=Yes, 0=No)  = ' 0
==========================================
'Lepton-pair invariant mass minimum = ' 60d0
'Lepton-pair invariant mass maximum = ' 120d0
'Z pT minimum                       = ' 0d0
'Z pT maximum                       = ' 1000d0
'Z rapidity minimum                 = ' -20d0
'Z rapidity maximum                 = ' 20d0
'Lepton pT minimum                  = ' 20d0
'Lepton pT maximum                  = ' 1000d0
'Anti-lepton pT minimum             = ' 20d0
'Anti-lepton pT maximum             = ' 1000d0
'pT min for softer lepton           = ' 20d0
'pT max for softer lepton           = ' 1000d0
'pT min for harder lepton           = ' 20d0
'pT max for harder lepton           = ' 1000d0
Taking absolute value of lepton pseudorapidity?
'(yes = 1, no = 0)      = ' 1
'Lepton pseudorapidity minimum      = ' 0d0
'Lepton pseudorapidity maximum      = ' 2.1d0
Taking absolute value of anti-lepton pseudorapidity?
'(yes = 1, no = 0)      = ' 1
'Anti-lepton pseudorapidity minimum = ' 0d0
'Anti-lepton pseudorapidity maximum = ' 2.1d0
Taking absolute value of soft lepton pseudorapidity?
'(yes = 1, no = 0)                  = ' 1
'Softer lepton pseudorapidity min   = ' 0d0
'Softer Lepton pseudorapidity max   = ' 2.1d0
Taking absolute value of hard lepton pseudorapidity?
'(yes = 1, no = 0)                  = ' 1
'Harder lepton pseudorapidity min   = ' 0d0
'Harder Lepton pseudorapidity max   = ' 2.1d0
Jet Cuts-----------------------------------
'Minimum pT for Observable Jets     = ' 20d0
'Minimum Number of Jets     = ' 0
'Maximum Number of Jets     = ' 2
'Jet 1 pT minimum                   = ' 0d0
'Jet 1 pT maximum                   = ' 1000d0
'Jet 2 pT minimum                   = ' 0d0
'Jet 2 pT maximum                   = ' 1000d0
Taking absolute value of Jet 1 pseudorapidity?
'(yes = 1, no = 0)                  = ' 1
'Jet 1 pseudorapidity minimum       = ' 0d0
'Jet 1 pseudorapidity maximum       = ' 4.5d0
Taking absolute value of Jet 2 pseudorapidity?
'(yes = 1, no = 0)                  = ' 1
'Jet 2 pseudorapidity minimum       = ' 0d0
'Jet 2 pseudorapidity maximum       = ' 4.5d0
Jet Algorithm & Cone Size ('ktal'=kT algorithm, 'aktal'=anti-kT algorithm, 'cone'=cone)
```

```
'ktal, aktal or cone     = ' ktal
'Jet algorithm cone size (deltaR)   = ' 0.4d0
'DeltaR separation for cone algo    = ' 1.3
ISOLATION CUTS------------------------------
'Lep-Anti-lep deltaR minimum        = ' 0.0d0
'Lep-Anti-lep deltaPhi min     = ' 0.0d0
'Lep-Anti-lep deltaPhi max     = ' 40.0d0
'Lep-Jet deltaR minimum             = ' 0.0d0
============================================
Cut on Z rapidity for well-defined Collins-Soper Angles at pp Collider
'Z rapidity cutoff for CS frame     = ' 0.0d0
============================================
(See manual for complete listing)
'PDF set =                        ' 'MSTW2008NLO'
(Active for MSTW2008 only; 0: alphaS best fit, 1: alphas-1sigma, 2: alphas-1/2sigma)
(3: alphas+1/2sigma, 4: alphas+1sigma)
'Which alphaS                       = ' 0
(Active for MSTW2008 only; 0: 90 CL for PDFs+alphas, 1: 68 CL)
'PDF+alphas confidence level        = ' 1
============================================
```

B. Supplement to $Z \rightarrow \tau^+\tau^-$

B.1. Description of the Embedding Process

The creation of embedded events on the level of Particle Flow objects is two-folded. In a first step, events with $Z \rightarrow \mu^+\mu^-$ canditates are selected according to the baseline selection of the vector boson task force. The corresponding modules for the candidate selection are provided in the `TauAnalysis/MCEmbeddingtools` package in CMSSW and produce a di-muon candidates.

These candidates are then taken as input for the replacement which is done by the `MCParticleReplacer` module. The user can choose between three different transformation mode steered by the option `transformationMode`:

- The transformation into a tau lepton pair is the default transformation mode.
- A dummy transformation which simply copies the muons. That procedure results in an unchanged pair of muons and can be used for cross-checks.
- The Z boson can also be transformed into a W. The particle is corrected for the different mass and the different decay width. A detailed description can be found in [147].

In the following this description will be resticted to the transformation into a tau lepton pair, more information on the other available modes can be found in the comments in the source code [148].

To maintain the kinematic properties of the Z boson decay during the transformation process, it is necessary to boost the muons in the rest frame of the Z boson. In this reference system the muons are back to back and their momenta can be easily scaled to take the different masses of muons and tau leptons into account while preserving their direction. A transformation with the inverse lorentz boost yields a $Z \rightarrow \tau^+\tau^-$ event that is stored in the HEPMC format which is commonly used for event generation. The decay vertex position corresponds to the original decay vertex of the Z boson candidate.

It is notable that this newly generated event yet consists only of the Z boson as mother particle and the two taus as daughter particles. The tau lepton decays are performed by the TAUOLA package which takes polarization effects of the tau leptons and their decay products into account. The user can configure TAUOLA in the same way as for a normal event generation, first and foremost the decay modes. A list of the possible decay modes can be found in [143].

Additionally, the user can define a minimum transverse momentum for the sum of the visible tau decay products and the transformation module will create an

event that fulfills this restriction. The hereby introduced weight of the event is stored as a `double` variable inside the CMSSW event and can be processed later by other modules. The branching fraction for the tau decay is not included in the event weight and has to be applied separately.

During the following simulation, slight modifications to the standard configuration are needed but these are all included in the provided config files:

- The commonly applied vertex smearing is switched off as the decay vertex is taken from the $Z \to \mu^+\mu^-$ decay and a smearing as for Monte Carlo events is not necessary.

- The $\tau\tau$ event itself is simulated using the startup detector conditions to match reality as close as possible. However, the beam spot position is different for data and Monte Carlo, so this particular information has to be overridden with the beam spot information that has been determined during the data taking process.

The di-muon candidate produced at the beginning is also used to identify the muon tracks in the track collection and the correpsonding objects in the Particle Flow candidate collections. They are removed and the remainders of the collections are merged with the collections from the separate $Z \to \tau^+\tau^-$ simulation. Subsequently the Particle Flow algorithms create all Particle Flow objects, e. g. taus, jets and the missing transverse energy. It is noteworthy that – for the purpose of later cross-checks – basically all products within the event are kept.

Analyses need only small modifications to read the newly generated products if at all. Without the explicit specification of the *process name* in *input tags* of analysing modules, CMSSW will always choose the latest produced object collection automatically which is in this case the correct one. If the trigger information is evaluated and checked for consistency, the user should keep in mind that `isRealData()` still returns *true* but the HLT process name to be used is not anymore `HLT`.

B.2. Mass Reconstruction with the Collinear Approximation

Restricted to the reconstructed visible momenta and the missing transverse energy, it is necessary to approximate the fraction of the momenta carried away by the neutrinos. For the decay of a high energetic tau lepton, both the sum of the neutrinos and the created visible decay producs can be assumed to be close to the original direction of the tau lepton in the three-vector space. This approximation is illustrated in Figure B.1. Hence, the missing energy can be projected onto the direction of the visible decay products to finally obtain the unavailable z-component of the missing energy.

Using the collinear approximation, it is sufficient to determine the visible fraction x_i of the tau transverse momentum as the fraction of the transverse momentum of

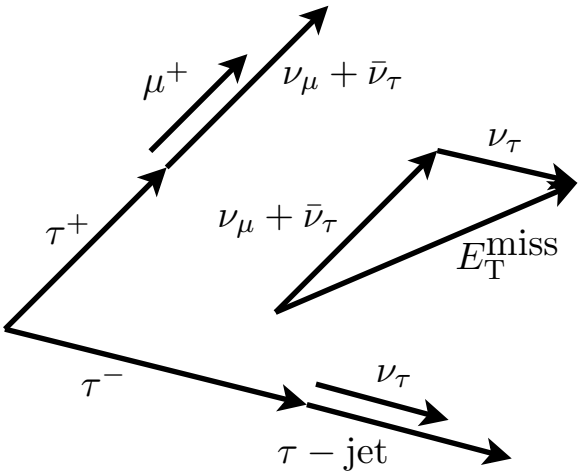

Figure B.1.: In the collinear approximation the directions of the decay products of the two taus are assumed to be close to the original tau directions. In this approximation, the missing transverse energy is equal to the sum of the neutrinos' momenta

the visible decay product $p_{\mathrm{T}}^{\mathrm{vis}_i}$ and the yet unknown tau transverse momentum $p_{\mathrm{T}}^{\tau_i}$:

$$x_i = \frac{p_{\mathrm{T}}^{\mathrm{vis}_i}}{p_{\mathrm{T}}^{\tau_i}}, \quad i = 1, 2 \tag{B.1}$$

Since the transverse momentum is conserved the following equation holds

$$\begin{aligned} \vec{p}_{\mathrm{T}}^{\,\tau_1} + \vec{p}_{\mathrm{T}}^{\,\tau_2} &= \vec{p}_{\mathrm{T}}^{\,\mathrm{vis}_1} + \vec{p}_{\mathrm{T}}^{\,\mathrm{vis}_2} + \vec{p}_{\mathrm{T}}^{\,\mathrm{miss}} \\ &= \frac{\vec{p}_{\mathrm{T}}^{\,\mathrm{vis}_1}}{x_1} + \frac{\vec{p}_{\mathrm{T}}^{\,\mathrm{vis}_2}}{x_2}, \end{aligned}$$

which can be solved for $\vec{p}_{\mathrm{T}}^{\,\mathrm{miss}}$:

$$\vec{p}_{\mathrm{T}}^{\,\mathrm{miss}} = \left(\frac{1}{x_1} - 1\right) \vec{p}_{\mathrm{T}}^{\,\mathrm{vis}_1} + \left(\frac{1}{x_2} - 1\right) \vec{p}_{\mathrm{T}}^{\,\mathrm{vis}_2}$$

This expression is equivalent to a linear system of equations. By solving it the visible fractions x_i can be written as

$$\begin{aligned} x_1 &= \frac{p_x^{\mathrm{vis}_1} p_y^{\mathrm{vis}_2} - p_y^{\mathrm{vis}_1} p_x^{\mathrm{vis}_2}}{p_y^{\mathrm{vis}_2} p_{\mathrm{T},x}^{\mathrm{miss}} - p_x^{\mathrm{vis}_2} p_{\mathrm{T},y}^{\mathrm{miss}} + p_x^{\mathrm{vis}_1} p_y^{\mathrm{vis}_2} - p_x^{\mathrm{vis}_2} p_y^{\mathrm{vis}_1}} \\ x_2 &= \frac{p_x^{\mathrm{vis}_1} p_y^{\mathrm{vis}_2} - p_y^{\mathrm{vis}_1} p_x^{\mathrm{vis}_2}}{p_x^{\mathrm{vis}_1} p_{\mathrm{T},y}^{\mathrm{miss}} - p_y^{\mathrm{vis}_1} p_{\mathrm{T},x}^{\mathrm{miss}} + p_x^{\mathrm{vis}_1} p_y^{\mathrm{vis}_2} - p_x^{\mathrm{vis}_2} p_y^{\mathrm{vis}_1}} \end{aligned}$$

For a physical solution the values x_i must yield a value between 0 and 1. After all, the invariant $\tau\tau$ mass can be calculated under the assumption of massless neutrinos

as

$$m_{\tau\tau} = \frac{m_{ll}}{\sqrt{x_1 x_2}}$$

The collinear approximation was studied with generated particles in PYTHIA $\gamma^*/Z \to \mu\mu$ events. Here, the missing energy is calculated as the vectorial sum of the neutrinos momenta. Figure B.2(a) shows the fractions $x_{1,2}$ in a two-dimensional plot: All entries in the plot outside the marked rectangle $[0,1;0,1]$ represent a reconstruction where the event does not fulfill the collinear assumption. In such a case, the event is rejected.

The collinear approximation causes a broadening of the invariant di-tau mass distribution as figure B.2(b) shows. It compares the distribution of the invariant mass of the generated Drell-Yan events and the reconstructed invariant mass. It is important that this broadening is inherent to the reconstruction with the collinear approximation. The resolution of the Z mass resonance is further affected by the limited resolution of the detector and impreciseness of the reconstruction of the physical objects.

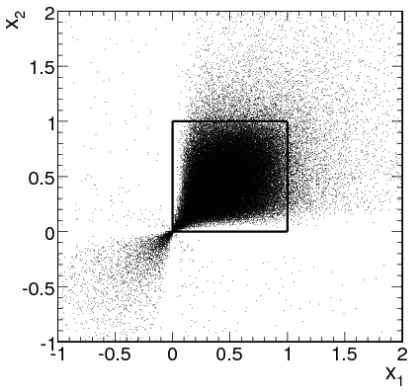

(a) The fractions x_i of the tau momentum carried away by the muon on generator level. All points outside the rectangle represent unphysical reconstructions and are dismissed.

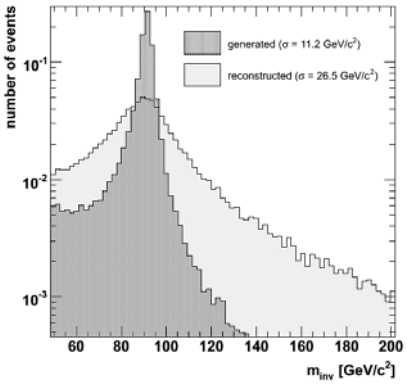

(b) Comparison of the mass distribution of the generated γ^*/Z resonances and the reconstructed mass distribution after applying the collinear approximation.

Figure B.2.: Spectra of the reconstruction of $\gamma^*/Z \to \mu\mu$ events using the generated particle momenta [139].

B.3. Additional Plots

$\tau\tau \to \mu + \tau-$jet Candidates in 2010 Data

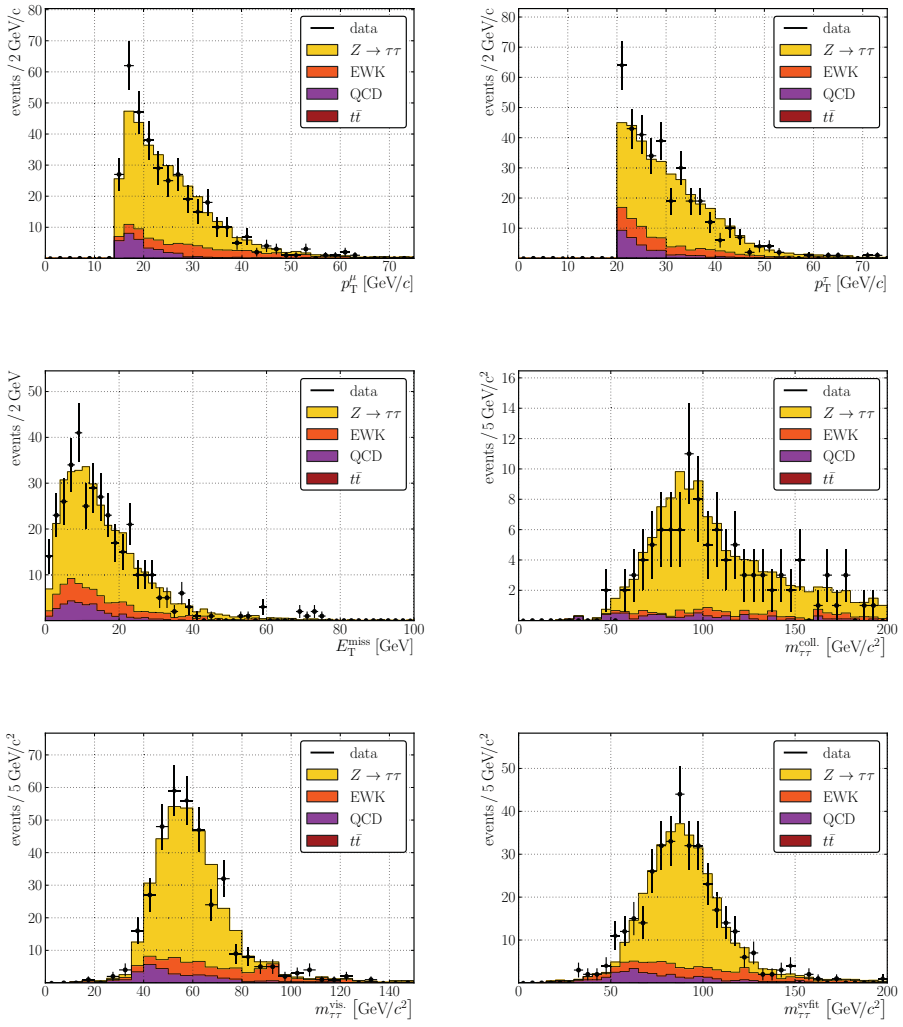

Figure B.3.: Comparison of reconstructed $\tau\tau \to \mu + \tau-$jet candidates in the data sample and in simulated event samples. The latter is scaled according to the production cross section and the intergrated luminosity. A correction for the imperfect description of the trigger algorithms in the simulation is applied.

Reconstructed Embedded $\tau\tau \to \mu + \tau-$jet Candidates

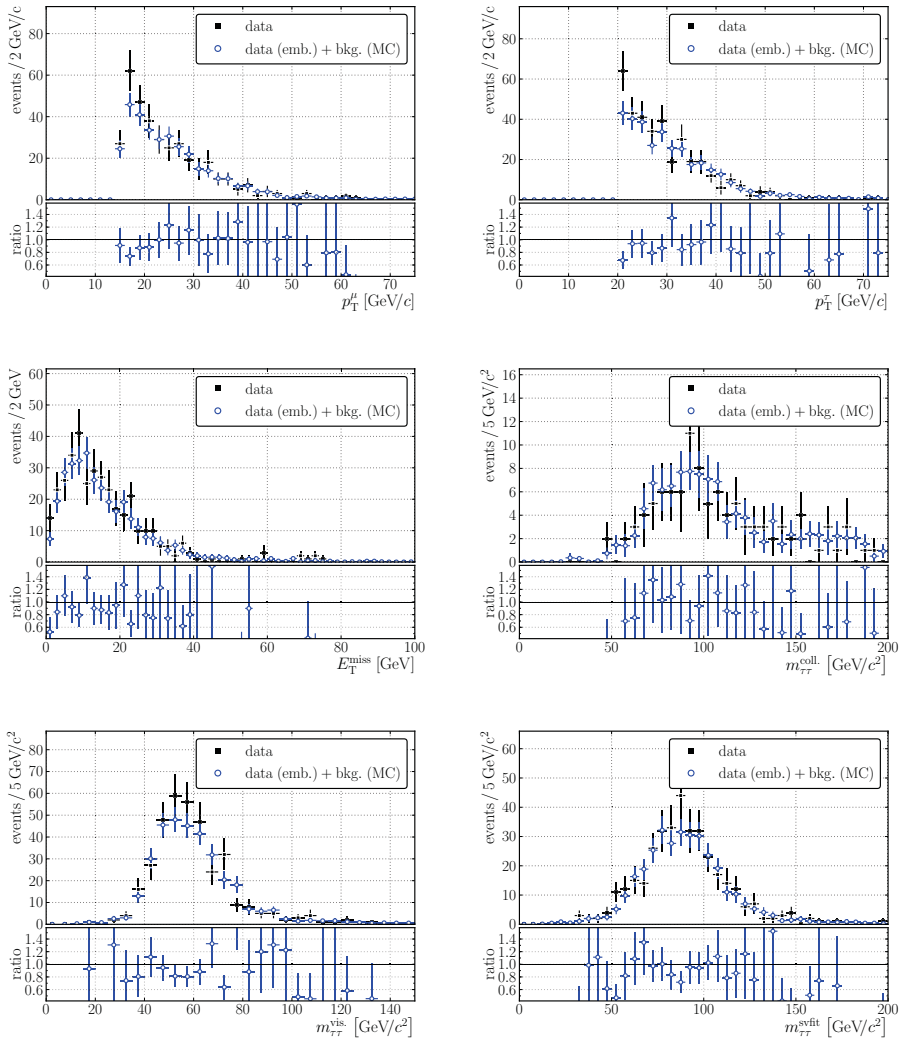

Figure B.4.: Comparison of different distributions of reconstructed $\tau\tau \to \mu + \tau-$jet candidates in a sample of embedded events and reconstructed $\tau\tau \to \mu + \tau-$jet candidates in the 2010 data sample. As the embedded sample covers only $Z \to \tau^+\tau^-$ events, it is necessary to add background contributions as well. They are scaled according to their individual production cross sections and the integrated luminosity.

List of Figures

List of Tables

Bibliography

[1] Rudolf Löbl. *Demokrits Atomphysik.* Erträge der Forschung ; 252. Wiss. Buchges., Darmstadt, 1987.

[2] Joseph John Thomson. On the structure of the atom: an investigation of the stability and periods of oscillation of a number of corpuscles arranged at equal intervals around the circumference of a circle; with application of the results to the theory of atomic structure. *Philosophical Magazine*, 7(39):237–265, 1904.

[3] Ernest Rutherford. The Scattering of the Alpha and Beta Rays and the Structure of the Atom. *Proceedings of the Manchester Literary and Philosophical Society IV*, pages 18–20, 1911.

[4] W. M. Yao et al. Review of particle physics. *J. Phys.*, G33:1–1232, 2006.

[5] Nicola Cabibbo. Unitary Symmetry and Leptonic Decays. *Physical Review Letters*, 10:531, 1963.

[6] Gustavo Branco, Luis Lavoura, and Joao Silva. *CP violation.* International series of monographs on physics ; 103. Clarendon Press, Oxford, 1999.

[7] Michael E. Peskin and Dan V. Schroeder. *An Introduction To Quantum Field Theory (Frontiers in Physics).* Westview Press, 1995.

[8] Bogdan Povh, editor. *Teilchen und Kerne : eine Einführung in die physikalischen Konzepte.* Springer-Lehrbuch. Springer, Berlin, 8. aufl. edition, 2009.

[9] F. Englert and R. Brout. Broken symmetry and the mass of gauge vector mesons. *Phys. Rev. Lett.*, 13(9):321–323, Aug 1964.

[10] G. S. Guralnik, C. R. Hagen, and T. W. B. Kibble. Global conservation laws and massless particles. *Phys. Rev. Lett.*, 13(20):585–587, Nov 1964.

[11] Peter W. Higgs. Broken symmetries and the masses of gauge bosons. *Phys. Rev. Lett.*, 13(16):508–509, Oct 1964.

[12] Abdelhak Djouadi. The Anatomy of electro-weak symmetry breaking. I: The Higgs boson in the standard model. *Phys. Rept.*, 457:1–216, 2008. hep-ph/0503172.

[13] Jeffrey Goldstone, Abdus Salam, and Steven Weinberg. Broken symmetries. *Phys. Rev.*, 127(3):965–970, Aug 1962.

[14] Martin-Stirling-Thorne-Watt Parton Distribution Functions, `http://projects.hepforge.org/mstwpdf/`.

[15] A. D. Martin, W. J. Stirling, R. S. Thorne, and G. Watt. Parton distributions for the LHC. *Eur. Phys. J.*, C63:189–285, 2009. arXiv:0901.0002.

[16] Online parton distribution calculator with graphical display, `http://durpdg.dur.ac.uk/hepdata/pdf3.html`.

[17] G. Arnison et al. Experimental observation of lepton pairs of invariant mass around $95\,\mathrm{GeV}/c^2$ at the CERN SPS collider. *Phys. Lett.*, B126:398–410, 1983.

[18] The ALEPH, DELPHI, L3, OPAL, SLD Collaborations, the LEP Electroweak Working Group, the SLD Electroweak and Heavy Flavour Groups. Precision Electroweak Measurements on the Z Resonance. *Phys. Rept.*, 427:257, 2006. hep-ex/0509008.

[19] Various Collaborations. Precision Electroweak Measurements and Constraints on the Standard Model. 2010. arXiv:1012.2367.

[20] LEP Electro-Weak Working Group, `http://lepewwg.web.cern.ch/LEPEWWG/`.

[21] Volker Büge. Virtualisation of Grid Resources and Prospects of the Measurement of Z Boson Production in Association with Jets at the LHC. urn:nbn:de:swb:90-90839.

[22] Danilo Piparo. Statistical Combination of Higgs Decay Channels and Determination of the Jet-Energy Scale of the CMS Experiment at the LHC. urn:nbn:de:swb:90-211175.

[23] Austin Ball, Michel Della Negra, L Foà, and Achille Petrilli. CMS technical design report, volume II: Physics performance. *J. Phys.*, G34:995–1579, 2007.

[24] Christoph Hackstein. Searches for the Higgs Boson at the LHC Based on its Couplings to Vector Bosons.

[25] LHC Higgs Cross Section Working Group, S. Dittmaier, C. Mariotti, G. Passarino, and R. Tanaka (Eds.). Handbook of LHC Higgs Cross Sections: 1. Inclusive Observables. *CERN-2011-002*, CERN, Geneva, 2011. arXiv:1101.0593.

[26] David Pegna, James Olsen, and Philipp Schieferdecker. Search for the Standard Model Higgs Boson Produced in Association with a W or Z Boson in pp Collisions at $\sqrt{s} = 7\,\mathrm{TeV}$. 2010. CERN-CMS-AN-2010-265.

[27] Stephanie Baffioni, Claude Charlot, Federico Ferri, Nikola Godinovic, P. Meridiani, Ivica Puljak, Roberto Salerno, and Y. Sirois. Discovery Potential for the SM Higgs Boson in the H $\to$ ZZ$^{(*)}$ $\to e^+e^-e^+e^-$ Decay Channel. CERN-NOTE-2006-115.

[28] Ulrich Felzmann, Günter Quast, and Christian Weiser. Observability of a Heavy Higgs Boson in the Channel qqH and H $\to$ ZZ $\to llq\bar{q}$. CERN-CMS-AN-2007-020.

[29] Haifeng Pi, Paul Avery, James Rohlf, Christopher Tully, and Shuichi Kunori. Search for Standard Model Higgs Boson via Vector Boson Fusion in the H $\to$ W$^+$W$^-$ to $l^{\pm}\nu jj$ Channel with $120 < m_{\mathrm{H}} < 250\mathrm{GeV}/c^2$. CERN-CMS-NOTE-2006-092.

[30] G Davatz, M Dittmar, and A Giolo-Nicollerat. Standard Model Higgs Discovery Potential of CMS in H $\to$ WW $\to l\nu l\nu$ Channel. CERN-CMS-NOTE-2006-047.

[31] Tevatron, `http://www-bdnew.fnal.gov/tevatron/`.

[32] SLAC National Accelerator Laboratory, `http://www.slac.stanford.edu/`.

[33] Martin Goebel and for the Gfitter Group. Status of the global fit to electroweak precisions data. *PoS*, ICHEP2010:570, 2010. arXiv:1012.1331.

[34] T. Aaltonen et al. Combined CDF and D0 Upper Limits on Standard Model Higgs Boson Production with up to 8.2 fb-1 of Data. 2011. arXiv:1103.3233.

[35] Lyndon Evans et al. LHC Machine. *JINST*, 3:S08001, 2008.

[36] The LHC Study Group. Large hadron collider accelerator project. CERN-AC-93-03 (LHC).

[37] G. Aad et al. The ATLAS Experiment at the CERN Large Hadron Collider. *JINST*, 3:S08003, 2008.

[38] G. Aad et al. Expected Performance of the ATLAS Experiment - Detector, Trigger and Physics. 2009. arXiv:0901.0512.

[39] A. Augusto Alves et al. The LHCb Detector at the LHC. *JINST*, 3:S08005, 2008.

[40] The TOTEM Collaboration. The totem experiment at the cern large hadron collider. *Journal of Instrumentation*, 3(08):S08007, 2008.

[41] K. Aamodt et al. The ALICE experiment at the CERN LHC. *JINST*, 3:S08002, 2008.

[42] R. Barate et al. Search for the standard model Higgs boson at LEP. *Phys. Lett.*, B565:61–75, 2003. hep-ex/0306033.

[43] LHC Programme Coordination, `http://lpc.web.cern.ch/lpc/`.

[44] LHC OP Vistars, `http://op-webtools.web.cern.ch/op-webtools/Vistar/`.

[45] CMS Collaboration. Measurement of CMS Luminosity. 2010. CMS PAS EWK-10-004.

[46] CMS Collaboration. Performance of the CMS Level-1 trigger during commissioning with cosmic ray muons and LHC beams. *Journal of Instrumentation*, 5(03):T03002, 2010.

[47] LHC Beam Commissioning Working Group: Werner Herr, Beam-Beam Observations, `https://lhc-commissioning.web.cern.ch/lhc-commissioning/meetings/20101026/WHerr.pdf`.

[48] LHC machine commissioning and the near future, `http://lhc-commissioning.web.cern.ch/lhc-commissioning/presentations/2010/lhc-status-split-oct10.pdf`.

[49] LHC operation wiki, `http://op-webtools.web.cern.ch/op-webtools/dokuwiki/doku.php`.

[50] CERN. *oai:cds.cern.ch:1347440. LHC Lumi Days: LHC Workshop on LHC Luminosity Calibration*, Geneva, 2011. CERN. Organisers: Burkhardt, Helmut; Ferro-Luzzi, Massimiliano; Mangano, Michelangelo.

[51] Simon van der Meer. Calibration of the effective beam height in the ISR. Technical Report CERN-ISR-PO-68-31. ISR-PO-68-31, CERN, Geneva, 1968.

[52] CMS Collaboration. Absolute Luminosity Normalization. Mar 2011. CMS DP 2011-002.

[53] Michel Della Negra, L Foà, A Hervé, and Achille Petrilli. *CMS physics: Technical Design Report*. CERN, Geneva, 2006.

[54] The CMS Collaboration. The CMS experiment at the CERN LHC. *JINST*, 3 S08004:361, 2008.

[55] CMS outreach, `http://cmsinfo.cern.ch/outreach/`.

[56] CMS Collaboration. *The TriDAS Project Technical Design Report, Volume 2: Data Aquisition and High-Level Trigger*. CERN, Geneva, 2002.

[57] CMS Collaboration. Jet Energy Calibration and Transverse Momentum Resolution in CMS. 2011. CMS-PAS-JME-10-011.

[58] CMS Collaboration. Jet Energy Resolution in CMS at $\sqrt{s} = 7\,\text{TeV}$. 2011. CMS-PAS-JME-10-014.

[59] CMS Collaboration. Particle-Flow Event Reconstruction in CMS and Performance for Jets, Taus, and MET. Apr 2009. CMS PAS PFT-09-001.

[60] The CMS Collaboration. Commissioning of the Particle-flow Event Reconstruction with the first LHC collisions recorded in the CMS detector. 2010. CMS PAS PFT-10-001.

[61] R. Fruhwirth. Application of Kalman filtering to track and vertex fitting. *Nucl. Instrum. Meth.*, A262:444–450, 1987.

[62] T Speer, W Adam, R Frühwirth, A Strandlie, T Todorov, and M Winkler. Track Reconstruction in the CMS Tracker. Technical Report CERN-CMS-CR-2005-014, CERN, Geneva, Jul 2005.

[63] CMS Collaboration. Performance of cms muon reconstruction in cosmic-ray events. *Journal of Instrumentation*, 5(03):T03022, 2010.

[64] CMS Collaboration. Performance of muon identification in 2010 data. 2011. CMS PAS MUO-10-004.

[65] Dimuon composition in atlas at 7 tev. Technical Report ATLAS-CONF-2011-003, CERN, Geneva, Feb 2011.

[66] John Conway, Evan Friis, M Squires, and Christian Veelken. The Tau Neural Classifier algorithm: tau identification and decay mode reconstruction using neural networks. 2010. CERN-CMS-AN-2010-099.

[67] CMS Collaboration. Tau Identification in CMS. 2011. CMS-PAS-TAU-11-001.

[68] Michael Heinrich. A Jet Based Approach to Measuring Soft Contributions to Proton-Proton Collisions with the CMS Experiment. urn:nbn:de:swb:90-218398.

[69] Andreas Oehler. Strategy for an Initial Measurement of the Inclusive Jet Cross Section with the CMS Detector . urn:nbn:de:swb:90-149218.

[70] Gerald C. Blazey et al. Run II jet physics. 2000. hep-ex/0005012.

[71] G. Salam and G. Soyez. A practical seedless infrared-safe cone jet algorithm. 2007. JHEP05 (2007) 086.

[72] Matteo Cacciari. FastJet: A Code for fast k(t) clustering, and more. 2006. hep-ph/0607071.

[73] J. M. Butterworth, J. P. Couchman, B. E. Cox, and B. M. Waugh. Kt-Jet: A C++ implementation of the k_{T} clustering algorithm. *Comput. Phys. Commun.*, 153:85–96, 2003. hep-ph/0210022.

[74] Gregory Soyez. The SISCone and anti-kt jet algorithms. 2008. arXiv:0807.0021.

[75] Torbjörn Sjöstrand. *Pythia 6.4 Physics and Manual*. hep-ph/0603175, 2006.

[76] G. Corcella et al. HERWIG 6.5: an event generator for Hadron Emission Reactions With Interfering Gluons (including supersymmetric processes). *JHEP*, 01:010, 2001. hep-ph/0011363.

[77] Rikkert Frederix. Recent developments in madgraph/madevent v4. *Nuclear Physics B - Proceedings Supplements*, 183:285 – 289, 2008. Proceedings of the 9th DESY Workshop on Elementary Particle Theory.

[78] K. Arnold et al. VBFNLO: A parton level Monte Carlo for processes with electroweak bosons. *Comput. Phys. Commun.*, 180:1661–1670, 2009. arXiv:0811.4559.

[79] Simone Alioli, Paolo Nason, Carlo Oleari, and Emanuele Re. A general framework for implementing NLO calculations in shower Monte Carlo programs: the POWHEG BOX. *JHEP*, 06:043, 2010. arXiv:1002.2581.

[80] Richard Corke and Torbjorn Sjostrand. Improved Parton Showers at Large Transverse Momenta. *Eur. Phys. J.*, C69:1–18, 2010. arXiv:1003.2384.

[81] Torbjorn Sjostrand et al. High-energy physics event generation with PYTHIA 6.1. *Comput. Phys. Commun.*, 135:238–259, 2001. hep-ph/0010017.

[82] Rick Field. Physics at the Tevatron. *Acta Phys. Polon.*, B39:2611–2672, 2008.

[83] J. Pumplin et al. New generation of parton distributions with uncertainties from global QCD analysis. *JHEP*, 07:012, 2002. hep-ph/0201195.

[84] Boost 2011 (May 23, 2011): Rick Field, Underlying Event and Fragmentation Models Tuning, `https://indico.cern.ch/getFile.py/access?contribId=14&resId=0&materialId=slides&confId=138809`.

[85] Stanislaw Jadach, Zbigniew Was, Roger Decker, and Johann Kuehn. The tau decay library TAUOLA: Version 2.4. *Comput. Phys. Commun.*, 76:361–380, 1993.

[86] Zbigniew Was. TAUOLA the library for tau lepton decay, and KKMC/KORALB/KORALZ/... status report. *Nucl. Phys. B, Proc. Suppl.*, 98(hep-ph/0011305):96–102, 2000.

[87] TAUOLA and PHOTOS, `http://wasm.home.cern.ch/wasm/goodies.html`.

[88] Stefano Frixione and Bryan R. Webber. Matching NLO QCD computations and parton shower simulations. *JHEP*, 06:029, 2002. hep-ph/0204244.

[89] Simone Alioli, Paolo Nason, Carlo Oleari, and Emanuele Re. NLO vector-boson production matched with shower in POWHEG. *JHEP*, 07:060, 2008. arXiv:0805.4802.

[90] Simone Alioli, Paolo Nason, Carlo Oleari, and Emanuele Re. Vector boson plus one jet production in POWHEG. *JHEP*, 01:095, 2011. arXiv:1009.5594.

[91] Simone Alioli, Paolo Nason, Carlo Oleari, and Emanuele Re. NLO Higgs boson production via gluon fusion matched with shower in POWHEG. *JHEP*, 04:002, 2009. arXiv:0812.0578.

[92] Paolo Nason and Carlo Oleari. NLO Higgs boson production via vector-boson fusion matched with shower in POWHEG. *JHEP*, 02:037, 2010. arXiv:0911.5299.

[93] ROOT, `http://root.cern.ch/`.

[94] PROOF, `http://root.cern.ch/twiki/bin/view/ROOT/PROOF`.

[95] S. Agostinelli et al. G4–a simulation toolkit. *Nuclear Instruments and Methods in Physics Research Section A: Accelerators, Spectrometers, Detectors and Associated Equipment*, 506(3):250 – 303, 2003.

[96] J. Allison et al. Geant4 developments and applications. *Nuclear Science, IEEE Transactions on*, 53(1):270 –278, Feb. 2006.

[97] B Blumenfeld, D Dykstra, L Lueking, and E Wicklund. Cms conditions data access using frontier. *Journal of Physics: Conference Series*, 119(7):072007, 2008.

[98] Armin Scheurer et al. German contributions to the cms computing infrastructure. *Journal of Physics: Conference Series*, 219(6):062064, 2010. ID:CHEP299.

[99] D. Cooper, S. Santesson, S. Farrell, S. Boeyen, R. Housley, and W. Polk. RFC 5280 - Internet X.509 Public Key Infrastructure Certificate and Certificate Revocation List (CRL) Profile. Technical report, May 2008.

[100] CRAB, `https://twiki.cern.ch/twiki/bin/view/CMS/CRAB`.

[101] Grid-Control, `https://ekptrac.physik.uni-karlsruhe.de/trac/grid-control/`.

[102] Grid Control - An Alternative Grid Job Submission Tool, `http://indico.desy.de/contributionDisplay.py?contribId=5&confId=2295`.

[103] A. Abulencia et al. Measurements of Inclusive W and Z Cross Sections in p-pbar Collisions at $\sqrt{s} = 1.96\,\text{TeV}$. *J. Phys.*, G34:2457–2544, 2007. hep-ex/0508029.

[104] S. Abachi et al. W and Z boson production in p anti-p collisions at $\sqrt{s} = 1.8\,\text{TeV}$. *Phys. Rev. Lett.*, 75:1456–1461, 1995. hep-ex/9505013.

[105] Hung-Liang Lai et al. New parton distributions for collider physics. *Phys. Rev.*, D82:074024, 2010. arXiv:1007.2241.

[106] Rick Field. Early LHC Underlying Event Data - Findings and Surprises. 2010. arXiv:1010.3558.

[107] J. Pumplin et al. New generation of parton distributions with uncertainties from global QCD analysis. *JHEP*, 07:012, 2002. hep-ph/0201195.

[108] CMS Collaboration. Measurement of the W and Z inclusive production cross sections at $\sqrt{s} = 7\,\text{TeV}$ with the CMS experiment at the LHC. 2010. CMS PAS EWK-10-002.

[109] CMS Collaboration. Performance of muon identification in pp collisions at $\sqrt{s} = 7\,\text{TeV}$. 2010. CMS PAS MUO-10-002.

[110] CMS Collaboration. Commissioning of the cms experiment and the cosmic run at four tesla. *Journal of Instrumentation*, 5(03):T03001, 2010.

[111] J. Alcaraz and other. Measurement of the Inclusive W and Z Cross Section in pp Collisions at $\sqrt{s} = 7\,\text{TeV}$: Update with full 2010 statistics. 2011. CERN-CMS-AN-2010-395.

[112] CMS Collaboration. Measurement of Inclusive W and Z Cross Sections in pp Collisions at $\sqrt{s} = 7\,\text{TeV}$. 2011. CMS PAS EWK-10-005.

[113] CMS Collaboration. Measurement of Tracking Efficiency. 2010. CMS PAS TRK-10-002.

[114] N. Adam, J. Berryhill, V. Halyo, A. Hunt, and K. Mishra. Generic Tag and Probe Tool for Measuring Efficiency at CMS with Early Data. CMS AN-2009/111.

[115] Ryan Gavin, Ye Li, Frank Petriello, and Seth Quackenbush. FEWZ 2.0: A code for hadronic Z production at next-to- next-to-leading order. 2010. arXiv:1011.3540.

[116] Kirill Melnikov and Frank Petriello. Electroweak gauge boson production at hadron colliders through $O(\alpha_s^2)$. *Phys. Rev. D*, 74(11):114017, Dec 2006.

[117] Stefano Catani and Massimiliano Grazzini. An NNLO subtraction formalism in hadron collisions and its application to Higgs boson production at the LHC. *Phys. Rev. Lett.*, 98:222002, 2007. hep-ph/0703012.

[118] Stefano Catani, Leandro Cieri, Giancarlo Ferrera, Daniel de Florian, and Massimiliano Grazzini. Vector boson production at hadron colliders: a fully exclusive QCD calculation at NNLO. *Phys. Rev. Lett.*, 103:082001, 2009. arXiv:0903.2120.

[119] A. D. Martin, W. J. Stirling, R. S. Thorne, and G. Watt. Uncertainties on $alpha_s$ in global PDF analyses and implications for predicted hadronic cross sections. *Eur. Phys. J.*, C64:653–680, 2009. arXiv:0905.3531.

[120] C. Albajar et al. Studies of intermediate vector boson production and decay in ua1 at the cern proton-antiproton collider. *Zeitschrift für Physik C Particles and Fields*, 44:15–61, 1989. 10.1007/BF01548582.

[121] J. Alitti and others. Measurement of w and z production cross sections at the cern proton-antiproton collider. *Zeitschrift für Physik C Particles and Fields*, 47:11–22, 1990. 10.1007/BF01551906.

[122] B. Abbott et al. Extraction of the width of the W boson from measurements of $\sigma(p\bar{p} \to W + X) \times \mathrm{B}(W \to \nu)$ and $\sigma(p\bar{p} \to Z + X) \times \mathrm{B}(Z \to ee)$ and their ratio. *Phys. Rev.*, D61:072001, 2000.

[123] A measurement of the total $\mathrm{W}^{\pm}$ and Z/γ^* cross sections in the e and μ decay channels and of their ratios in pp collisions at $\sqrt{s} = 7\,\mathrm{TeV}$ with the atlas detector. Technical Report ATLAS-CONF-2011-041, CERN, Geneva, Mar 2011.

[124] Jr. Massey, Frank J. The kolmogorov-smirnov test for goodness of fit. *Journal of the American Statistical Association*, 46(253):pp. 68–78, 1951.

[125] Tejinder Virdee, Achille Petrilli, and Austin Ball. CMS High Level Trigger. Technical Report LHCC-G-134. CERN-LHCC-2007-021, CERN, Geneva, Jun 2007. revised version submitted on 2007-10-19 16:57:09.

[126] Rudolph Emil Kalman. A new approach to linear filtering and prediction problems. *Transactions of the ASME–Journal of Basic Engineering*, 82(Series D):35–45, 1960.

[127] Hwidong Yoo, Adam Everett, Chang Liu, and Norbert Neumeister. Level-3 Muon Trigger Performance on CRAFT data. 2009. CERN-CMS-AN-2009-127.

[128] private discussion with Ingo Bloch.

[129] Juan Alcaraz et al. Measurement of the inclusive $W \to \mu\nu$ cross section in pp collisions at $\sqrt{s} = 7\,\mathrm{TeV}$ with fixed shape templates. CERN-CMS-AN-2011-053.

[130] C. J. Clopper and E. S. Pearson. The Use of Confidence or Fiducial Limits Illustrated in the Case of the Binomial. *Biometrika*, 26(4):404–413, 1934.

[131] Giovanni Petrucciani. Measurement of the tracking efficiency for muons using the tag and probe method. CMS AN-2010/149.

[132] Matteo Sani. Electron Efficiency Measurements using Tag and Probe. CMS AN-2010/291.

[133] Hongwan Liu, Frey Blekman, and Julia Thom. $t\bar{t}$ Electron Trigger Efficiency Measurement using Tag and Probe in Early Data. CMS AN-2010/293.

[134] Agni Bethani, Armin Burgmeier, Guenter Quast, Gregory Schott, Manuel Zeise, et al. Measurement of $\sigma(\mathrm{pp} \to Z) \cdot \mathrm{BR}(Z \to \tau\tau)$ in the dimuon channel with CMS in pp collisions at 7 TeV. CMS-AN-2010-446.

[135] Serguei Chatrchyan et al. Measurement of the Inclusive Z Cross Section via Decays to Tau Pairs in pp Collisions at $\sqrt{s} = 7\,\mathrm{TeV}$. 2011. arXiv:1104.1617.

[136] J. Antonelli et al. Measurement of the Inclusive $Z \to \tau\tau$ Cross Section in pp Collisions at $\sqrt{s} = 7\,\mathrm{TeV}$. CERN-CMS-AN-2010-431.

[137] M. Bachtis, J. Swanson, A. Savin, S. Dasu, and W. Smith. Study of the di-tau spectrum using muon-tau and electron-tau final states with CMS detector at $\sqrt{s} = 7\,\mathrm{TeV}$. 2010. CERN-CMS-AN-2010-387.

[138] John Conway, Evan Friis, M Squires, Christian Veelken, Guiseppe Cerati, S Malvezzi, R Manzoni, E. Re, and Jeff Kolb. Search for MSSM neutral Higgs $\to \tau^+\tau^-$ Production using the TaNC Tau id. algorithm. CERN-CMS-AN-2010-460.

[139] Manuel Zeise. Modelling of Background from Z Boson Decays for the Higgs Boson Search at the LHC in the Channel $H \to \tau\tau$. 2008. IEKP-KA/2008-10.

[140] CMS Collaboration. Studies of tracker material. CMS PAS TRK-10-003.

[141] Weekly Tracker DPG Meetings (September 30, 2010): Ernesto Migliore, Tracker Alignment Status Report, `https://indico.cern.ch/materialDisplay.py?contribId=3&sessionId=5&materialId=slides&confId=82593`.

[142] CMS Tracker Alignment Workshop (May 31, 2011): Marco Musich, The CMS Tracker Alignment Primary Vertex Validation, `https://indico.cern.ch/getFile.py/access?contribId=29&sessionId=6&resId=0&materialId=slides&confId=137973`.

[143] S. Slabospitsky. *TopReX 4.23 short manual*, 2006. `http://lpsc.in2p3.fr/d0/generateurs/txman_423.ps`.

[144] Matteo Cacciari, Gavin P. Salam, and Gregory Soyez. The Catchment Area of Jets. *JHEP*, 04:005, 2008. arXiv:0802.1188.

[145] DYNNLO homepage, `http://theory.fi.infn.it/grazzini/dy.html`.

[146] FEWZ homepage, `http://gate.hep.anl.gov/fpetriello/FEWZ.html`.

[147] Christopher Jung. *Grid Computing for LHC and Methods for W Boson Mass Measurement at CMS*. PhD thesis, University of Karlsruhe, 2007. IEKP-KA/2008-5.

[148] Source code of the Replacer module. `http://cmssw.cvs.cern.ch/cgi-bin/cmssw.cgi/CMSSW/TauAnalysis/MCEmbeddingTools/src/ParticleReplacerClass.cc`.

Danksagung

Mein besonderer Dank gilt Prof. Günter Quast für die hervorragende Betreuung während meiner gesamten Zeit am EKP. Er ließ mir immer viel Raum eigene Ideen und Ansätze zu verfolgen und hatte dennoch stets Zeit, um über offene Fragen und Probleme zu diskutieren. Sein Engagement für die Arbeitsgruppe und seine Begeisterung für die Physik sind beispiellos und sehr motivierend.

Für die Übernahme des Korreferats danke ich Prof. Dr. Wim de Boer.

Armin Burgmeier gilt mein Dank für die hervorragende Zusammenarbeit, die vielfältigen Diskussionen und die vielen hilfreichen Kommentare.

Mein Dank gilt darüber hinaus meinen Kollegen Joram Berger, Christoph Hackstein, Thomas Hauth, Michael Heinrich, Hauke Held, Oliver Oberst, Andreas Oehler, Armin Scheurer und Fred Stober für das Korrekturlesen meiner Arbeit, für die vielen Diskussionen und natürlich für die sehr angenehme Atmosphäre in der Arbeitsgruppe. Christoph danke ich darüber hinaus besonders für sein Geduld, mir Sachverhalte der theoretischen Physik näher zu bringen.

Ein besonderer Dank gebürt Klaus Rabbertz, Hauke Held, Philipp Schieferdecker und Fred Stober für die unzähligen Diskussionen über Physik und andere Dinge, welche die Zeit am CERN nicht nur lehrreich sondern auch sehr angenehm gemacht haben.

Benjamin Klein und Sinéad Walsh danke ich für die sehr gute Zusammenarbeit am CERN und die Bereitschaft Teile meiner Arbeit Korrektur zu lesen.

Meinen früheren Kollegen Volker Büge, Ulrich Felzmann, Danilo Piparo und Christophe Saout danke ich für Ihre Unterstützung und ihre Ratschläge weit über ihre Zeit am Institut hinaus.

Meinen Eltern danke ich für ihre Unterstützung und ihr großes Vertrauen. Martin Engel und meinen Freunden danke ich für die moralische Unterstützung.

Hiermit versichere ich, die vorliegende Arbeit selbstständig verfasst und nur die angegebenen Hilfsmittel verwendet zu haben.

Manuel Zeise

Karlsruhe, den 28. Juni 2011